DEEP NEURAL NETWORKS FOR IMPROVED TERMINAL VOLTAGE AND STATE-OF-CHARGE ESTIMATION OF LITHIUM-ION BATTERIES FOR TRACTION APPLICATIONS

Carlos J. G. Vidal

McMaster University, vidalc2@mcmaster.ca

DEEP NEURAL NETWORKS FOR IMPROVED TERMINAL VOLTAGE AND STATE-OF-CHARGE ESTIMATION OF LITHIUM-ION BATTERIES FOR TRACTION APPLICATIONS

BY

CARLOS J. G. VIDAL, M.SC., MBA.

A THESIS

SUBMITTED TO THE DEPARTMENT OF MECHANICAL ENGINEERING

AND THE SCHOOL OF GRADUATE STUDIES OF MCMASTER

UNIVERSITY IN PARTIAL FULFILMENT OF THE REQUIREMENTS

FOR THE DEGREE OF DOCTOR OF PHILOSOPHY

i

Doctor of Philosophy (2020) McMaster University
(Mechanical Engineering) Hamilton, Ontario, Canada

TITLE: Deep neural networks for improved terminal voltage and State-of-Charge estimation of lithium-ion batteries for traction applications

AUTHOR: Carlos Jose Goncalves Vidal, M.Sc., MBA

SUPERVISOR: Dr. Ali Emadi

NUMBER OF PAGES: xix, 227

This work is dedicated to my parents, wife, and sons.

Abstract

The growing interest in more electrified vehicles has been pushing the industry and academia to pursue new and more accurate ways to estimate the xEV batteries State-of-Charge (SOC). The battery system still represents one of the many technical barriers that need to be eliminated or reduced to enable the proliferation of more xEV in the market, which in turn can help reduce CO_2 emissions. Battery modelling and SOC estimation of Lithium-ion batteries (Li-ion) at a wide temperature range, including negative temperatures, has been a challenge for many engineers.

For SOC estimation, several models configurations and approaches were developed and tested as results of this work, including different non-recurrent neural networks, such as Feedforward deep neural networks (FNN) and recurrent neural networks based on long short-term memory recurrent neural networks (LSTM-RNN). The approaches have considerably improved the accuracy presented in the previous state-of-the-art, and have expanded the application throughout five different Li-ion at a wide temperature range, achieving error as low as 0.66% Root Mean Square Error at -10ºC using an FNN approach and 0.90% using LSTM-RNN. Therefore, the use of deep neural networks developed in this work can increase the potential for xEV application, especially where accuracy at negative temperatures is essential.

For Li-ion modelling, a cell model using LSTM-RNN (LSTM-VM) was developed for the first time to estimate the battery cell terminal voltage and is

compared against a gated recurrent unit (GRU-VM) approach and a Third-order Equivalent Circuit Model based on Thevenin theorem (ECM). The models were extensively compared for different Li-ion at a wide range of temperature conditions. The LSTM-VM has shown to be more accurate than the two other benchmarks, where could achieve 43 (mV) Root Mean Square Error at -20⁰C, a third when compared to the same situation using ECM. Although the difference between LSTM-VM and GRU-VM is not that steep.

Finally, throughout the work, several methods to improve robustness, accuracy and training time have been introduced, including Transfer Learning applied to the development of SOC estimation models, showing great potential to reduce the amount of data necessary to train LSTM-RNN as well as improve its accuracy.

Acknowledgement

I would like to express my most profound admiration and gratitude to my academic supervisor Dr. Ali Emadi, for his inspiring kindness and leadership that kept us together and confident through terrible times. A significant deal of growth beyond technical and professional areas have been learned over the years through his example.

I would also like to extend my most profound appreciation to Dr. Pawel Malysz for his guidance and support throughout all the steps that lead to the compilation of this thesis. Equally, I also would like to thank Dr. Phil Kollmeyer for his friendship and support throughout all the years. So many times, he changed my mind when I thought something could not be improved; his help was crucial for this work. I also would like to thank Dr. Ephrem Chemali for the support of anything related to artificial intelligence. His doctorate work has greatly influenced my research. To Dr. Ryan Ahmed, I would like to express my gratitude for his support and honest interest in sharing his knowledge.

I would like to recognize the great support of two of my best friends, Dan Manolescu and Daniel Goretti. Their bright minds and friendship have been indispensable. I would also like to thank my colleagues and friends Jeremy Lempert, Mike Haussmann, Lucas Bruck, Dr. Brock Howey, Dr. Alan Callegaro,

Silvio Rotilli, and Chris Mak for their support inside and outside the lab. I would like to thank my friends from the Wastrels cycling club for their support in many situations, especially going up Wilson Street at 6:15 am above 30km/h. The early morning rides and the coffee afterwards helped me to maintain my physical and mental health throughout the last years.

Nomenclature

AI	Artificial Intelligence
BMS	Battery Management System
CC/CV	Constant-Current Constant Voltage profile
ECM	Equivalent Circuit Model
EIS	Electrochemical Impedance Spectroscopy
ESS	Energy Storage System
FNN	Feedforward Neural Networks
HPPC	Hybrid Pulse Power Characterization
HW	Highway Fuel Economy Cycle
KF	Kalman Filter
LA92	Unified Cycle Driving Schedule
LFP	Lithium Iron Phosphate (cathode: LiFePO4; anode: C)
LSTM	Long Short-Term Memory
LTO	Lithium Titanate anode (cathode: Not Informed; anode: Li4Ti5O12)
MAE	Mean Absolute Error
MLP	Multi-Layer Perceptron
MSE	Mean Squared Error
NCA	Lithium Nickel Cobalt Aluminum Oxide (cathode: LiNiCoAlO2; anode: C)
NMC	Lithium Nickel Cobalt Manganese Oxide (cathode: LiNiCoMnO2; anode: C)
OCV	Open-Circuit Model
RMSE	Root Mean Squared Error
RNN	Recurrent Neural Networks
RUL	Remaining Useful Life
SOHc	State-of-Health based on battery capacity loss
SOHr	State-of-Health based on the increase of battery resistance
SOP	State-of-Power
TF	Transfer Learning
UDDS	Urban Dynamometer Driving Schedule
US06	US06 Supplemental Federal Test Procedure
xEV	Electrified Vehicle

CONTENTS

List of Figures

xviii

1. INTRODUCTION

1.1. Problem statement

The transportation industry faces many challenges to improve efficiency, expand performance, advance connectivity, increase autonomy, and reduce emissions. Some of the biggest automotive markets, the USA and China, have established targets to reduce CO_2 emissions by 12% and 18% respectively from 2017 to 2020[1]. The electrified vehicle (xEV) market is estimated to reach 7.4% of the global car fleet. However, depending on the environmental policies applied by each country, this number can vary from 3.5% to 18.5% [2], [3]. Although due to the uncertainties generated by the COVID-19 pandemic, these predictions can be largely affected as the current low investment on the oil market can be shifted to green energy and electrified transportation sectors [4], which can increase the demand for better powertrain systems, including electric motors and energy storage systems (ESS).

The electrified powertrain is one of the most effective technologies to enable the improvement of vehicle efficiency, but finding the best trade-off between efficiency and costs remains a significant challenge[5]. As the Li-ion, which composes most of the xEV ESS, remains one of the most expensive parts of the xEV[6], [7], therefore significant research and development interests have been put upon the improvement of the battery pack and its components and sub-systems, e.g. Li-ion cell, thermal management system, battery management system.

The battery management system (BMS) is responsible for interfacing the communication between the vehicle energy management system (EMS) and the

battery pack [8]. The BMS contains all the algorithms and control policies necessary to guarantee the safety and performance of the battery pack, including the battery states, such as SOC, State-of-Health (SOH), and State-of-Power (SOP). The SOC estimation determines how much energy it is available in the vehicle battery pack and has a significant impact on the vehicle EMS, including range estimation, overall efficiency, and indirectly the vehicle cost due to overdesign [5], [6]. Therefore, estimate the battery SOC correctly it is crucial, although due to the non-linear nature of the batteries, especially at low temperature [9], it still a challenge that the automotive industry has to face [9], [10]. For example, when driving an xEV in countries like Canada, that traditionally have extremely cold winters, a perceptive reduction in the vehicle range capabilities will occur. According to the historical data from 1981 to 2010 collected in Toronto, an average of 100 days per year were below 0℃ and 130 days under 2℃ [11], [12]; some days it can reach temperatures as low as -41℃ [12] as showed on data collected from colder cities, such as Trois Rivieres in the province of Quebec in Canada.

One of the simplest methods used to estimate the battery SOC is based on Coulomb counting, which keeps track of the charges and discharges currents of the battery by summing the battery current over time, although it is a very unprecise method when used for xEV application as the error tends to accumulate. Another straightforward method is based on the battery open-circuit voltage (OCV), which can be correlated to the battery SOC in a lookup table (LUT). However, it is not a practical method for real-time estimation as it requires opening the battery terminals

and wait hours before the battery complete its final electrochemical reaction to provide an accurate OCV measurement [9], which turns to be impractical for xEV application. Hence, more sophisticated methods are necessary to deal with the dynamics and non-linearities of the xEV battery, which include model-based methods, adaptative filters, machine learning algorithms, non-linear observer, and the combination of two or more of the methods. For a comprehensive review of the different approaches to the estimation of SOC, SOH, SOP, and other battery states, readers are referred to [8], [13]–[15]

In 2019 the daily amount of data generated by each connected vehicle was four terabytes, but the total amount of data from all sources is expected to be 44 zettabytes in 2020[16], which in turn forecasts to generate 750 billion dollars by 2030 [17]. Although this is only a small fraction when compared to the 15 trillion dollars that artificial intelligence (AI) can add to the world economy by 2030[18]. Within this scenario, general-purpose technologies, machine learning (ML), and deep neural networks (NN) can be applied to solve many engineering problems. As battery technology grows and matures, a significant amount of data is being collected and analyzed in a partially or fully automated fashion [19] to improve battery design and usage. This plethora of data has made it possible to improve BMS performance [20] via big data, the internet of things (IoT), cloud computing, and the ML methods investigated [13]. In the case of SOC and SOH estimation based on ML methods, the main computational load demanded by these approaches happens during its off-line training phase [21], making it feasible for

implementation on typical BMS hardware. Machine learning data-driven approaches to battery SOC and SOH estimation have been providing recent advances in the field [7], [19], [22], [23].

The research gaps related to the thesis problem statement are listed below:

Research gaps summary

1. The interconnected effects of low temperature on Li-ion batteries applied to xEV application need to be further explored

2. Battery models and SOC estimation algorithms have considerably high errors at low temperatures. The lower the temperature, the harder it is to maintain good accuracy.

3. Despite the increase of the use o Machine learning algorithms applied to SOC and SOH estimation, a large part of the surveyed research has not used Li-ion datasets that contain a wide temperature range, including negative temperatures.

4. Battery datasets based on xEV applications are harder to obtain from public sources and even harder at a wide temperature range, which increases the difficulty of comparing modelling approach across multiple published pieces of research.

5. When comparing Machine Learning algorithms, most research has not considered the variability of results due to multiple local minima. Therefore many model comparison presented in prior research does not present conclusive answers

5

6. Long short-term memory recurrent neural networks approach has presented high accuracy on SOC estimation, based on a wide temperature range, but the prior art has not validated the approach on different Li-ion batteries, and the search for the right model size in terms of the number of parameters need to be further explored.

7. The prior art has shown considerable improvement in the use of a moving average filter to create an external memory feature to add to the feedforward neural network structure, although the accuracy provided still lower than the long short-term memory approach and the use of different filters need to be further explored.

8. Combining SOC and SOH estimation need to be explored, as the battery ages the SOC estimation model needs to maintain it is accuracy, although very few research papers have addressed this using Machine Learning approaches

9. Further work on SOC estimation at the battery pack level, considering the intrinsic manufacturing variation, and at a wide temperature range from each cell in the pack should be done using the Machine Learning approach and the data from the same type but from different battery cells are necessary.

1.2. Research Contributions and Novelty

The results of this research represent significant contributions to the area of battery modelling and state of charge estimation, as well as to the body of knowledge in

deep neural networks and battery management systems field. In order to provide a summary of research contributions, a list of original research goals presented in is thesis are listed below:

Research Contributions

10. A comprehensive and critical review focused on the low-temperature effect for xEV application

11. A survey of battery SOC and SOH estimation methods based on ML approaches providing a comprehensive cross-publication comparison between different methods, providing the guidelines for future work.

12. Development of a method to train and improve the robustness of the SOC estimation models regarding gains error and offsets generated by the sensors used to collect the model input data.

13. Shows the importance of considering the estimation error discrepancy from models due to multiple local minima.

14. SOC estimation using a single NN applied to a 12V Hybrid Energy Storage system composed by a Li-ion (LFP, 8Ah) and Lead-acid (60Ah) 12 V batteries, for Micro-Hybrid application.

15. Development of a Li-ion cell model using long short-term memory recurrent neural network to estimate the cell terminal voltage for different batteries and a wide range of temperature conditions.

16. A comprehensive comparison between the third-order Equivalent Circuit Model and battery voltage models based on long short-term memory recurrent neural network, and gated recurrent approaches.

17. Introduction of Transductive Transfer Learning applied to improve the development of SOC estimation models using long short-term memory recurrent neural networks.

18. Development of a SOC estimation model based on Feedforward Neural Network with exogenous memory based on Butterworth filters.

19. A comprehensive comparison between Feedforward Neural Network with exogenous memory and long short-term memory recurrent neural networks.

1.3. Organization of the Thesis

This thesis presents a combination of analytical research and deep neural Network methods used to propose advancements in xEV Li-ion battery state-of-charge at a wide range of temperatures. The thesis is organized as follows:

Chapter 2 presents an introduction of Li-ion batteries, battery modelling, state estimation methods, and finally, a literature review on the effects of low-temperatures effects on electrified vehicle energy storage systems. The low-temperature effects are classified into nine categories: Capacity loss, Power loss, Life degradation, Safety hazard, Unbalanced capacity, Charging difficulty, Thermal Management complexity, Battery modelling complexity, and Incremental costs.

Chapter 3 provides a comprehensive review of the state-of-the-art regarding the application of Machine learning methods to state-of-charge and state-of-health estimation for xEV application. It also presents a critical cross publication comparison between all the methods as well as offers a guideline for future benchmark between models, including the indication of publicly available high-quality Li-ion battery datasets, crucial for the quality for any model created based on data-driven approaches such as machine learning. The chapter also presents the results of 100 models trained for state-of-charge estimation, showing the variability of results due to multiple local minima; it is a vital factor to consider for any machine learning benchmark work.

Chapter 4 presents a non-recurrent deep neural network design for Li-ion state-of-charge estimation at multiple temperatures. This chapter presents how the model based on the feedforward neural network structure is built and how the model is trained, including a novel method to improve the model robustness against sensors gains and offsets that generate noise to the model inputs and can damage the state-of-charge estimation. The batteries' data acquisition and preparation are presented and discussed. It also reinforces the effect of multiple local minima on the variability of results by showing the result of one thousand models.

A novel model designed to estimate the state-of-charge of a 12 V Hybrid Energy Storage System composed by one Li-ion and a Lead-acid battery is presented, and the results discussed and analyzed.

Chapter 5 introduces a novel Equivalent Circuit Model approach using long short-term memory recurrent neural networks. The model was trained and tested on large datasets from different Li-ion batteries at multiple temperatures. The model performance is initially compared to a third-order Thevenin Equivalent Circuit Model, showing considerable advantages, especially at lower temperatures. The new modelling approach is further compared to a similar recurrent neural network using gated recurrent units. Both models have their performance compared using approximately the same number of parameters and the same battery dataset at four different temperatures.

Chapter 6 presents a novel method based on the use of Transfer Learning applied to improve the state-of-charge estimation modelling using long short-term memory recurrent neural networks. The concept of Transfer Learning has been introduced as well as the Long Short-Term Memory modelling approach. To validate the Transfer Learning method, four different test cases were presented and applied to four different Li-ion types.

Chapter 7 provides a comparative analysis between two deep neural networks state-of-charge estimation modelling approaches, one using the recurrent neural network with long short-term memory and the other a feedforward neural network with exogenous memory. Feedforward neural network design process includes the selection of the number of layers, parameters as well as selection between two different filtering methods, moving average and Butterworth. The two modelling approaches are extensively compared under a varying number of parameters,

temperatures, trials, and special situations. Two very distinct Li-ion batteries are used in this work.

Chapter 8 provides a summary of the thesis, the major conclusions and the recommendations for future research.

2. LITHIUM-ION BATTERIES, MODELS, AND THE EFFECTS OF LOW-TEMPERATURES ON ELECTRIFIED VEHICLE ENERGY STORAGE SYSTEMS

2.1. Problem statement

To overcome the low-temperature effects on Li-ion batteries, it will be necessary to gain more knowledge about the issue before proposing the development of practical solutions. The main goal of this chapter is to present some basic concepts of Li-ion batteries, batteries models, and a comprehensive review of Li-ion battery low-temperature effects for xEV. This chapter is divided into two main parts, where part one is composed of an introduction of Li-ion battery, and an introductory discussion about energy management systems, battery models, and state estimation methods, and part two a comprehensive discussion about nine classified low-temperature effects on the Li-ion, including some possible solutions presented in the literature.

2.2. Lithium-ion battery

The first Li-ion battery to be widely commercialized and capable to power devices, such as laptops and cellphones, with superior quality than any other battery chemistry previously in the market was the Lithium Cobalt Oxide (LCO/graphite), with graphite anode, created by Professor Goodenough and commercialized by SONY[24][25]. The creation of the LCO/graphite helped the rebirth of the modern electrified vehicles, and in this article, it will be used to exemplify some of its electrochemical reactions:

Positive electrode $\qquad CoO_2 + Li^+ + e^- \underset{Charging}{\overset{Discharge}{\rightleftharpoons}} LiCoO_2$

Negative electrode $\qquad LiC_6 \underset{Charging}{\overset{Discharge}{\rightleftharpoons}} Li^+ + C_6 + e^-$

Net cell reaction
$$LiC_6 + CoO_2 \underset{Charging}{\overset{Discharge}{\rightleftharpoons}} LiCoO_2 + C_6$$
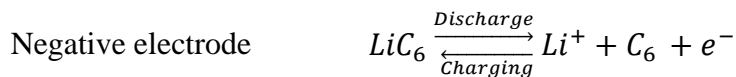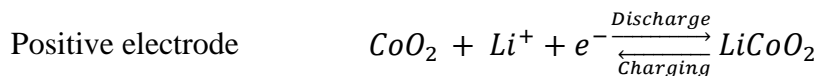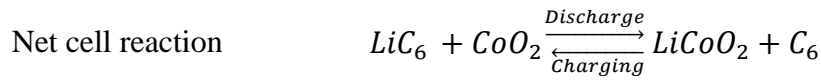
$$E^\circ = 3.7 \text{ V (cell voltage)}$$

The cations of Lithium (Li^+) are physically transferred (diffused), from the cathode ($LiCoO_2$) to the anode (LiC_6) during the charging process, with the process reversed when discharging. The ions pass through a porous separator and are inserted inside the active material crystalline structure on both electrodes. In [26]–[28] visually represents the electrodes structures in further detail, where the x and y indicate the Lithium proportion inserted inside of the electrodes, which values vary between 0 and 1, but the typical value of y for real cells are valued between 0.5 and 1 [28]. The Li-ion cell is also composed by a liquid electrolyte, normally composed by lithium salt, such as $LiPF_6$, and a non-aqueous organic solvent, e.g. ethylene carbonate. The electrolyte resides inside the separator and the pores of each electrode structure, facilitating the Li^+ transport.
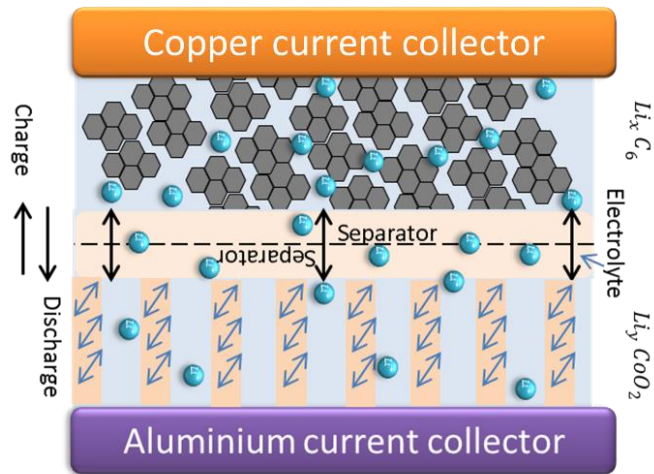
Figure 2.1 LCO/graphite Li-ion battery internal reactions[2]

2.2.1. Battery Capacity

One of the most basic information necessary when choosing a Li-ion to compose

an ESS is the battery capacity, although generally represented by a single value,

e.g. 5 Ah, it is not a constant value and is relative to other variables, including,

the battery chemistry, current, and temperature. The battery capacity is defined

as the amount of electrical charge stored in the battery over time and is commonly

measured in Ampere-hour (Ah). Although, some ESS requirements can be

expressed in terms of Battery Energy, which is a related measure, defined by the

product of battery capacity and Nominal Voltage, and is commonly measured in

Watt-hour (Wh).
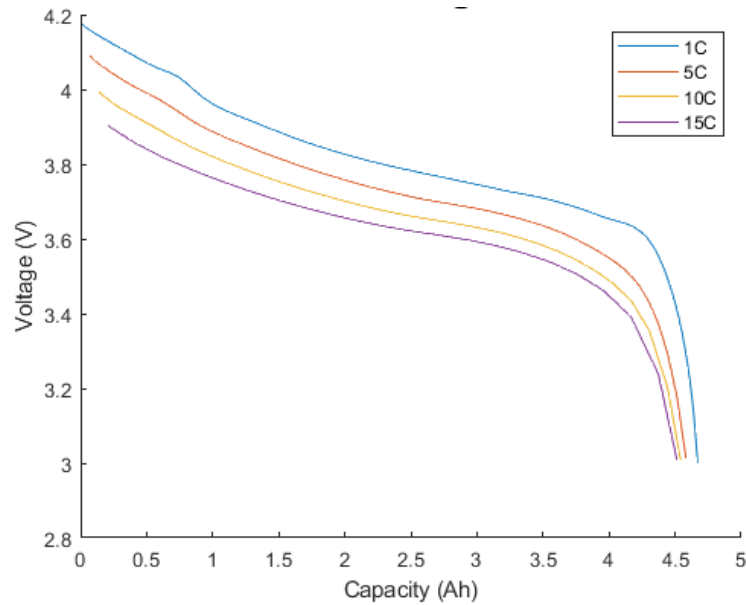
Figure 2.2 The capacity variation as a function of the current rate, when a constant current discharge and voltage from 4.2V to 3V @ 25 ⁰C is applied to an LCO/graphite cell [7].

Li-ion battery capacity can vary as a function of the applied current rate, as illustrated in **Figure 2.2**. The LCO cell, in this example, has an operational voltage limit from 4.2V to 3.0 V, although this voltage range can also vary according to the chosen chemistry [29].

Battery current rate is typically measured in C-Rates, where a 1C rate is equivalent to transferring the total battery capacity in one hour. If twice this capacity is transferred in one hour, the rate would be referred to as a 2C, and the battery would be expected to accept/deliver this capacity in ½ hour.

The capacity response to different current rates will also depend on the chemistry of the cell, actual state of health and its design [10]. On the example shown in **Figure 2.2**, the capacity reduced from 4.67Ah to 4.51Ah at 25⁰C, when

respectively using constant current of 1C and 15C[30]. The temperature can also influence the Li-ion capacity, as it can affect the speed in which the electrochemical reactions occur. Further details about the temperature effects on Li-ion will be discussed later in this article.

One way to express the non-linearity of the battery capacity response to different current rates is using the Peukert equation (2.1), where Cp is the capacity of the battery in Ah, I is the discharge current, n and K are Peukert constants that can be experientially obtained and should vary according to the chemistry and cell design[31]. Although simple to calculate, the Peukert equation is not suitable when the application requires a high variation of current, such as xEVs, which consequently requires more accurate mathematical representations.

$$Cp = KI^{(1-n)} \tag{2.1}$$

Another limitation of this equation is that it does not consider the influence of temperature, although some modifications can be implemented to include the influence of the temperature[32], [33].

2.2.2. Battery Power

The available battery power is influenced by the variation of temperature, due to the temperature-based impedance variation, intrinsically connected to how fast the electrochemical reaction occurs inside the cell.

In most cases, when high currents are required over a short period of time, the above-mentioned reactions occur on the most external area of the electrodes, polarizing the electrodes until the cell reaches its cut-off voltages.

Polarization is a deviation of the actual voltage from equilibrium, open-circuit voltage, dominated by both electrical and diffusion resistance on the electronic and ionic flow, respectively, which directly cause the cell voltage to drop or to rise[29], and can simply be described as the difference from the open-circuit voltage (OCV) and the terminal voltage [8], [31].

2.2.3. Battery Life

Li-ion batteries may suffer from life degradation due to a combination of factors, including relative current rates, number and depth of charge/discharge cycles, storage conditions, and operation under high or low temperatures. The ideal temperature for Li-ion to operate is between 15℃ to 35℃, although, it is acceptable for xEVs applications to work from -20℃ to +60℃[34].

Measuring the capacity fade of the battery is one way to verify how the battery is degrading and use this information to predict its State of Health (SOH), which is an estimation of how well the battery capacity compares to its previously measured Beginning of Life (BOL) capacity. A general indication of Battery End of Life (EOL) is when the battery reaches 80% of its BOL capacity[35], [36] and may no longer be suitable for a xEVs application.

It is also essential to consider the difference between cycle life and calendar life. Cycle life is related to the number of cycles the battery can support under specific cycle regimes, and the related cumulative amount of Capacity / Energy passed through the battery. Calendar life is the battery life measured in time under specific environmental and states conditions.

To better understand the impact of temperature on the ageing process of the battery, the Arrhenius law can be used to correlate, based on empirical experiments, the temperature effect with the chemical reaction rate, represented by (*2.2*), where *K* represents the chemical reaction rate, *A* the molecules collision rate which increases as the temperature increases, E_A represents the minimum energy necessary to start the chemical reactions, *R* the universal gas constant, and *T* the temperature in Kelvin[37].

$$K = Ae^{-E_A/RT} \qquad (2.2)$$

This temperature versus ageing correlation can be seen in [26], where 1.5Ah 18650 Li-ion cells, NMC:LMO (1:1) cathode with a graphite anode, were cycled at a constant temperature about nine times per day at a 1 C rate between 4.2V and 2.0V. Each cell's capacity was periodically measured by cycling the cell at 25^0C, and SOH is calculated as the capacity degradation. This procedure was repeated at different constant temperatures until the cells' capacity falls below 80% of its initial capacity at 25^0C, e.g. at -20 ^{0}C the cell SOH reaches close to 70% in 10 days or in other words 90 cycles. The measured capacities represented in terms of SOH can be seen in **Figure 2.3**, showing a sudden decrease in the cells SOH as temperature varies either above or below 25^0C. Although, the predominant life degradation mechanisms differ if the battery temperature is found to be above or below 25^0C. It is important to remark in **Figure 2.3** that there are only a few points of measurement for temperatures above and below 25^0C; the solid and dashed lines are only to help visualize the trend. When above 25^0C, degradation of the cathode and the solid-

electrolyte interface (SEI) growth on the anode tends to increase the Li-ion internal resistance and reduce its capacity. When below 25^0C, the Lithium plating formed on the anodes leading to the reduction of cyclable Li^+ is shown to be the predominant factor of battery ageing. More details about the ageing mechanisms at low temperatures will be discussed later in the article.

© 2020 IEEE
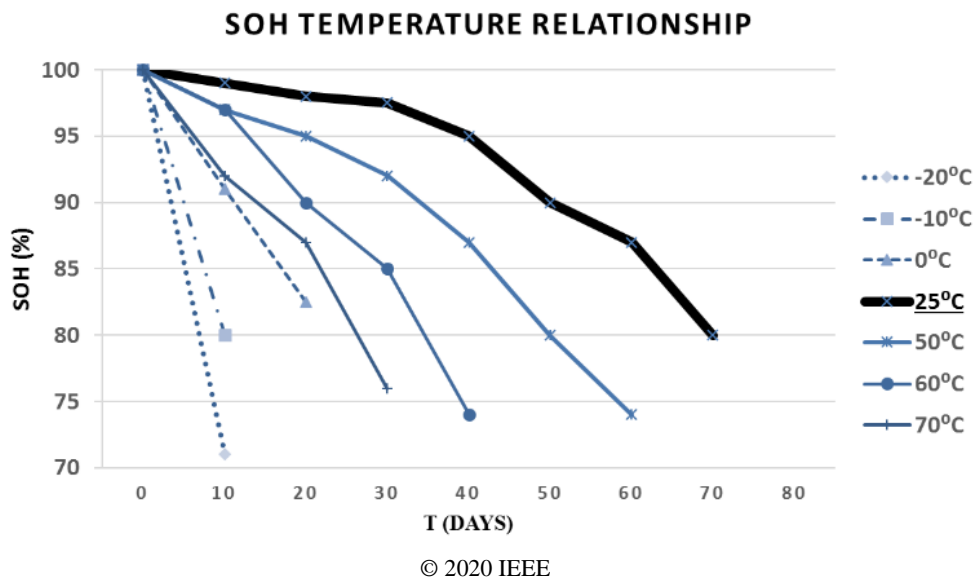
Figure 2.3 NMC:LMO/graphite Li-ion SOH curves at 1C rate and at different temperatures as a function of time [38]**.**

Furthermore, according to [31] even though Arrhenius law helps in understanding the dynamics that lead to battery life degradation, deriving its prediction from one temperature to another may be limited, especially at very low temperatures, e.g. -20℃.

2.3. Battery Models and State Estimation Methods

As mentioned before, an essential component of the ESS is the BMS, which is a system responsible to maintain ESS operation under safe conditions and meet all

required performance criteria. For that is necessary to have a precise estimation of SOC, SOH, State of Power (SOP), and sometimes Remaining Useful Life (RUL). This is not an easy task, due to the non-linearity of the battery, especially for applications such as xEVs, which are subjected to continuously varying current rates, loads and temperature conditions.

This comprehensive vehicle operating envelope has a direct impact on the BMS design, increasing the complexity of the system when compared to applications such as mobile devices, e.g. cellphones and laptops. Much work has been done to date to design BMS based on accurate battery models or battery state estimation methods. This section will discuss two groups of battery models and three methods that are commonly used for battery state estimation in automotive applications. The models' group is the Electrochemical model and Thevenin Equivalent Circuit Model (ECM), and the methods are the Coulomb Counting, Adaptive filters, and Learning algorithms.

2.3.1. Electrochemical Model

Electrochemical Models are based on the physical properties of the battery, including the investigation and modelling of internal electrochemical phenomena. Electrochemical Models can be a very accurate modelling method because they can mathematically represent the internal phenomena of the battery.

Their most significant shortcoming is that requires considerable effort to gather all the parameters necessary to build the model [39]–[41] and they tend to become even more complicated when it is necessary to parametrize the model to an

extensive range of temperature and current rates, as it is typically required by the automotive application.

2.3.2. Equivalent Circuit Model

The ECM, based on Thevenin theorem, can represent the battery dynamics reasonably well, using an electric circuit representation with one or more parallel RC (resistance-capacitance), as shown in **Figure 2.4**. As higher the number of series RC elements are incorporated, the higher becomes the polynomial order, and the more complex become the model[42], [43].

The ECM also needs an OCV-SOC relation, which is the relationship between the OCV and the state of charge (SOC) of the battery, obtained experientially, and it will vary for each battery chemistry [33]. A first-order ECM is showed in **Figure 2.4**, where $z[k]$ is the battery SOC at instant k and $OCV(z[k])$, represents the *OCV-SOC* relation in discrete time domain, R_0 represents the battery internal resistance, R_1 and C_1 represent, respectively, the resistance and capacitance responsible for the battery dynamic response in time. The relation of the ECM parameters for the given an example is characterized by (2.3), (2.4), and (2.5) where $i_{R1}[k]$, $i_{C1}[k]$, represent the current in R_1 and C_1 respectively, η .the Coulomb efficiency, and Q the battery nominal capacity, and Δt the time interval.
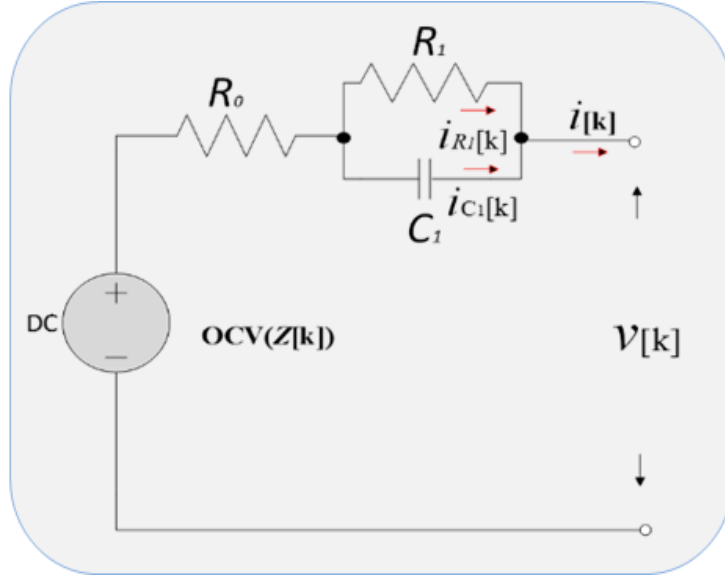
Figure 2.4 ECM using first-order RC network

$$i_{R1}[k+1] = \exp\left(-\frac{1}{R_1 C_1}\Delta t\right) i_{R1}[k] + \left(1 - \exp\left(-\frac{1}{R_1 C_1}\Delta t\right)\right) i[k] \qquad (2.3)$$

$$v[k] = OCV(z[k]) - R_1 i_{R1}[k] - R_0 i[k] \qquad (2.4)$$

$$z[k+1] = z[k] - \frac{\Delta t}{Q}\eta_i[k]i[k] \qquad (2.5)$$

Although, to maintain the model accuracy when submitted to a wide range of ambient temperatures it may require the *OCV-SOC* and R_0 to be as function of the temperature or *OCV-SOC (T)* and $R_0(T)$, where *T* is the battery temperature[42]. As the temperature has significant impact on the battery internal phenomena, for example affecting the diffusion rate, internal resistance and battery capacity. As a consequence, the engineering effort to obtain all the parameters for ECM also increases.

2.3.3. Coulomb Counting

The Coulomb Counting method integrates the battery current over time, calculating the amount of energy flowing in and out of the battery, expressed in Ah. This is a simple and good method, when used on batteries with constant charging-discharging current rates and temperatures. For automotive applications, which have diverse current rates over time, this method tends to accumulate measurement error, caused by current sensor inaccuracies. Another limitation is the necessity to have a precise initial SOC, in order to work properly, but this can be troublesome if the battery SOC vary after hours/days of parking [10], [44], [45]. As the SOC is the ratio of the amount of energy available in the battery and is calculated as function of a fixed rated battery capacity, this method is also prone to even more inaccuracies as the battery temperature varies.

2.3.4. Adaptive Filter Algorithm

The Adaptive Filter Algorithm methods include the following; Kalman Filters (KF), Extended Kalman Filter (EKF), Unscented Kalman Filter (UKF), Sigma Point Kalman Filter (SPKF), Particle filter (PF), $H\infty$ Filter, Recursive Least Square (RLS)[10], [46].

The EKF is the most frequently used method of this group, as KF cannot work with non-linear equations, such as those required for Li-ion batteries. EKF uses linearization techniques applied to the KF, which are self-correcting mathematical equations that iteratively calculate the minimum squared deviation between the estimated and actual states until they reach a convergence solution close to zero.

As for battery modelling, the adaptive filter algorithms work in combination with battery models such as ECM and Conventional in order to improve their estimation accuracy and adaptability [8], [47].

2.3.5.   Machine learning

Machine learning algorithms are useful methods for the calculation of non-linear equations, but in some cases, require large amounts of data to capture all the necessary features and adequately perform the estimation.

In the case of artificial neural networks (NN), the most significant advantage of this method is to be able to estimate the battery behaviour without necessarily gathering any previous information related to the physical battery, such as chemistry or its internal structure. Although this method is highly dependent on the available data and its chosen structure to perform satisfactorily [8], [39]. In **Figure 2.5** is shown a NN structure built to estimate the SOC of a Li-ion battery and a lead-acid battery [19], where it is composed of two hidden layers with respectively four and two hidden units. The complexity of the NN structure can be related to the number of hidden layers, hidden units, the number of input and output variables, as well as how they are interconnected. Other NN variations, such as recurrent neural networks (RNN) and support vector machine (SVM), are also significant to solve non-linear problems, and they can be combined with another method or battery model [8], [50], [51].

In order to predict the RUL, some work has been done using machine learning algorithms[52], [53]. The RUL is a prediction of how much longer the

battery is still capable of providing the required energy and power for a given application. It can be derived from a combination of many variables, such as environmental temperature, SOC, SOH, current rate, calendar life, application, internal impedance etc. For xEVs, the RUL can be considered to be the remaining number of cycles the battery can support but maintaining the minimum vehicle requirements of energy and power, which can influence the vehicle's total life cost. Due to the number of variables and the non-linear response of the battery, the prediction of an accurate RUL remains a great challenge, and advanced machine learning methods, such as Long Short-Term Memory RNN (LSTM) have been used to predict the RUL of Li-ion batteries[54] properly.
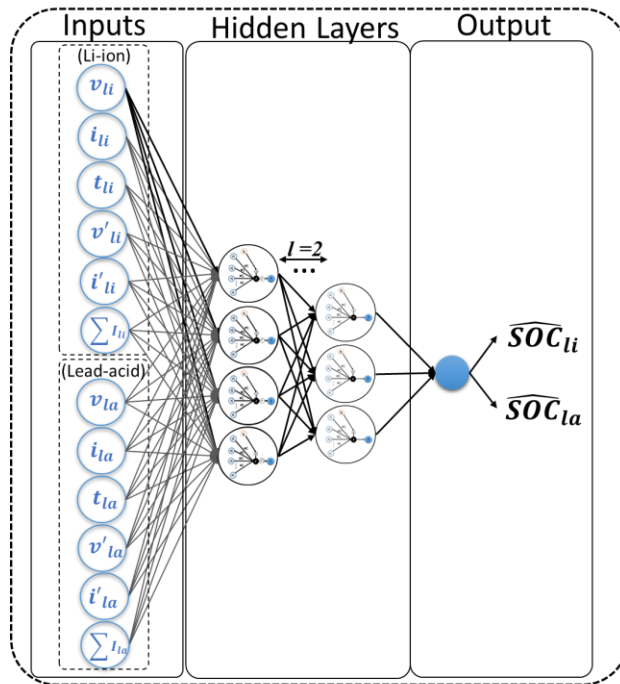
Figure 2.5 Schematic of feedforward three-layer network and 12 inputs for estimating SOC of two batteries

2.4. Low-Temperature Effects on Li-Ion Batteries

In this section, the effect of low temperature on Li-ion batteries will be approached in more detail, subdivided into nine significant effects that directly or indirectly affect the battery operation, seen. It is vital to notice that all effects described here are in some way correlated to each other. This work intends to capture as much as possible the critical aspects related to the operation of Li-ion batteries under low temperatures in xEV application and to help guide the development of solutions to overcome these constraints.

2.4.1. Capacity Loss

When an xEV operates under sub-zero temperature environments, it may impact the Li-ion battery temperature which can lead to a reduction in its range capability. According to a set of studies in Canada [54], [55] the EV range can be change at 1.1 km/℃ rate. The Studies also show that, at -7℃ the vehicle range can be decreased by about 20 %, without any auxiliary load draining energy from the battery, e.g. cabin heat, in comparison to the same condition at 20℃, and it can be reduced by up to 60% at -20℃, with all vehicle auxiliary loads turned on.

The studies showed how significant are the auxiliary loads used to improve the driver comfort during cold weathers are on the range reduction. Not taking into account these auxiliary loads when the battery temperatures are reduced, there is an incremental impedance increase, due to slower diffusion rates in the solid electrodes, electrolyte and SEI, which is further aggravated if the current rate is also increased [31], [33], [34], [37], [56], [57].
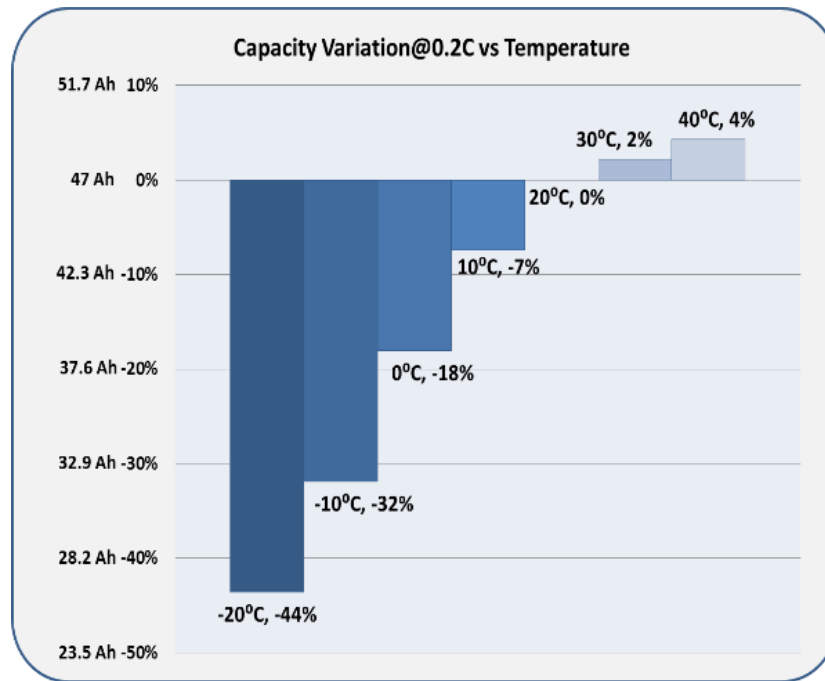
Capacity Variation@0.2C vs Temperature

Figure 2.6 LFP/graphite battery capacity losses at constant low current at different temperatures

When at sub-zero temperatures and when a very low current is applied, e.g. C/10, in a condition that can be considered pseudo-opened-circuit-voltage, a reduction on the nominal capacity can still be observed, due to polarization of the electrodes caused by high electrode activation energies and the ratio between the anode and cathode in the cell design[37]. An LFP/graphite battery capacity loss shown in **Figure 2.6** helps to illustrate these cumulative effects, where the battery lost 44% of its capacity when discharged at only 0.2C constant rate at -20℃, but also increased by 4% when at 40℃ [44], [56].

The battery must control its temperature to overcome or mitigate this issue and keep the vehicle performance in the desired range. Without having to change the type cells, there are many strategies to heat the battery to the targeted temperature

actively. Some strategies take into account the energetic overall cost, which often suggests that pre-heating a battery before driving using an external power source, such as a level 1 charging station (120VAC, 16 A), is energetically more efficient when compared by heating the battery while driving the vehicle [67], [68]. Although, even when pre-heated, the battery will not necessarily be exempt from the requirement to maintain an active heating system during vehicle operation, this should be addressed accordingly to each ESS design.

2.4.2. Power Loss

The battery power capability is directly related to the ability of the battery to deliver high current in a short period, e.g. 5 to 30 seconds[37], [60]. As the batteries are electrochemical devices, they are dependent on both electrical and chemical phenomena that ideally should co-occur, although, this is not true in practice. In the case of Li-ion batteries, this time difference built between demand and response is dependent on the Li-ion diffusion rate in the electrodes, electrolytes and SEI [57].

When the battery operates under low temperatures, the diffusion rate can be significantly reduced, especially in the graphite anode, leading to cell polarization [31], [56], [67], [87]. The higher the polarization, the higher becomes the time necessary for the diffusion to be completed and the lower the resultant battery power capabilities [62]. Batteries with better power capabilities require lower diffusion time/higher diffusion rates, lower internal resistance and lower activation energies [37].

Table 2.1 Li-ion and Supercapacitors specifications

Specification	LFP	NCA	NMC	SC
Specific power (w/kg)	*250-1600*	*700-800*	*500-2400*	*500-100k*
Energy density (kwh/l)	*250-500*	*500-670*	*230-550*	*10-30*
Specific energy (kwh/kg)	*80-140*	*145-240*	*126-210*	*2.5-15*
Cycle life (cycles)	*1000-2000*	*1000-1280*	*1200-1950*	*>100k*
Cost ($/kwh)	*300-600*	*300-600*	*300-600*	*300-2000*

One method to solve or to reduce the negative effects of low temperatures on the batteries is to combine batteries with supercapacitors (SC), which are less sensitive to temperature variations than batteries and have high power densities. The cost and complexity of using such a hybrid energy storage system (HESS) can be a downside for this approach [63]. The specifications of three types of Li-ion batteries, all with anode graphite, and SC are shown in **Table 2.1**, where the cost and power density of an SC can be significantly higher than a Li-ion [10]. Another approach may involve changing the Li-ion cell cathode and/or anode materials and electrolyte composition, or at the system level, heating and use preconditioning strategies [59].

2.4.3. Life Degradation

In case of EVs and in some types of HEVs, the ESS is the most expensive part of the vehicle, which consequently means that the useful battery life has a relevant impact on the vehicle market adoption, and thus it is essential to improve and maintain the vehicles' batteries life [64]. Understanding how the battery ages are

required to better measure and predict its useful life, especially at extreme use conditions such as at high and negative temperatures.

In the case of low temperatures, ageing effects should be even more pertinently applied to countries like Canada which can have more than 100 days per year under sub-zero temperature and may see temperatures as low as -40℃ [12], [54], where even simple vehicle maneuvers can damage battery life[65].

As the battery ages, its performance also gradually fades until it reaches its automotive life threshold, which is generally considered to be when the capacity is reduced to 80% BOL or its internal resistance is increased in 33% of BOL[66]. For Li-ion batteries, it is well established in the literature that lithium plating has a large impact on cell life degradation, leading to impedance increase, loss of active material and safety hazards.

Lithium plating is when Lithium ions deposit as metallic Lithium on the anode surface, rather than intercalating into the anode material, potentially forming dendrites that have the large surface area and that are very reactive with the electrolyte, and incrementally reducing the amount of Li-ion available for the desired galvanic reaction [67]. As more metallic lithium deposits on the SEI, the Lithium will destroy the existing SEI layer, allowing more electrolyte to be consumed, during the reformation of the SEI, and result in a net thickening of the SEI layer. As a consequence, Li-ion diffusion becomes more difficult, and intercalation rates into the graphite electrode become slower [41]. In general, extremely low temperatures and high current rates exacerbate this plating

phenomenon, and the graphite electrode becomes more prone to permanent damage, in turn reducing the life of the battery [68], [69].

Using lithium titanate (LTO) instead of graphite, makes the cell much less sensitive to lithium plating, due to the difference in equilibrium potential that are ~0.1V between Li/Li+ for graphite, but closer to +1.45V for LTO and Li/Li+ [65], [70]. For example, the NMC / LTO (LTO anode), may add cost to the system design as it will require the addition of more cells in series to reach the necessary pack voltage, because of the LTO cell's lower nominal voltage; 2.4V [29], compared to other types of Li-ion batteries that use graphite as their anode material, e.g. NMC/graphite (3.6 V), LFP/graphite (3.3V), NCA/graphite (3.6V) [71].

2.4.4. Safety Hazards

Due to its high energy density, intrinsic safety constraints and wide use in xEVs application, the Li-ion battery shall be required to comply with several standards and regulations, concerning the safety of the persons inside and outside the vehicle. The safety requirements, including legal and technical requirements, have a direct influence on the design of the cell, module, ESS and the vehicle, although these requirements may vary from country to country.

The difference between a standard and regulation is that standards are conventions based on the recorded best practices from academia, industry and market, in general, organized by non-governmental entities e.g. SAE (Society of Automotive Engineers) and USABC (formed by Ford, FCA and GM), but are not compulsory, and despite that, it can be referred by regulations, which have the power

of law, e.g. NHTSA (National Highway Traffic Safety Administration)[72]. An example of relevant standards and regulations used for Lithium-ion in the automotive industry are listed below in **Table 2.2**.

Table 2.2 Safety standards and regulations related to automotive battery tests

Region	Standards and regulation
International	SAE J2464, SAE J2929, ISO 12405-1(-2)(-3), IEC 626060-2(-3)
Europe	UN/ECE-R100.02
USA	UL2580, USABC, FreedomCAR
Korea	KMVSS 18-3
India	AIS-048
China	QC/T 743, GB/T 31467.3

© 2020 IEEE

Motivated by the need to improve the safety of the batteries at high temperatures, many studies [73]–[75] have been published to address the concerns related to battery failure mechanisms and their related hazards.

One of the main safety concerns is to avoid thermal runaway; sudden temperature increase, due to uncontrolled electrochemical reactions, leading to the battery destruction and high risk of fire and explosion. It happens due to side chemical reactions not related to the desired galvanic reactions, responsible for charging or discharging the battery, which incrementally generates more heat, and without dissipation, the accumulated heat increases the internal pressure, due to the electrolyte starting to boil, or possibly decompose, thereby increasing the risk of gas leakage, fire and explosion.

Thermal runaway can be trigged by mechanical, e.g. penetration during a car crash, electrical, e.g. overcharging, thermal abuse, i.e. exposure to heat above 80℃

where the thermal runaway may occur spontaneously[67], [74], [76]. A combination of more than one of these factors may increase safety hazards.

One potential failure mode caused by the formation and growth of dendrites originating from Lithium plating is a cell internal short-circuit, which can potentially be followed by thermal runaway. The probability of a thermal runaway event can be aggravated by forcing aged batteries to cycle under extreme temperature conditions and at high current rates, effectively driving the battery to over-charge or over-discharge[67].

Although thermal runaway is unlikely to happen at low temperatures[34], the detection mechanisms of internal short-circuit that trigger the thermal runaway is not well understood and still need additional examination[76]. Furthermore, the only standard that specifies an extremely low-temperature test is the USABC:1999 designed to test the performance and safety of the battery (cell, module and pack) under temperatures down to -40℃[72].

Another safety issue that should be carefully addressed when designing an ESS with Li-ion battery for an EV or HEV is the possible vehicle loss of power when driving at extreme low-temperature conditions, e.g. lack of power when passing another vehicle in a highway during winter. The powertrain control strategy needs to account for that situation, and accurate information of the battery SOP is necessary, notwithstanding the high non-linearity of the battery especially when combining high current demand and low-temperature condition[31], [64], [77].

2.4.5. Unbalanced Capacity

At a system level, the battery can be affected by the inhomogeneous heat distribution in the battery pack [78], which is not an effect exclusive when the battery pack is exposed to low temperatures, although it is always important to be considered in any ESS design.

A battery pack can have as many as thousands of Li-ion cells distributed in different ways in the vehicle, which consequently have some cells operating at different temperatures than others [41]. As already mentioned, at low temperatures, the battery is more likely to lose effective capacity and power capabilities due to slower electrochemical kinetics, increasing battery polarization [7], forcing some vehicle manufacturers to over-size the ESS or to include complex and expensive temperature control systems.

When a few Li-ion cells in the ESS are functioning at a lower or a higher temperature than other cells in the pack, the whole system operating conditions may be limited by the lower capacity cells, in order maintain the safety condition of the pack, and avoiding cells from experiencing overcharge or over-discharge [80]. The capacity loss is aggravated if the temperature difference among cells is higher than 5 ℃ [79], [81], which can also increase the likelihood of Lithium plating when charging at low temperatures [57], [82], [83]. It is then necessary not just to heat the battery system, but also to control its thermal distribution, maintaining the temperature difference among cells below 5℃ [5].

2.4.6. Charging Difficulty

Charging the Li-ion battery at low temperatures can be challenging, as the electric current needs to be controlled to avoid cell and battery over-voltages, which can consequently bring safety and ageing issues. Charging at low temperatures is not always recommended in every situation. For instance, the datasheet of batteries, such as Panasonic 18650 LiNiCoAlO2 specifies that it should not be charged below +10 ℃ [33]. In some cases, however, avoiding charging and operating the xEV battery under low temperatures is not an option, especially in countries like Canada and Sweden [12], [55].

Defining a battery thermal strategy is then crucial to maintaining the performance, life and safety of the battery under cold conditions, whether during parking or driving[59]. Charging the vehicle in cold weather can also double the charging time, when compared to 20℃ charging temperature, partly due to the lower charge rate required at these lower temperatures[84]. Pre-heating the battery before driving can, however, reduce the SOC effective loss to as little as 6%[61] and also improve the vehicle range[85].

To improve charging efficiency of the battery and even allowing fast charging in cold weather, tracking its polarization voltage and SOC, and adjusting the current amplitude and frequency should help to quickly heat the battery, without compromising life and safety[86]. Furthermore, fast charging the battery to a partial state of charge (PSOC) may be less damaging to the battery, than charging close to

100% SOC[87], emphasizing that an accurate SOC estimation is fundamental, for an efficient charging protocol.

2.4.7. TMS Complexity

The objective of an excellent thermal management system is to maintain the battery temperature as close as possible to its ideal temperature operation range, which for Li-ion batteries is from 15℃ to 35℃ [34], under the full vehicle operating envelope. The ESS target set by USCAR for EV commercialization for 2020 requires that the battery should support environmental temperatures from -30℃ to 52℃. Please note that the USABC expects at least 70% of the battery's electrical storage capacity to be available at -30℃ when discharged at C/3. To meet this goal cell-to-cell capacity variation must be considered. Besides should also improve other characteristics, such as cell-specific energy to 350 Wh/kg and system cost to 125$/kWh [88].

Thermal management strategies can include the use of self-heating [34], [89]–[91], cooling/ heating by convection or liquid, use of an internal or external power source[16], [19] phase change materials[92], preconditioning during charging/discharging, new cells design[57] or even the combination of two or more of these strategies[61]. Examples of these strategies have been provided by early experiments and commercialized vehicles, e.g. Tesla Model S, Nissan Leaf, GM Bolt [85], [93], [94]. Some of the strategies are illustrated in **Figure 2.7**.

A mutual pulse heating strategy is illustrated in **Figure 2.7(a)**, where the cells in an ESS are divided into two or more groups and connected by a specially designed dc-dc converter. The cells are uniformly heated when the DC-DC converter

boosts the voltage of one group to be able to charge the cells in the other group, while in this process, part of the energy is stored in the cells, and the rest is dissipated as heat due to the cells internal resistance. This process is repeated in both directions, from one group to another, with controlled pulse signals to maintain the cell's capacity balanced and mitigate life degradation[90].

In **Figure 2.7(b),** another self-heating strategy is shown, which is characterized by a closed-loop system where the cells use their energy to power a fan and an external resistance. The heat generated by the external resistance is transferred by convection to heat the cells. This strategy has the advantage to heat the cells quickly but may require more space for airflow, fans, and external resistance. Also, this strategy should not heat the cells as uniformly as the mutual pulsed heating strategy. To illustrate a simple cooling strategy, **Figure 2.7(c)** shows an example of an external AC power source, e.g. vehicle alternator, powering a fan to blow the heated air out of the cells.
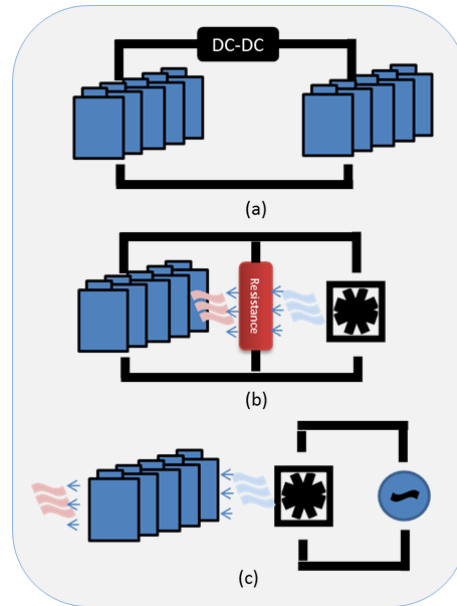
© 2020 IEEE

Figure 2.7 TMS examples. (a) Self-heating by modulating current input and output from a group of the cell to another. (b) Self-heating by convection. (c) Air cooling using an external power source.

For any of the strategies discussed above, an accurate mathematical model may be necessary to simulate the battery response to energy and power demand under different temperature conditions. Modelling by coupling both thermic and electrochemical battery behaviour is one approach to predict the non-linear reaction of the Li-ion ESS. When the battery charges and discharges, it also generates heat, which in cold conditions can be beneficial to the battery performance [8], and it should be taken into account when developing an electrochemical-thermal model [95].

Although, the self-heating effect is considered more relevant to a long-distance trip than for short trips[96], [97] and an imprecise or unrefined TMS may also increase safety hazards; e.g. liquid cooling leakage and short circuit, and may also reduce the battery performance due to thermally unbalanced cells[41], [98].

Table 2.3 shows the distribution of types of TMS currently in use by major xEV manufacturers in the world [99]. Forced air is related to the type of TMS that requires a fan to blow the air and transfer heat by convection, as shown in **Figure 2.7(b)** and **Figure 2.7(c)**, and Natural airflow is the heat transfers that occur without the need of such devices.

Table 2.3 Type of TMS recently in use by xEVs

TMS/xEV	Liquid	Forced air	Natural airflow	Refrigerant	Peltier & Isolation
HEV	5%	83%	-	12%	-
PHEV	55%	30%	-	15%	-
EV	49%	21%	22%	5%	3%

2.4.8. Battery Model and State Estimation Method Complexity

The battery mathematical model, as well as the methods used to estimate the battery states, are critical to ensure the vehicle control strategy and driver safety. However, the battery has non-linear behaviour due to its dependency on electrochemical reactions, which also are interconnected with temperature variations[78]. The non-linearity of the battery behaviour tends to increase as the battery temperature decreases[60], forcing the mathematical models to become even more complex to capture the battery behaviour accurately, and then provide precise information to the vehicle energy management system [12]. For example, when designing an ECM to estimate the battery SOC for a wide range of temperatures, the *OCV-SOC* relation and internal resistance should also be a function of the battery temperature. In practice, it could be translated into the creation and use of multiple lookup tables,

one for each temperature or temperature range. As these lookup tables must be embedded in the BMS and computed by a microprocessor, it should increase the computational load of the system when compared to a simpler model, e.g. ECM designed for single ambient temperature with only one *OCV-SOC* lookup table.

The difficulty to accurately estimate the SOC at low temperatures also should lead to even higher-order ECM and the inclusion of more parameters, e.g. one or more extra RC pairs in the ECM, leading to further complexity and computational load. It should be harder even to characterize the battery and its parameters for a wide range of temperatures facing the electrochemical constraints imposed by low temperatures. For example, the ability to measure the internal resistance of the battery, at certain current rates, using a hybrid pulse power characterization (HPPC) test method becomes much harder when tested at negative temperatures, as the cut-off voltage is reached prematurely due to high polarization effect[100]. Other techniques, such as electrochemical impedance spectroscopy (EIS) may be necessary to capture the desired resistance parameters[33], [90].

For non-parametric methods used to estimate battery states NN, it is still necessary to collect a large dataset from the battery, which can require more development hours, generating data at different temperatures in test benches [31], [48]. Although, due to the complexity of the battery information encoded in the data for a wide range of temperatures, the NN structure should be adjusted to be able to estimate the desired battery states accurately. This can be done by adding more hidden layers and hidden units. This will increase the number of the NN

parameters[19] that have to be computed by the BMS, leading to higher computational cost.

2.4.9. Incremental Cost

Cost is considered as a product of a chain of decisions, whether good or bad, that can significantly influence the widespread use of xEVs. An ESS using a Li-ion battery can represent close to 50% of the vehicle cost [101], [102]. The cost of the battery cell is derived from its components, materials and processes, but most of the cost comes from the active cathode material, which represents about 20% the cost[103]. It is estimated that when the cost of the Li-ion cell reaches the $100 per kWh, it will be able to compete directly to ICE (Internal Combustion Engine) vehicles in terms of production cost[88], [104].

Battery costs are decreasing considerably since the last decade, from $1000 kWh [6], [44], down to $300 kWh in 2018, due to great investments on increasing production capacity, and improvement to the cells energy density [103], [105]. At a system level, however, there is still room for design improvement, as the ESS can be overdesigned, adding more cost to the vehicle[26], [94]. It is assumed that part of this overdesign is the consequence of the difficulty in understanding and predicting the non-linearities of the batteries under different driving and temperature conditions[26], [106], [107].

The effect of low temperature on the battery cost can be translated as a side-effect, generated from the several technical solutions implemented to overcome the effects of operating under low temperatures, but which can become the problem

itself if increased to the point that will make the vehicle unaffordable or unattractive to costumers[5].

For example, one technical approach that may increase the system and vehicle cost is the use of supercapacitors (SC), together with batteries, which can mitigate several problems related to power capability when operating under low temperatures. The SCs have much higher power density than li-ion batteries and are less sensitive to temperature variations, but, up to now have not been a cost-effective solution as the SC needs to be reduced about to 1/3 of its cost and weight to be commercially attractive for PHEV application[26] [63], [108].

Another technical approach is to use LTO instead of graphite in the Li-ion anode, which makes the cell less prone to lithium plating on the anode [65], [70] and consequently more robust to low temperatures. As mentioned before, this technology may add more cost to the system, especially for high voltage ESS, as it should require more cells connected in series to reach the desired system voltage, since the LTO battery has relative lower nominal voltage, 2.4V[29], compared to other types of chemistries that use graphite as their anode material, e.g. LFP/graphite (3.3V)[71]. In the end, it is all about trade-offs, and even a small advantage in a specific situation, as the battery operation under low temperatures can be essential to help enlarge xEV market acceptance. In **Table 2.4** is shown a forecast for 60kWh battery pack and cells up to 2025 [109].

Table 2.4 Price forecast for 60kWh battery pack and cells

43

60kWh pack	2020 (100k units/year)	2025 (500k units/year)
Cell materials	70-85 $/kWh	55-75 $/kWh
Cell price	110-130 $/kWh	80-110 $/kWh
Cells in pack	$ 7200	$ 5700
Pack price	$ 9000	$ 6950

2.5. Conclusion

The effects caused by the low temperature on the battery are connected. For example, the EV range reduction is, in part related to the use of auxiliary loads used to maintain the comfort of the users and not entirely related to the slower Li-ion diffusion rate, and that even at a pseudo-opened-circuit-voltage, there is still observed loss of battery capacity at extremely low temperatures. The leading cause for power degradation is the growth of SEI, which is exacerbated by irreversible metallic lithium deposition, especially in the case of graphite anodes. Lithium plating is also responsible for the formation of dendrites, and resultant safety hazards increase.

Controlling and managing the temperature is essential, not only regarding the Li-ion cells but also to the entire system, as cell-to-cell temperature variation should be minimized and as uniform as possible to avoid system underperformance or oversizing, adding cost. The existence and combination of these many factors, in general, increase the overall complexity of the ESS, increasing cost and control complexity. However, understanding how they are connected and what are the root causes, become essential to find the best solutions and strategies with a good balance among performance, safety, and cost.

3. REVIEW OF MACHINE LEARNING APPLIED TO BATTERY STATE-OF-CHARGE AND STATE-OF-HEALTH ESTIMATION

3.1. Artificial Intelligence and battery state estimations

Machine learning data-driven approaches to battery state estimation have been driven by recent advances in artificial intelligence [7] in fields such as computer vision and autonomous vehicles. The Venn diagram in **Figure 3.1** shows how the field of AI is subdivided, including Machine Learning and its subsequent divisions of representation learning and deep learning [110]. **Figure 3.1** also shows how the scope of this survey, the state of the art of machine learning SOC and SOH estimation methods for electrified vehicles (xEV), is bounded within the AI field while permeating all subfields of machine learning. **Figure 3.2** shows a structured summary of the SOC and SOH estimation methods considered and analyzed in this chapter. For a comprehensive explanation of ML itself and its basic math, interested readers are referred to [110],[111].

© 2020 IEEE
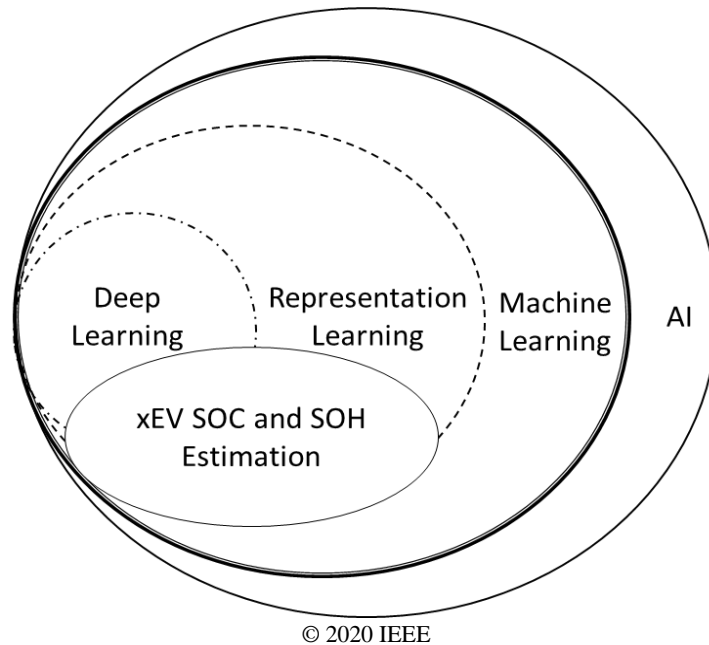
Figure 3.1 Venn diagram [110] **showing the relation of xEV SOC and SOH Estimation to the field of artificial intelligence and machine learning**

As battery technology grows and matures, a significant amount of data is being collected and analyzed in a partially or fully automated fashion [19] to improve battery design and usage. This plethora of data has made it possible to improve BMS performance [20] via big data, the internet of things (IoT), cloud computing, and the ML methods investigated here. In the case of SOC and SOH estimation based on ML methods, the main computational load demanded by these approaches happens during its off-line training phase [21], making it feasible for implementation on typical BMS hardware.

The remainder of the chapter is structured as follows: Section 3.1 reviews ML methods for SOC estimation, Section 3.3 focuses on SOH estimation, and Section 3.3 gives concluding remarks.
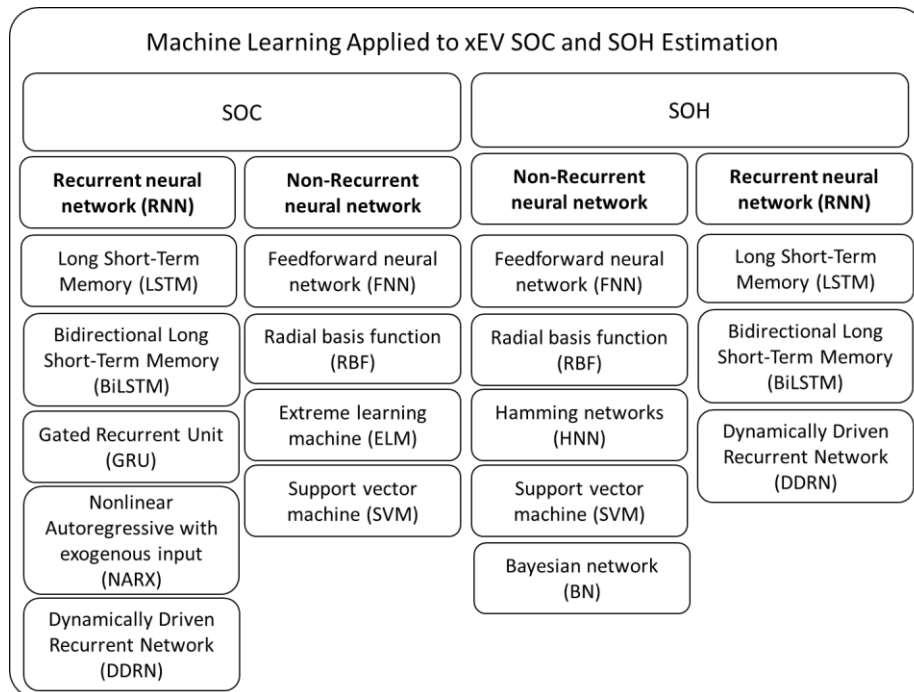
Figure 3.2. Structured summary of the ML methods considered and analyzed in this chapter

3.2. Battery state of charge estimation

This section presents relevant published work regarding the estimation of battery SOC using machine learning methods. The battery SOC is the equivalent of a fuel gauge used in traditional gasoline vehicles. Although, unlike the fuel gauge, to determine the percentage of useful energy left inside the battery, it is necessary to perform an indirect measurement of the SOC via estimation. This is done by a great variety of methods and techniques which use measurable signals such as the battery terminal voltage, current, and temperature[8]. This is not an easy task due to the non-linear nature of the battery. An accurate estimation of the SOC is crucial to improve vehicle performance, safety, passenger comfort, and to minimize costs associated with over design or oversizing of the pack.

In the remainder of this section, different ML SOC estimation methods which have been utilized in the most recent literature will be presented as follows:

3.1.1 Feedforward deep neural network (FNN)

3.1.2 Radial basis function (RBF) neural network

3.1.3 Extreme learning machine (ELM)

3.1.5 Support vector machine (SVM)

3.1.5 Recurrent neural network (RNN)

3.2.1. *Feedforward artificial neural network*

An FNN is a Multi-Layer Perceptron (MLP) that uses no recurrence, only forward pass, to map the non-linearities within the data. It is often used to solve non-convex optimization problems containing several local minima, as discussed in sections

3.2.6 and 4.5. **Figure 3.3(a)** shows a single-layered perceptron, and **Figure 3.3(b)**

an MLP, where x_N^l, W_N^l, and b^l represent the inputs, weights, and bias, respectively

for each single perceptron and F^l the activation function. The subscript l refers to

the layer number, wherein the case of a Single-layer perceptron $l = 1$, and N refers

to the number of input features, e.g. three inputs features, could be Voltage,

Current, and Temperature at certain time-step k.
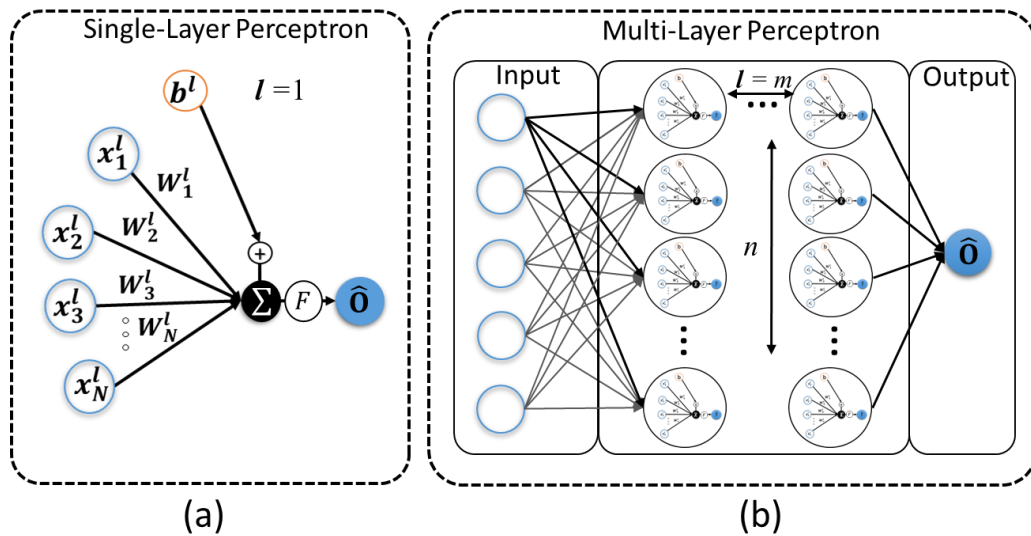
Figure 3.3 (a) Single-layer perceptron, with l = 1, where l is the number of hidden layers, and Ô is the estimation output. (b)Multi-Layer Perceptron, with l = m, n neurons, and output Ô.

The MLP, as the name suggests, is composed of multiple layers and multiple

neurons, which in turn is the equivalent of a Single-layer perceptron in the context

of deep neural networks. Equations (3.1) and (3.2) shows mathematically how these

variables interact, where $\hat{y}^l$ is the estimated output of the neuron at layer l and $\hat{O}$ the

estimated output of the MLP calculated using the outputs from previous neurons

from previous layers, e.g. $\hat{y}_i^{l-1}$ the estimated output from layer l-1 and neuron i used

to calculate $\widehat{O}$. The transfer functions F used in this work are represented by a hyperbolic tangent (3.3), sigmoid function (3.4), and rectified linear unit (RELU) (3.5).

$$F^l\left(\sum_{i=1}^{N}(W_i^l x_i^l) + b^l\right) = \hat{y}^l \tag{3.1}$$

$$F^l\left(\sum_{i=1}^{N}(W_i^l \hat{y}_i^{l-1}) + b^l\right) = \widehat{O} \tag{3.2}$$

$$F(x) = \frac{2}{1 + e^{-2x}} - 1 \tag{3.3}$$

$$F(x) = \frac{1}{1 + e^{-x}} \tag{3.4}$$

$$F(x) = max\,(0, x) \tag{3.5}$$

$$RMSE = \sqrt{\sum_{i=1}^{N}\frac{\left(\widehat{O} - O\right)^2}{N}} \tag{3.6}$$

From the perspective of supervised learning algorithms, the learnable parameters, weights and biases, are iteratively adjusted to minimize the loss between the estimated value and a given objective function O. The loss function used in this work is the RMSE (3.6). The error is backpropagated by calculating the partial derivative of the loss relative to each learnable parameter to use it to update its value [110]. The process is iterative, repeated several times to reduce the loss or until meeting the training stop conditions.

3.2.1.1. FNN combined with filters and other models

A hybrid approach, which has combined the use of an ECM and FNN, was presented by [112], which, instead of using a look-up table (LUT) to correlate the battery SOC to the battery OCV, an FNN model was trained to make this correlation.

The FNN structure was formed by one input, the OCV, a hidden layer with *m* neurons, and the SOC as its output. With the FNN model capable of correlating the SOC based on the OCV input, an ECM was developed to estimate the OCV based on the battery terminal voltage. In [113], and FNN was built to estimate the SOC of an LFP battery and an Unscented Kalman filter was then used to improve the SOC estimation accuracy. The FNN presented in [113] is a supervised ML algorithm, which is characterized by the use of a known reference or target employed to calculate the ML output estimation error. To train the FNN in this work, a set of battery data was acquired using the automotive homologation driving cycles US06, FUDS and the dynamic stress test (DST) specified by the U.S. Advanced Battery Consortium (USABC). Although, in this case, the amount of data seems to be a very narrow representation of the application domain, which can explain the relatively low accuracy when tested in the US06 dataset, as shown in **Table 3.2**, despite the use of UKF to improve the accuracy.

3.2.1.2. FNN directly used for SOC estimation

A work using an FNN, but without the use of a Kalman filter, was presented in [19] for a 12V hybrid energy storage system. This system was composed of a 12V LFP battery and a 12V lead-acid battery to power a belt starter generator system where the electric machine functioned as either a motor or generator according to the control strategy, which kept the Li-ion battery cycling within a partial SOC window. An FNN was developed to simultaneously estimate the SOC of both batteries using the same neural network structure. However, a benchmark

comparison with two separate single-output NN models that estimate SOC of each cell type was not performed. Such comparison needs to be further investigated to clarify the benefits of the shared NN dual SOC estimation output approach.

Because different sources influence the Li-ion batteries' characteristics, e.g., SOC, SOH, current, and temperature [9], the authors in [114] have considered the use of the battery polarization states as inputs for an FNN model trained to estimate battery SOC. The polarization states can have a significant influence on the battery terminal voltage [115] and can be calculated from the battery current using equation (3.7), where S_k is the polarization state at sample point k, Δt_i the sampling interval, N the number of parts within the interval Δt_i, $i_{L,k}$ the battery current, and τ the time constant that can have any integer value from 0 to 1000.

$$S_k = exp\left(-\frac{1}{\tau}\sum_{i=k}^{N} \Delta t_i\right) S_0 + \left(1 - exp\left(-\frac{1}{\tau}\sum_{i=k}^{N} \Delta t_i\right)\right) i_{L,k} \qquad \textbf{(3.7)}$$

The authors have investigated the use of different values of τ and multiple polarization state inputs. In the end, four values of $\tau = [2,6,32,155]$, were chosen for the four polarization states, together with the battery current, voltage, and temperature as inputs to the FNN. The FNN was trained and tested with measured data from an NCA cell for ten standard drive cycles including the EUDC, HL07, HWFET, LA92, NEDC, MANHATTAN, NYCC, REP05, SC03, and UNIF01, each performed at ambient temperatures of -10ºC, 0ºC, 10ºC, and 25ºC. From the entire dataset, 80% was used to train and the remaining 20% for validation and testing. The model was further tested in the lab on a Hardware In the Loop (HIL)

system. This chapter is an example of a thorough study that includes a complex dataset and a good division of training and testing data.

In [21], the authors have shown that the FNN is capable of estimating battery SOC at different temperatures, including temperatures as low as -20°C. Although FNNs are not capable of storing and using past information from a time series, it is possible to encode this information partially by creating new input features based on the moving average of the battery terminal voltage and current. This technique seems to work well as the results obtained are equivalent to those obtained by RNNs, which will be discussed in detail in the next section. Here the authors have systematically evaluated different numbers of neurons, the number of hidden layers, and the average based on two different sample windows (100 and 400 timesteps).

The FNN architecture used in this work is depicted in Figure **3.4**, where the inputs are the battery terminal voltage *V(k)*, battery temperature *T(k)*, averaged terminal voltage V_{avg}, averaged current I_{avg}, and the output is SOC at timestep *k*. The best result at 25°C was obtained when a rolling window of 400 timesteps was used. As expected, the errors are much higher at −20°C due to the low-temperature effects on the li-ion batteries [9]. It was conjectured that it might be improved if a larger dataset was used, and a more complex FNN was built to capture all the complexity presented at low temperatures. Another contribution from the authors shows that using so-called augmented datasets can improve the robustness and accuracy of the model by up to 41%.
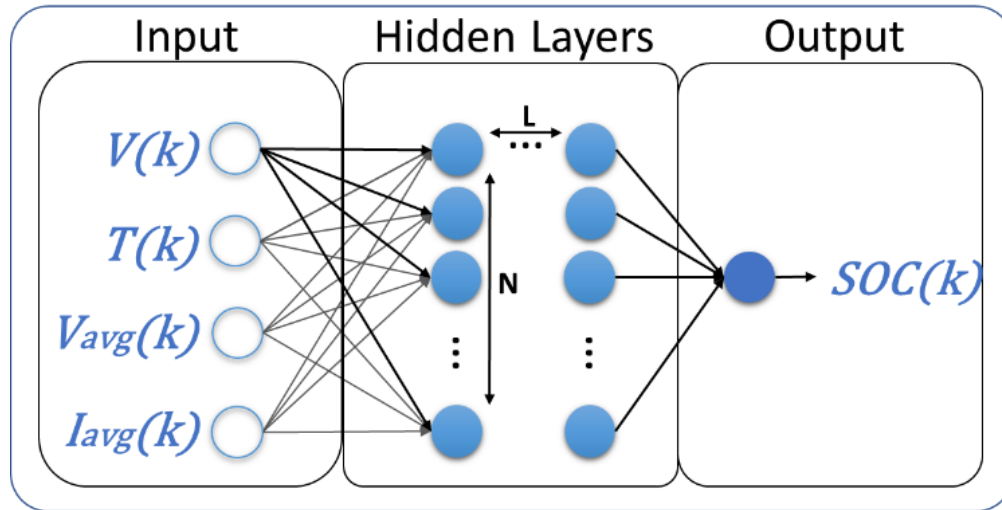
Figure 3.4. FNN structure used to estimate battery SOC [21], where the battery terminal voltage V(k), battery temperature T(k), averaged terminal voltage V_{avg}(k), and averaged current $I_{avg}(k)$, are used as input, and the output is SOC at timestep k

In [116], the authors have used the internal resistance data obtained from a tester in the lab, along with the voltage, current, and battery temperature, to train and test an FNN to estimate SOC. However, the use of the internal resistance would be a valuable input feature, not only for SOC but also for SOH estimation; its direct measurement in a vehicle would be difficult due to practical reasons. Alternatively, using a model to estimate the battery's internal resistance is possible and can be implemented onboard to provide real-time input information [117].

The authors in [118] introduced a process to systematically alter the FNN structure using offline optimization algorithms to find the optimal FNN structure. The work has focused on the backtracking search algorithm, an optimization algorithm, which according to the authors is easier to implement, faster, and more robust when compared to other algorithms, such as a genetic algorithm (GA), particle swarm optimization (PSO), and artificial bee colony. The backtracking

search algorithm (BSA) was set to optimize the number of neurons in the hidden layer and the learning rate value. The procedure of this work was divided into four stages. In the first stage, the data was collected from a 18650 NMC lithium battery cell with 2 Ah capacity using DST and FUDS cycles, then filtered and normalized.

On stage two, the SOC is estimated using a chosen primary structure to calculate the initial cost (root mean squared error) to be used in the next stage. On stage three, the backtracking search algorithm is applied to find the number of neurons in the hidden layer, and the learning rate in which makes the SOC estimation error the lowest. This procedure was applied with other learning algorithms instead of FNN for comparison, and the battery data was acquired at three different temperatures; $0°C$, $25°C$, and $45°C$. An individual FNN model structure was established using BSA for each dataset at each temperature, and it was noted that at $0°C$, the errors obtained in each method are about double the error when comparing the results at $25°C$. Ideally, one FNN model should be able to handle different temperatures if appropriately trained, as previously shown in [21].

There is a great potential of using optimization algorithms to help determine the FNN structure and therefore reducing the necessity of previous engineering experience to set the "correct" FNN training parameters. Although many other parameters besides the number of neurons and learning rates should be considered, e.g., the number of hidden layers, the initial weights distribution values, it will also increase complexity and the offline computational burden for the search of the optimal structures.

Another unique approach was presented by the authors in [119], where they have trained a model composed of three parallel FNNs, each individually trained with distinct training data from three operation modes, idling, charging, and discharging. Despite the low accuracy and limited data used to train and test the FNN (US06 for validation and testing and pulsed profile for training), the authors have considered the impact of random initial NN weights by performing training 50 times and using the average error as the final result of the method. The authors show that the initial values, which are generally randomly selected when training an NN, can lead to different local minima. Despite the importance of initial parameters on training, their effect on the result is explicitly considered in only a few of the publications presented in this survey.

3.2.2.   Radial basis function neural network

A radial basis function neural network is a class of FNN that contains only an input layer, one hidden layer, and an output layer implementing linear summation. Rather than use non-linear monotonic single-valued activation functions, the hidden layer neurons in an RBF compute a Euclidean distance, multiply it by a (standard deviation related) scaling factor, and map it through a Gaussian function. This is also referred to as a radiated Gaussian kernel function (3.8).

$$\varphi_i(\mathbf{x}) = G\big(||\mathbf{x} - \mathbf{w_i}||\big) = \exp\left(-\frac{||\mathbf{x} - \mathbf{w_i}||^2}{\sigma_i^2}\right) \qquad \textbf{(3.8)}$$

An example RBF neural network is shown in **Figure 3.5**. Rather than determining weight gains in the training process, centroid vectors are fitted in the RBF neural

network training stage. RBF neural networks are also typically characterized as having very fast training/learning and being good at interpolation [46].

A radial basis function neural network with an extended Kalman filter (EKF) was used in [120],[121] for online estimation of the SOC of a Li-ion battery cell and a lead-acid battery. In this work, a battery model was first created using the RBF structure to find the state-space equations for the EKF. The state variables extracted from the battery model were the SOC and terminal voltage from the previous time step. The temperature used in this work was only the ambient room temperature. A similar use of the RBF was presented in [122] and [123], although using extended H_∞ and unscented Kalman filter (UKF), respectively.

In [124], the authors used the RBF to learn the dynamics of a lithium polymer battery cell trained offline with experimental battery data to estimate the SOC. The trained RBF was then used to establish the upper bounds of the system uncertainties adaptively, and to determine a parameter necessary for the determination of the appropriate switching gain which is essential for robustness. Through the Lyapunov stability theory, the sliding variables converge theoretically to the sliding surface and remain there for a finite time until the error asymptotically converges to zero [125]. The upper bound is adaptively updated by an RBF, using the structure in **Figure 3.5**, providing robust traceability and limiting the chattering magnitudes in the SOC estimation. In **Figure 3.5** $\hat{x}$ is the estimated state vector, φ represents the Gaussian function in each of the 9 neurons of the RBF structure and $\hat{\bar{\psi}}$ is the updated upper bound of the system uncertainty.
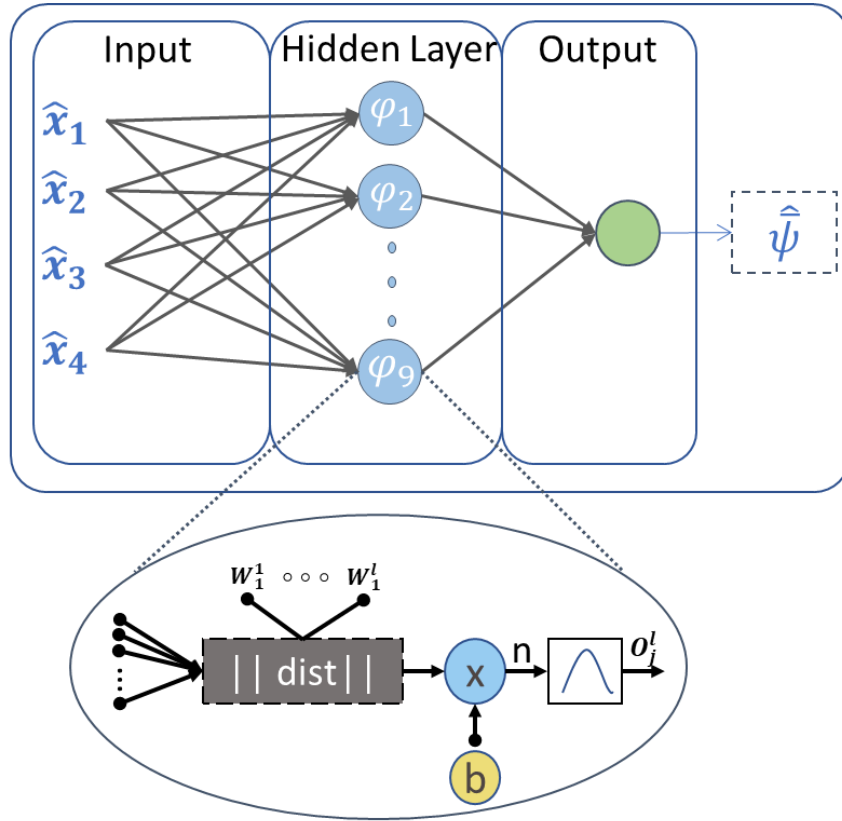
Figure 3.5. Example radial basis function neural network structure

In [126], a multi-cell Li-ion battery pack SOC estimation framework was presented, and an RBF was used to quantify the uncertainties necessary to build a response surface model of model bias. In this work, the model bias δ is the stochastic difference between the estimated and measured li-ion cell terminal voltage. This is motivated due to the intrinsic differences between each cell in the battery pack, which makes it challenging to track their dynamics accurately. After quantifying the parameter uncertainties using the RBF, it was possible to apply the average pack model to each cell and have a better estimation of the terminal voltage. Then an adaptive extended Kalman filter (AEKF) was applied to perform an online SOC estimation of the entire pack.

3.2.3. Extreme learning machine

The extreme learning machine (ELM) structure is very similar to an FNN, but the main difference consists of its training algorithm, which instead of using backpropagation, the ELM uses the Moore-Penrose generalized inverse or pseudoinverse matrix [127]. In [128], the authors used an ELM to model a Li-ion battery from experimental data; then, the SOC estimation was approximated using a KF. The ELM method was compared with an RBF showing lower computational load and better SOC estimation error. Besides, four different KF algorithms were compared: EKF, AEKF, UKF, and adaptive unscented Kalman filter (AUKF). As shown in **Figure 3.6**, the ELM was used to estimate the battery terminal voltage $V_{(k)}$, based on the battery current $I_{(k)}$, $SOC_{(k)}$ using SOC-OCV relation, and $V_{(k-1)}$, which is the terminal voltage from the previous sample step.

The ambient temperature used in this work was $25°C$, and the number of neurons used was 10 and 15 for both ELM and RBF, respectively. The ELM was up to 50% faster when compared to the RBF estimation time and have provided lower estimation error. Moreover, the use of the AUKF for SOC estimation improved its accuracy and reduced the computational load, even when comparing with other variations of KFs.
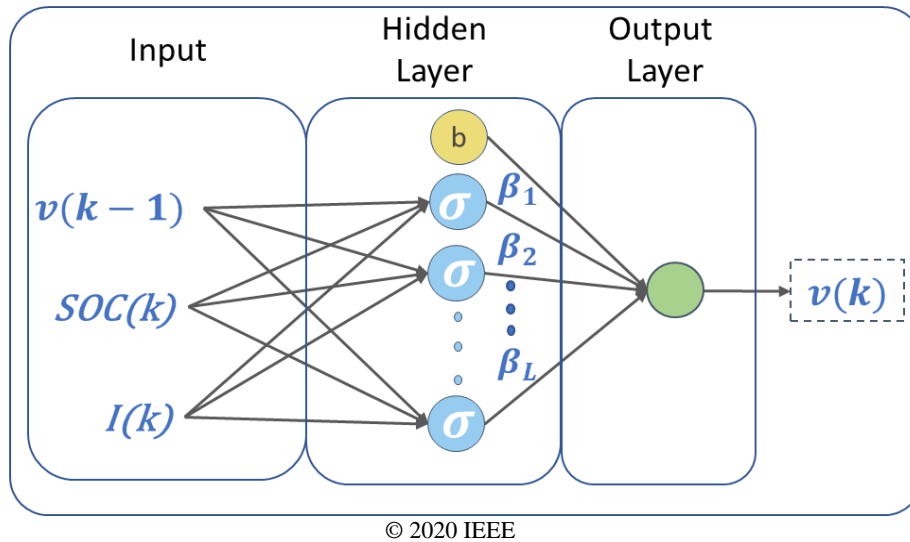
Figure 3.6. ELM network structure to model the battery terminal voltage [128]

In [129] the authors have used the gravitational search algorithm (GSA) to find the optimal number of neurons in an ELM with one hidden layer for two different drive cycles, US06 and Beijing dynamic stress test (BJDST) at two different temperatures (25ºC and 45Cº); however, they have used what seems to be a limited dataset to validate the generalization capability of the ELM model for xEV applications.

Instead of training and validating the model using different drive cycles, only a portion of the same drive cycle data was used to train and validate the model, 70% for training and 30% for validation. Their use of optimization algorithms seems to be a promising path to automate the process of ML structure selection.

3.2.4.   *Support vector machine*

The SVM was initially created to solve logistic/classification problems. In most cases, battery SOC estimation requires a regression learning method, which sequentially minimizes the error function. The generalized regression variation of

SVM, known as support vector regression (SVR), can be employed. This technique aims to solve a regression problem for data that is not linearly separable. This approach shares some similarities to the RBF methods previously described. However, a crucial distinction is that SVR aims to employ simplified optimization routines such as quadratic programming with linear constraints to fit the SVR parameters. Moreover, the concept of an error tolerance margin is used such that no cost function penalty is applied to the fitting error if it is within some defined error band; this, in principle, should stabilize the estimation.

In [130], an SVM was applied to estimate the SOC of a 60Ah LFP. The concept of a kernel was used to compute the support vectors. The most popular kernel is RBF, similar to equation (3.8); however, polynomial kernels are also possible [131]. The fitted support vector lies in a high dimensional hyperspace; in particular, 903 support vectors were found to be optimal in this case. The battery data in this work was obtained from a dynamic profile where the terminal voltage, current, and ambient temperature were employed. Similar work based on data from a 100Ah cell was performed by the same research group in [131].

3.2.5. Recurrent neural network

In this section, different types of RNNs are introduced, and the most critical points found in recent publications are discussed. Various RNN machine learning methods that are strong candidates for SOC and SOH estimation are presented.

3.2.5.1. Introduction to RNNs

The recurrent neural networks are a subtype of neural Networks that can reuse information from previous time steps in a closed-loop, i.e. a piece of information used or processed during time step *k-1* can be used to help compute a task at the time step *k*. The use of recurrence can add to the RNN the capability to encode contextual information to the model, which makes it suitable to solve problems where past information are relevant to estimate or forecast outcomes, e.g. stock market forecast, battery SOC, the driving situation [13], [132], [133].

Although some RNNs can present limitations to encode long-term dependencies from the data into the model, due to the "vanishing" or "exploding" gradient that happens during the backpropagation [134]. The backpropagation is part of the RNN training process as it is for FNN, as previously discussed.

To further improve the RNN, gated regulated RNN, such as Long Short-Term Memory (LSTM), bidirectional LSTM, and gated recurrent unit (GRU), use a set of "gates," and hidden states that help the RNN learn long-term data dependencies embedded in the data and reuse it when necessary. The LSTM was first introduced in [135] where its memory block is composed by a memory state (3.9), where $\odot$ represents an element-wise multiplication, a forget gate (3.10), current memory candidate (3.11), an input gate (3.12), an output gate (3.13), and the hidden state (3.14). In the equations mentioned above, the R, W and b represent the RNN recurrent weights vectors, input weights vectors, and biases vectors, respectively.

Their subscripts represent which gate it belongs, e.g. W_f weight vector from the forget gate f_k. Finally, Ψ represents the input matrix.

$$C_k = f_k \odot C_{k-1} + i_k \odot \widetilde{C}_k \qquad (3.9)$$

$$f_k = \sigma(W_f \Psi_k + R_f h_{k-1} + b_f) \qquad (3.10)$$

$$\widetilde{C}_k = Tanh(W_{\widetilde{c}} \Psi_k + R_{\widetilde{c}} h_{k-1} + b_{\widetilde{c}}) \qquad (3.11)$$

$$i_k = \sigma(W_i \Psi_k + R_i h_{k-1} + b_i) \qquad (3.12)$$

$$o_k = \sigma(W_o \Psi_k + R_o h_{k-1} + b_o) \qquad (3.13)$$

$$h_k = o_k \odot Tanh(C_k) \qquad (3.14)$$

To help build an intuition on how the LSTM works it can be said that the forget gate (f_k) determine how much of the previous information stored in (C_k) should be erased, the input gate (i_k) determines how much of the current information should be considered to compose the memory candidate $(\widetilde{C}_k)$ and therefore be part be of the information that will update the new memory state (C_{k+1}), the output gate will control how much of the new memory state will compose the new hidden state (h_{k+1}) [136]. Figure 3.7 shows a graphical representation of how the gates, inputs and outputs are interconnected within the LSTM layer.
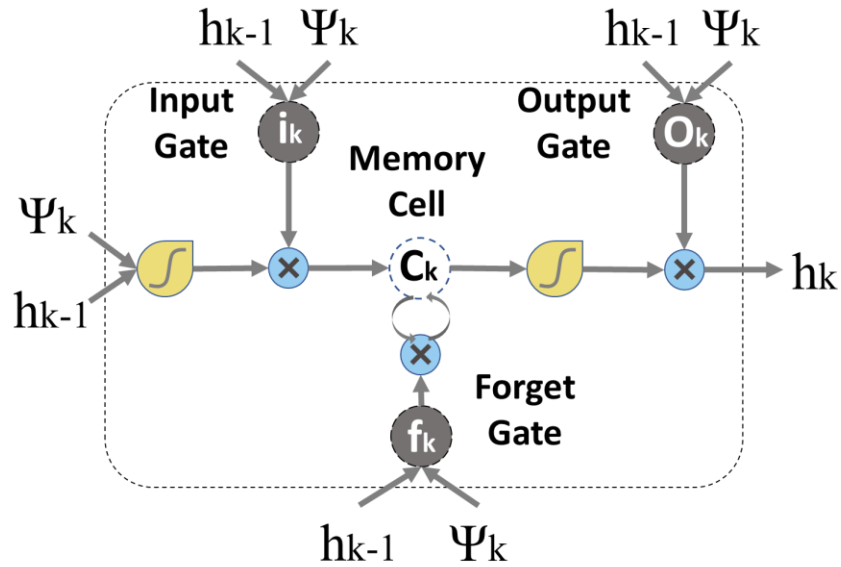
Figure 3.7. LSTM layer [136]. Ψ_k and h_{k-1} **are the input data layer at the current time-step k and hidden layer at the previous time step k − 1, respectively. i_k, o_k, f_k, and C_k are the input, output, and forget gates, as well as the memory cell, respectively**

Due to its cell states and hidden states, the LSTM can also be represented unfolding in time, as shown in **Figure 3.8**, where at each time step k the memory states (C_k) and hidden states (h_k) change their values without modifying the learnable parameters, weights and biases. The weights and bias are only modified during the training process, but the hidden states and memory states can change even after the model being trained and deployed. The depth in time represented by $\widetilde{N}$ determine how much the model will unfold, e.g. in case of using input vectors with 1000 seconds will make the model unfold $\widetilde{N} = 1000$ times at 1-sec time-step. During the training process, the deeper the model, the more historical data it is exposed [137], which may lead to better accuracy.

64
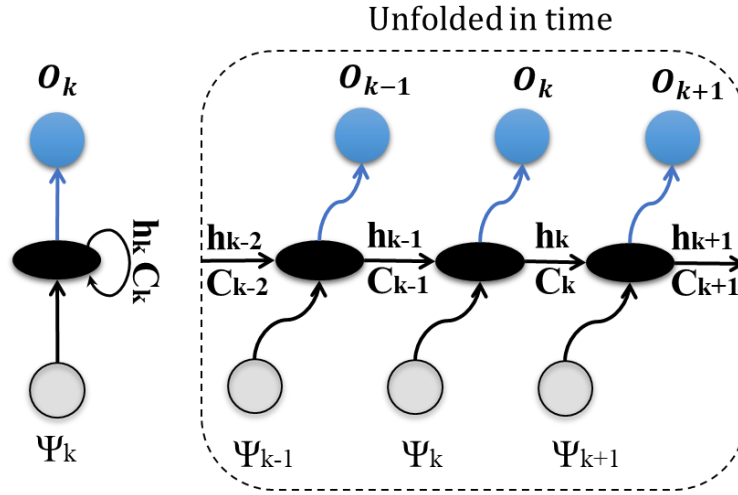
Figure 3.8 LSTM layer unfolded in time

The BiLSTM, a bidirectional version of the LSTM, is a composition of a forward and backward "unidirectional" LSTM layer, where the forward part is fed with temporal input data Ψ starting from the earliest time-step $k - n$ to the current time-step k, $[\Psi_{k-n} \rightarrow \Psi_k]$, and the backward part it is fed in the reverse order, $[\Psi_k \rightarrow \Psi_{k-n}]$ where n is the total number of temporal steps, and y the output of the BiLSTM as shown in **Figure 3.9**. The forward LSTMs are fed simultaneously, and the learnable parameters of each are updated independently, but the outputs of forward, $\vec{h}_k$, and backward, $\overleftarrow{h}_k$, are combined with the function f, which can be either the concatenation, summation, multiplication or average function. The method captures temporal or contextual dependencies from both temporal ends of the data, i.e., commonly used in text translation where the end words or phrases in the text have a significant impact on the overall context and, therefore, on the correct translation. The more samples of the sequential data, one can provide to the model, the more improved performance can be achieved with the BiLSTM before

outputting the estimation, which is a limiting factor for the BiLSTM to be considered.
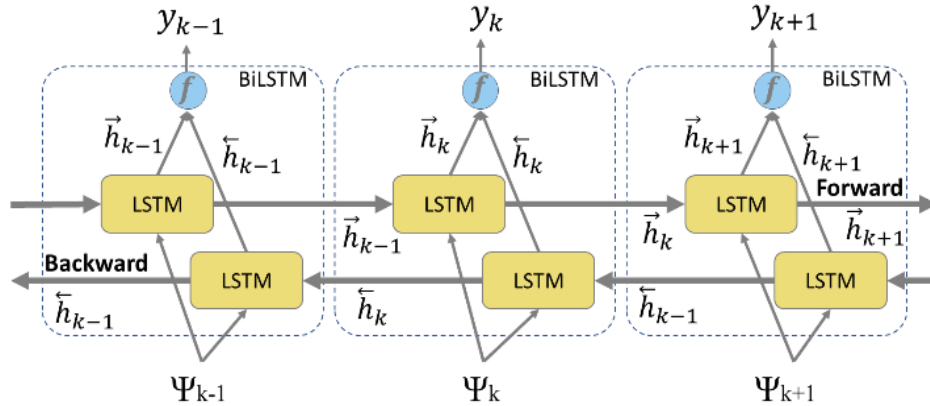
Figure 3.9. BiLSTM layer. From the forward LSTM part Ψk and $\vec{h}_{k-1}$ are respectively the input data at current time-step k and hidden layer at the previous time step k − 1, wherefrom the backward LSTM the inputs are Ψk, and $\overleftarrow{h}_{k-1}$. The BiLSTM output, y_k, are given by the combination of both forward and backward LSTMs, $\vec{h}_k$ and $\overleftarrow{h}_k$, through chosen function f.

Another RNN approach also capable of dealing with long-term dependencies is the GRU shown in **Figure 3.10**, which employs the use of gates to learn, memorize, and decide which information from the past and the present will be used to generate its output. In contrast to the LSTM, the GRU uses a single gate unit to simultaneously control the input and forgetting amount and the decision to update the state unit [110]. The GRU has considerably more straightforward gate mechanisms and than the LSTM and can achieve similar performance [138]. The mathematical representation of the gates and states are represented by (3.15), Reset gate, (3.16), Update gate, Hidden states candidate (3.17), and the Hidden states (3.18), where the *W*, *R*, and *b* represents the recurrent weights, input weights, and bias respective to each gate or hidden state candidate, according to their subscripts.
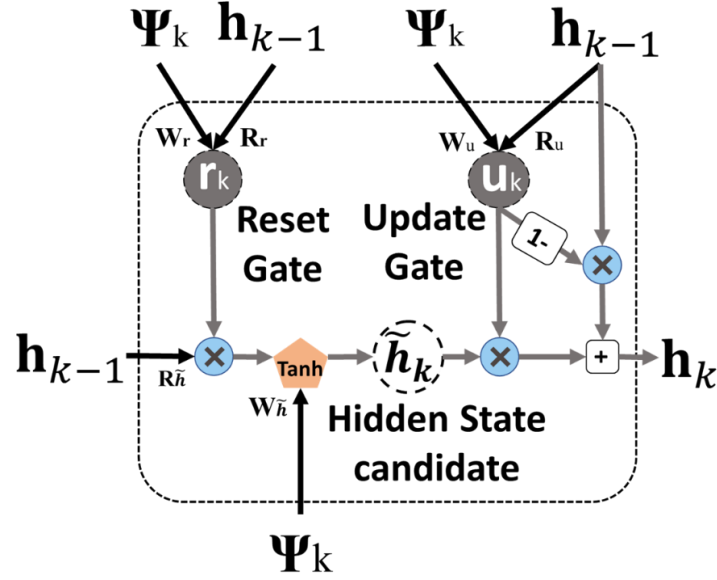
Figure 3.10 The Ψ_k and h_{k-1} are the input data at the current time-step k and hidden layer at the previous time step k−1, respectively. r_k, u_k, and h_k are the reset and update gates, as well as the hidden states, respectively. R and W represent the recurrent and input weights respectively to each gate or hidden state candidate.

$$r_k = \sigma(W_r\Psi_k + R_r h_{k-1} + b_r) \qquad (3.15)$$

$$u_k = \sigma(W_u\Psi_k + R_u h_{k-1} + b_u) \qquad (3.16)$$

$$\widetilde{h}_k = Tanh(W_{\widetilde{h}}\Psi_k + r_k\odot(R_{\widetilde{h}}h_{k-1}) + b_{\widetilde{h}}) \qquad (3.17)$$

$$h_k = (1 - u_k) \odot h_{k-1} + u_k \odot \widetilde{h}_k \qquad (3.18)$$

The remainder of this section is divided into two parts; 3.2.5.2 - Gated RNNs applied to SOC estimation; 3.2.5.3 - Other RNNs applied to SOC estimation.

3.2.5.2.   Gated RNNs applied to SOC estimation

In [137], the authors applied an LSTM to estimate the SOC by using only direct measured battery signals, such as terminal voltage, load current, and ambient

temperature, without requiring it to be coupled with other methods and estimation filters. A considerable outcome presented by this work was the capability to estimate the SOC under different temperatures. This is an advantage compared to methods that require the use of a LUT, from which it is necessary to build one LUT for each different temperature [120]. Although, it is essential to remark that this is only possible if the dataset chosen to train the LSTM includes the necessary information to encode the temperature variation within its parameters, which may lead to a large dataset. The authors used a Panasonic 18650PF Li-ion battery cell dataset acquired at multiple ambient temperatures, ranging from 0°C to 25°C; this dataset is available to download from [139].

A more recent work presented in [140], introduced a stacked BiLSTM model and compared its results with three previous publications [21],[137],[141] as the same dataset was used [139] in all four cases. The BiLSTM showed better accuracy than the other methods when the comparison was done at different temperatures, 0ºC, 10ºC, and 25ºC. Each model in [140] was trained five times, and the average result was used as the final number for comparison, although it is not clear if the other authors in [21],[137],[141] have used training repetition, hence there is difficulty in cross-comparison among publications even though the same dataset was used. The final structure found to be optimal by the authors in [140] was composed of two stacked BiLSTMs each with 64 hidden neurons, which is equivalent to four unidirectional LSTM stacked layers and over 130,000 learnable parameters, the sum of all the weights and biases in the structure. A previous publication [142] has also

used the option to increase the depth and accuracy of the NN by stacking three LSTMs together. The stacking of LSTMs may lead to some constraints, though, such as making the network harder to train, increasing the possibility of overfitting, and increasing the number of parameters.

As a rule of thumb, the higher the number of parameters, the higher the computational cost required to run the model. This can be confirmed by addressing different aspects of the computational cost, which was investigated in regards to memory occupation in [143] as well as computational time or floating-point operations per second (FLOPS) in [142] and [144]. Another common way to compare two algorithms in terms of efficiency is using the big O notation, also known as asymptotic notation, which classifies the algorithm based on its behaviour as the number of variables and input data increases towards infinity. Big O notation was investigated and considered as a point of model comparison in [21].

Finding the right balance between model complexity and accuracy is one of the many challenges addressed and discussed within most of the publications included in this survey. As an example, the performance similarity of the GRU and LSTM for solving speech recognition problems [138] suggests that performance similarities would also result in SOC estimation despite the obvious application differences. This assumption was initially confirmed in [141] where a GRU had been applied to perform SOC estimation using the same dataset [139] already used by the LSTM in [137]. In [145], a GRU was applied to estimate the SOC of an NMC and

LFP at seven different temperatures, ranging from 0⁰C to 50⁰C. Only the FUDS, DST, and CC drive cycles were used to generate the dataset.

A combination of vector autoregressive moving average (VARMA) and an LSTM was introduced in [146] to forecast li-ion battery voltage and SOC of an electric motorcycle where a different combination of inputs, including motor speed, input power and torque, and battery voltage, current, and temperature were evaluated. The authors have tested the model at 0⁰C and 25⁰C using only CVS-40, a South Korean driving cycle, and the data used to train the model were obtained directly from driving the motorcycle. No information about the battery, besides it being Li-ion, or the structure of the LSTM was provided, and it was not clear if the use of the VARMA in combination with the LSTM is essential when a larger dataset is available. The exploration of other features, besides the ones directly obtained from the battery, is an exciting path to pursue, for example, integrating weather forecast and/or vehicle destination.

In [23], the authors have introduced a novel way to reduce training time and further improve SOC estimation by using an LSTM with Transfer learning, and in [147] the authors explored the accuracy impact of using different types of loss function optimizers during model training, e.g. Adam, NAdam, Adadelta, AdaGrad, RMSProp, and AdaMax. Transfer learning and the use of appropriate optimizers are anticipated to be promising research paths that should be explored and combined with other methods.

3.2.5.3. Other RNNs applied to SOC estimation

Some publications focus on recurrent networks that do not use the gated approaches introduced in the prior section. In [148], the authors developed a dynamically driven recurrent network (DDRN) based on a nonlinear autoregressive with exogenous input (NARX) neural network architecture. The DDRN is used to estimate the SOC and SOH of two Li-ion chemistry batteries, LFP and LTO. What makes this supervised ML different from an FNN is the use of a recurrent input captured from the output of a previous state, e.g. SOC at instant k-1. This gives the DDRN an associative memory feature, despite being limited compared to the gated RNN previously discussed, this approach reduces the amount of data necessary to train the model.
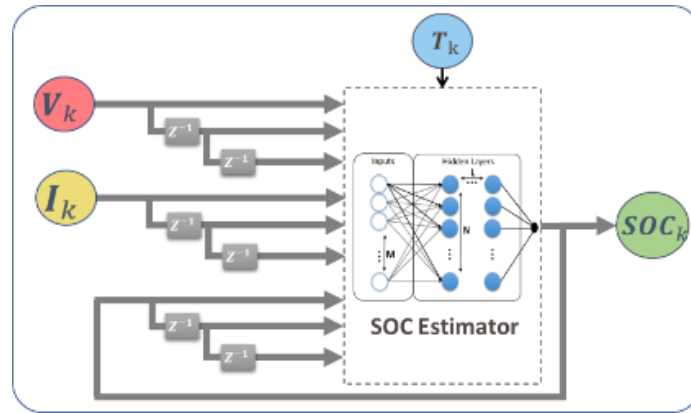
Figure 3.11. SOC estimator using DDRN, where the terminal voltage V_k, load current I_k and ambient temperature T_k are the inputs obtained by sensors and the recurrent inputs were $V_{(k-1)}$, $V_{(k-2)}$, $I_{(k-1)}$, $I_{(k-2)}$, $SOC_{(k-1)}$, and $SOC_{(k-2)}$ are the inputs from time steps $k-1$ and $k-2$

The authors also showed that for SOC estimation of the LFP battery, the training time was reduced by 1000 fold compared to a "non-recurrent" neural network. The input dataset, containing the voltage V_k, current I_k , ambient temperature T_k, and

SOC_{k-1} from the previous timestep were used to train and test the DDRN, and the data was obtained experimentally for the two batteries. The inputs and output organization on the DDRN for SOC estimation are shown in **Figure 3.11**. The DDRN was tested at temperatures of 0°C, 10°C, 25°C, and 40°C. Even though the cycling profiles used to obtain the battery data were dynamic, they resulted in a monotonic SOC output profile because there were no regenerative braking charging pulses during the cycle. This type of profile may not be a good representation of the xEV application domain. Therefore, the effectiveness of this approach needs to be further investigated

In [144], another NARX-based neural network was presented to estimate the battery SOC. A process to systematically alter the NN structure using an offline optimization algorithm, known as lighting search algorithm (LSA), was used to find the optimal combination of the number of neurons, input delay, and feedback delay to improve the accuracy of the model. The model was trained and tested using the dataset acquired at 0°C, 10°C and, 45°C from an NMC battery cell on two drive cycles, FUDS and US06. The work also showed a comparison with other SOC estimation methods also optimized by the LSA, but the NARX was shown to provide better accuracy. Although the use of optimization algorithms like LSA and BSA can help automate and alleviate the process of searching and building the optimal NN structure, it is essential to understand that a significant number of other tuning parameters, e.g. minibatch size, loss function optimizer, and the random

initialization of weights and biases can have a substantial impact on the results and are often neglected.

3.2.6. *Example methodology and guidelines for comparing soc estimation algorithms*

To provide a fair comparison of SOC or SOH estimation methods, such as those referenced in this review chapter, it is necessary to evaluate each algorithm with similar data, a similar number of trainable parameters, and a consistent training and testing methodology. When comparing methods, the following three guidelines are therefore recommended:

1- *Use the same training, validation, and testing datasets*

2- *Match the number of learnable parameters between models*

3- *Train the model several times*

Regarding the first guideline, **Table 3.4** provides references to high quality publicly available datasets that can be downloaded and used to build ML models for SOC and SOH estimation, allowing different authors, for example, to compare their results to others using the same datasets. The second guideline, to use the same number of learnable parameters, is to ensure compared models have similar computational cost and memory usage [110]. The third recommendation, to train the model several times, is necessary due to the degree of randomness embedded in the training process of ML algorithms, which can lead to several local minima. The number of repetitive training needed is highly dependent on the complexity of the

model, i.e., the more parameters, hidden layers and connections, the higher the chance it can find a local minimum.

To further contribute and to support the above guidelines, an FNN and LSTM were each trained 50 times using six of the nine drive cycles from the dataset [139] and tested using the remaining three drive cycles and the constant current (CC) charge profiles, e.g. UDDS-CC-LA92-CC-NN cycles. The training and testing data used includes each drive cycle at four ambient temperatures (-10⁰C, 0⁰C, 10⁰C, and 25⁰C), forming a larger dataset composed of 24 training and 12 testing drive cycles. This resulted in 2/3 of the data being used for training and 1/3 for testing, which is similar to ratios of training to testing data, which are often recommended.

The FNN structure is similar to the one used in [21] and has two hidden layers, with 55 neurons in each. The input vector Ψ is composed of the battery terminal voltage, current, battery temperature, average voltage, and average current, $\Psi = \{V, I, T, V\_avg, I\_avg\}$, as shown in **Figure 3.12(a)**. The RELU activation function was chosen for the FNN structure, and the voltage and current are averaged over the previous 500 time steps. The LSTM structure, shown **Figure 3.12(b)**, is similar to the one used in [147] and has 27 hidden units and an input vector composed by voltage, current and temperature, $\Psi = \{V, I, T\}$. The input vector for both the FNN and LSTM was rescaled to have values between 0 and 1 before being used to train the models. The total number of parameters for the FNN is 3466, and the LSTM is 3376.

74
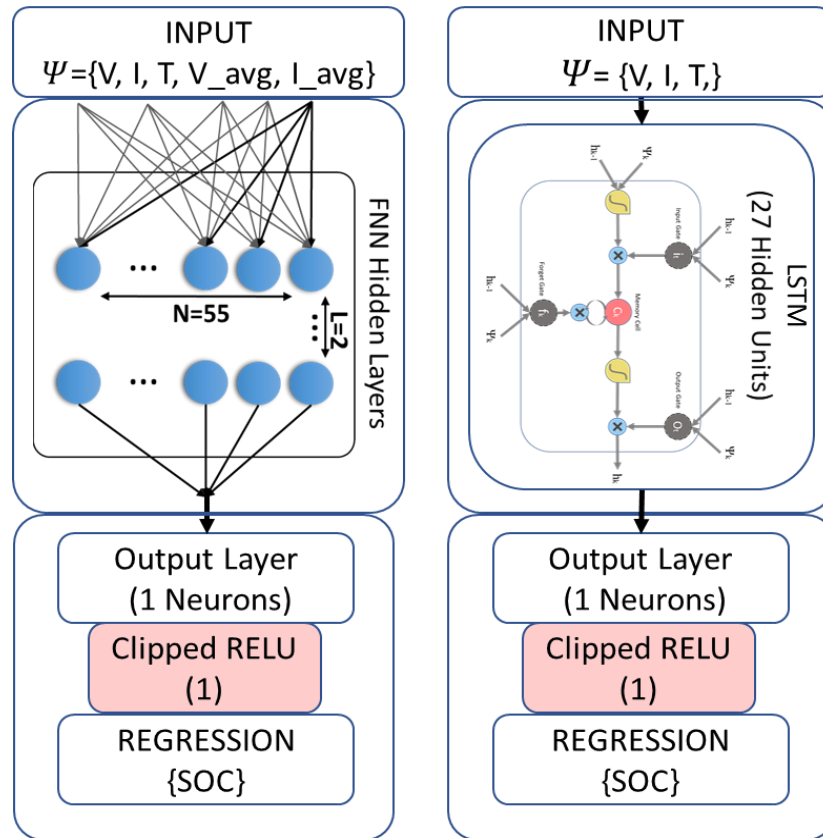
Figure 3.12. (a) FNN SOC estimator structure comprised of input vector Ψ, 55 hidden units per hidden layer, two hidden layers, and 3466 learnable parameters. (b) LSTM SOC estimator structure comprised of input vector Ψ, 27 hidden units, and 3346 learnable parameters

The FNN and LSTM were each trained fifty times for 3000 epochs, using the hyperparameters in **Table 3.1**. Because different initial parameter values were used each time the training was performed, a different result is achieved each time. To demonstrate this, the mean average SOC estimation error over all the testing data (three drive cycles and two charges at four different temperatures) was calculated, and a histogram of the results is shown in **Figure 3.13**. The error is shown to vary from 1.2 to 1.55% for the LSTM and from 1.5 to 3.5% for the FNN. Therefore, it is recommended to train multiple times when comparing different SOC estimation

structures; otherwise, it may be incorrectly concluded that one is superior to another.

TABLE 3.1 Training hyperparameters

Number of epochs	3000
Initial learning rate	0.01
Learning rate drop period	2500
Learning rate drop factor	50%
Loss function optimizer	ADAM
Number of Minibatches	89
Software platform	Matlab 2019b
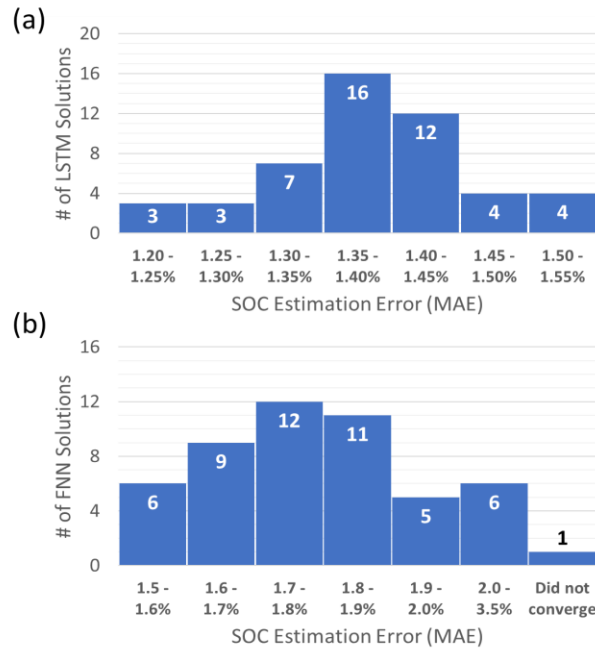
Figure 3.13. MAE histogram for 50 training iterations of SOC estimation algorithms; (a) LSTM (b) FNN

3.2.7. Comparison of SOC methods

The SOC estimation error for some of the methods presented in this section is summarized in **Table 3.2**, along with the data profiles used to train and test the

methods, the network inputs and outputs, a qualitative ranking of the dataset quality, the battery type(s) used, and the temperatures investigated. Most of the studies utilize similar inputs (voltage, current, and temperature), while a few utilize averaged values or other calculated values. About half of the studies use automotive type drive cycles and/or varying temperatures, with the remainder using constant or pulsed current cycles and/or fixed temperature. The studies with simpler data sets, such as fixed temperature and constant current, are given a dataset quality rating of * and the more sophisticated datasets are ranked as high as *****. In general, the higher the data quality, the more the stated accuracy for the method can be trusted.

Because it is difficult to come to any conclusions about the various methods by just observing the table, the accuracy of the methods is plotted in **Figure 3.14**. The RBFs are shown to have the highest error, an average of 2.2%, with the FNNs, RNNs, and other methods having an average error of 0.7%, 0.5%, and 0.4%, respectively. The FNNs and RNNs also have more challenging multitemperature datasets with automotive drive cycles, showing that they are the most promising methods and that the other methods (ELM w/ AUKF and SVM) should be investigated with more challenging cycles to determine their potential. While these results do show some interesting trends, it is essential to consider that many factors, as discussed in the prior section, affect the results for each method.

Table 3.2 Comparison of SOC estimation methods

ML Method	Lowest Error (only at 25^{0}C)	Data Profiles	Inputs(ψ) / Output (o)	Dataset Quality	Battery	Multi-Temperature
FNN[19]	0.33%(RMSE)@WLTC 0.27%(MAE) @WLTC	FTP75, NEDC, US06, GUDC, Highway, WLTC	$\psi = [V_{li(k)}, I_{li(k)}, T_{li(k)}, V'_{li(k)}, I'_{li(k)}, \sum I_{li(k)}, V_{la(k)}, I_{la(k)}, T_{la(k)}, V'_{la(k)}, I'_{la(k)}, \sum I_{la(k)}];$ o $= [SOC_{li(k)}; SOC_{la(k)}]$	***	LFP (12V, 8Ah)	No
FNN[21]	0.84%[++][+](MAE)@ US06 0.61% (MAE)@ HWFET	HWFET and US06	$\psi = [V_{(k)}, T_{(k)}, V_{avg(k)}, I_{avg(k)}];$ o $= [SOC_{(k)}]$	*****	[139]Li-ion Panasonic NCR18650PF	-20°C, -10°C, 0°C, 10°C, and 25°C
FNN w/ UKF[113]	1.4%(RMSE)@FUDS 2.5%(RMSE)@US06	FUDS, US06, DST	$\psi = [V_{(k)}, ..., V_{(k-4\tau)}, I_{(k)}, ..., I_{(k-4\tau)}, T_{(k)}, ..., T_{(k-4\tau)}];$ o $= [SOC_{(k)}]$	****	LFP (2.3Ah max)	0°C, 10°C, 20°C, 25°C, 40°C, and 50°C
FNN w/ECM[112]	0.33% (MAE)@FUDS	FUDS, DST	$\psi = [OCV_{(k)}];$ o $= [SOC_{(k)}]$	**	LFP (24V, 20Ah)	No
FNN w/ BSA[118]	0.81%(RMSE)@DST 0.91%(RMSE)@FUDS	FUDS, DST	$\psi = [V_{avg(k)}, I_{avg(k)}, T_{avg(k)}];$ o $= [SOC_{(k)}]$	***	NMC (3.6V, 2Ah)	0°C, 25°C, and 45°C
RBF w/ EKF[120]	~3% (RMSE)@CCC[+]	Constant current charging (CCC)	$\psi = [V_{(k-1)}, I_{(k)}, SOC_{(k)}];$ o $= [V_{(k)}]$	*	Li-ion (1.2Ah)	No
RBF w/ H∞[122]	0.7%(RMSE) @CCC[+]	Constant current charging (CCC)	$\psi = [V_{(k-1)}, I_{(k)}, SOC_{(k)}];$ o $= [V_{(k)}]$	*	Li-ion (1.2Ah)	No
RBF w/ UKF[123]	~3% (RMSE)@CCC[+]	Constant current charging (CCC)	$\psi = [V_{(k-1)}, I_{(k)}, SOC_{(k)}];$ o $= [V_{(k)}]$	*	Li-ion (1.2Ah)	No

RBF w/ RSMO [124]	2.32%(RMSE)@UDDS [+] 2.33%(RMSE)@HWY [+]	UDDS, Highway	$\psi = [\hat{x}_1, \hat{x}_2, \hat{x}_3, \hat{x}_4]$; $o = [\hat{\bar{\psi}}]$	**	Lithium-polymer, Turnigy (3.7V, 0.5Ah)	No
RBF w/ AEKF [126]	<2%(MAE)@DST [+]	DST, HPPC	$\psi = [C^j_{rate}, SOC^j, \Delta Q^j]$ $o = [\delta^j]$	*	Lithium-polymer (3.7V, 32Ah)	No
RNN [137]	0.57%(MAE)@ [++++]	HWFET, UDDS, LA92, and US06	$\psi = [V_{(k)}, I_{(k)}, T_{(k)}]$; $o = [SOC_{(k)}]$	****	[139] Li-ion Panasonic NCR18650PF (3.6V, 2.9Ah)	0 ℃, 10 ℃, and 25℃
RNN [141]	0.32%(MAE)@LA92 0.86%(MAE)@ BJDST	Panasonic: HWFET, UDDS, LA92, and US06 Samsung: FUDS, US06, BJDST	$\psi = [V_{(k)}, I_{(k)}, T_{(k)}]$; $o = [SOC_{(k)}]$	*****	[139] Li-ion Panasonic NCR18650PF Li-ion Samsung 18650-20R	0℃, 10℃, 25℃, and 40 ℃ (Panasonic) 0 ℃, 25 ℃, and 45℃ (Samsung)
RNN [145]	NMC: 0.77%(MAE)@ [+] LFP: 1.72%(MAE)@ [+]	DST	$\psi = [V_{(k)}, I_{(k)}, T_{(k)}]$; $o = [SOC_{(k)}]$	**	BAK B18650CD A123 18650 (LFP)	0℃, 25℃, 20℃, 30℃, 40℃, 50℃
RNN[148]	LFP :0.53%(RMSE) @[++] LTO :0.70%(RMSE) @[++]	Dynamic char./discharge profile[++]	$\psi = [V_{(k)}, I_{(k)}]$; $o = [SOC_{(k)}]$	**	LFP (3.6V) LTO(2.6V)	0℃, 10℃, 25℃, and 40℃
ELM w/ AUKF[128]	0.4%(RMSE)@ [++]	Constant pulse discharging current[++]	$\psi = [V_{(k-1)}, I_{(k)}, SOC_{(k)}]$; $o = [V_{(k)}]$	**	Samsung 2.6Ah	No
SVM[130]	0.4%(RMSE)@DST	DST	$\psi = [V_{(k)}, I_{(k)}, T_{(k)}]$; $o = [SOC_{(k)}]$	*	LFP (3.6V, 60Ah)	No

[+]assumed as "room temperature" in the paper
[++] **data acquired using a non-automotive dynamic charging/discharging profile**
[+++] **in the original paper, a typo shows the error as 0.084%.**
[++++]**at 10⁰C**
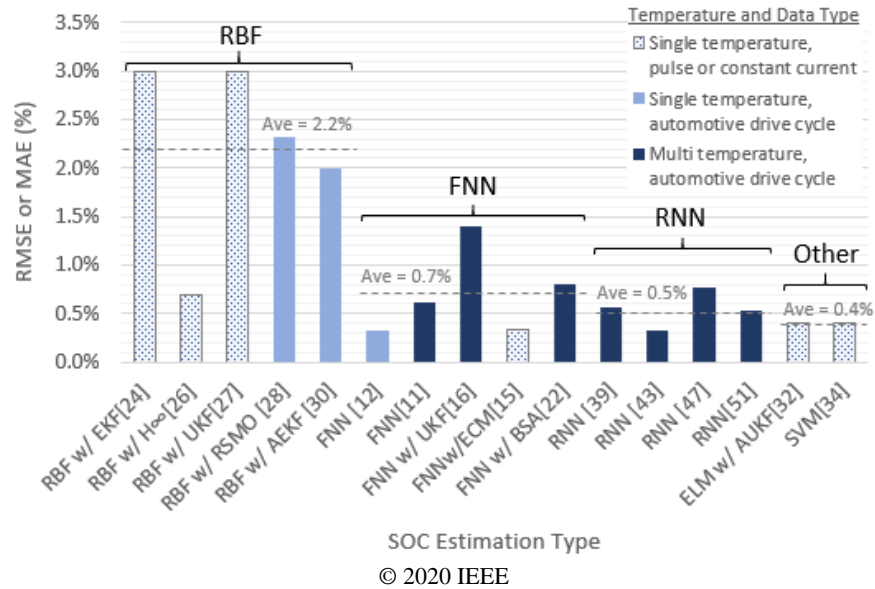
Figure 3.14. SOC estimation error, classified by method and data types.

3.3. Battery state of health estimation

Battery SOH is a measurement of battery deterioration in comparison to a new battery. This information is valuable for the vehicle energy management system to adjust its controls to keep the vehicle performance and safety within the desired boundaries. There are several ways to estimate and quantify the SOH of an xEV battery; many of the recent studies have considered either the loss of capacity (SOHc) or increase of internal resistance (SOHr). The conventional machine learning methods presented in this section for SOH estimation are grouped as the following types.

   3.2.1 Feedforward deep neural network (FNN)

   3.2.2 Recurrent neural network (RNN)

   3.2.3 Radial basis function (RBF) neural network

   3.2.4 Hamming networks (HNN)

3.2.5 Support vector machine (SVM)

3.2.6 Bayesian network (BN)

3.3.1. Feedforward neural network

As previously introduced in sections 3.1.1, an FNN performs non-linear mappings with an arbitrary number of inputs and outputs. For a more detailed explanation about the methods and its basic math, interested readers are referred to [110],[111].

For SOHc estimation, the battery capacity fading metric is typically represented by

$$SOH = \frac{C_t}{C_0} \times 100 (\%)$$

(3.19)

where C_t is the capacity estimate at time t and C_o is the new battery's nominal capacity. Battery capacity is typically measured via a particular test that spans the entire SOC range using high accuracy current measurements. However, this is rarely achieved in real-world usage of an xEV, so online estimation algorithms need to be employed.

In [149], the authors developed a real-time SOHc estimation method using an FNN based on the historical distribution of measured data over one year of tests of 18650 form factor cells. The method proposed in this work used data extracted from 10 different drive cycle profiles. In total, 44 datasets were created, eleven for each of the following temperatures: 10 ºC, 25 ºC, 45 ºC, and 60ºC. The historical distributions were based on 3D point clouds of battery current, voltage, and temperature. The relation between these three varies according to factors such as

battery SOC and age. The patterns of the point clouds change as the battery ages and capacity changes. A key feature extraction idea of the paper is that rather than grouping data points based on voxel segments of the axes (current, voltage, and temperature), a k-means algorithm was employed to find more optimal sub-region volumes. This reduced the amount of FNN pattern classification necessary to estimate the SOHc. The optimal number of sub-regions determined in this work was 80. A histogram of counts in each sub-region served as inputs to the FNN. The FNN structure was composed of 80 inputs, a hidden layer of 80 neurons, and a single output (SOHc). **Figure 3.15** shows an overview of the proposed approach. The FNN method was compared to two different SVM approaches. The first SVM used the same 3D inputs as the FNN, the other a combination of two 2D signals, e.g. current-temperature and voltage-temperature. The FNN was shown to have superior results. Practical challenges for the use of this method include lack of adaptability to adjust to cell-to-cell variations within a pack and the need to record and update the point cloud histogram distributions over the life of the battery pack.
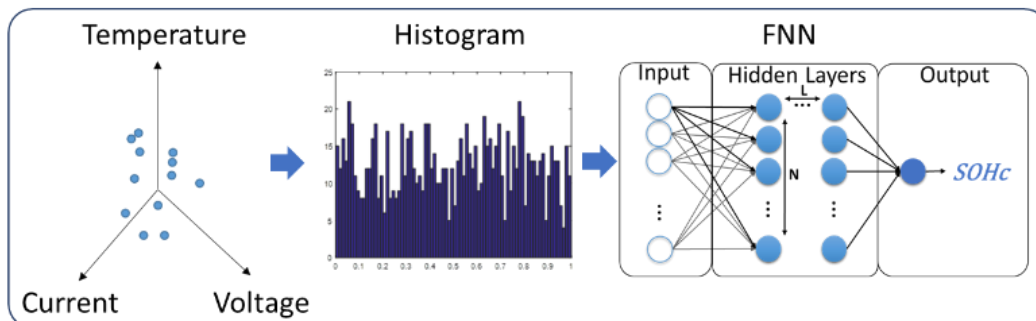
Figure 3.15. Point cloud distribution based SOH FNN [149]

A so-called structured neural network (SNN) was developed in [150] to compute SOH by estimation of internal parameters of a battery equivalent circuit model. The SNN is a variant of an FNN whose structure is guided by any existing battery model structure and knowledge. Compared to internal NN neurons, ECM parameters have a closer relation to the physical characteristics of the battery; for instance, the battery internal resistance variation over time can be correlated to the battery SOHr. Feature inputs to the SNN included SOC and its quadratic, cubic, and quartic powers. This enabled the usage of fourth-order polynomials in the SNN structure design. The overall SNN schematic is depicted in **Figure 3.15**. In principle, training an SNN is expected to be easier since the global minimum is expected to be easier to find by choosing initial NN weight seed values based on model parameters rather than purely random values.

The data used to train the SNN was collected directly from a vehicle, a Mercedes Benz S400 Hybrid. The data collection started from a new vehicle, 0km, at the BOL up to 174000km at the EOL. Each dataset recorded had a length of about 5 hours, and a total of 33 datasets were collected. Part of the data, 70%, was used to train the SNN, and the rest was used to validate the model. EIS was used to validate the internal resistance estimated by the SNN. The work compared an SNN with an Extended Kalman Filter approach that showed similar results. However, the SNN presented advantages in terms of computational speed and memory usage.
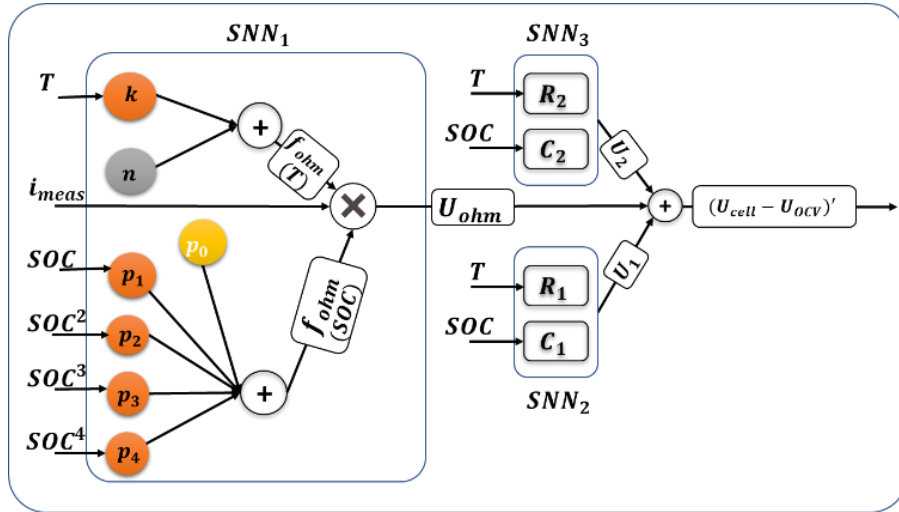
Figure 3.16. SNN schematic for internal resistance determination [150]

In [151], the authors used an FNN with time-delayed input data to estimate SOHc. It was referred to as an input time-delayed neural network (ITDNN). The usage of time-delayed inputs allows the NN better to model the dynamics and memory effects of a battery. The data used to estimate SOHc were based on the battery terminal voltage, current, time-delayed signals, and ambient temperature. An optimal time-delay of 20 seconds was determined for the voltage and current signals and shows the SOHc estimator structure. **Figure 3.17** shows the SOHc estimator structure where the FNN used was composed of 4 layers: 1 input layer, two hidden layers (L=2), and one output layer. The hidden layers were formed of three and two neurons (N_1=3 and N_2=2), respectively, with each layer including a sigmoid activation function.

The dataset used to train and validate the model was divided into five milestones measured in hours: 0 hours (BOL), SOHc=100%), 352 hours, 544 hours, 650 hours, and 650 hours (EOL, SOHc=10%). Each dataset was generated at three

separate ambient temperatures: 10°C, 25°C, and 40°C with currents of 6 A, 10 A, and 20 A. The battery used in this work was an LFP 20 Ah cell. A backpropagation algorithm was used to train the ITDNN.
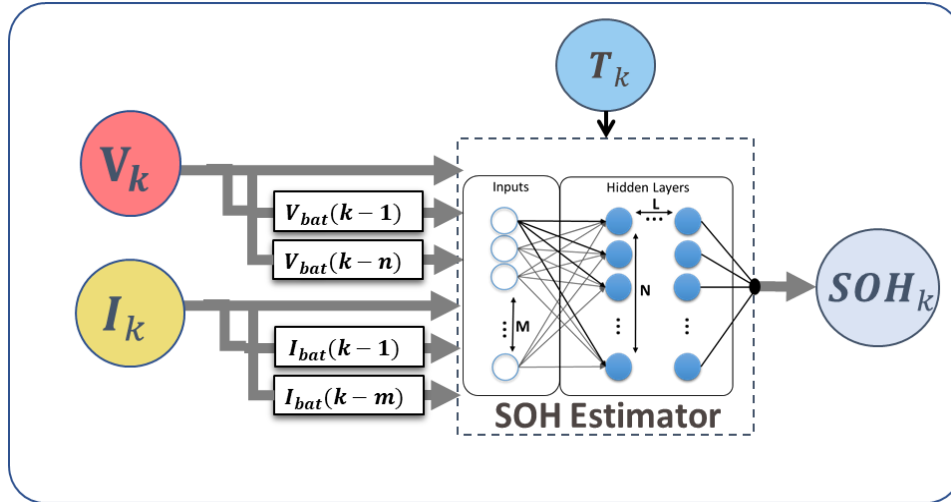
Figure 3.17. SOH estimator using ITDNN [151]

The work presented in [152] used a similar approach of FNN with input time-delays employing a single hidden layer with ten neurons. Moreover, multiple time-delayed input signals were considered, and practical considerations such as the effect of capacity estimation error on SOC estimation was studied.

The authors in [153] have established that the geometric variation of the battery terminal voltage can be correlated to the battery SOHr. They showed that the terminal voltage slope of a battery reduces as its SOH decreases and its internal resistance increases. Therefore, a differential geometry-based approach using samples of the battery terminal voltage and its velocity, defined here as the voltage slope variation over time, were used as inputs to train and validate a neural network

capable of correlating these inputs to the battery SOHr. Data sets, containing data from cells at different ageing states, were used to train the neural network model. Another dataset from an LFP was used to validate the approach for other cell types. Results showed that the method could estimate the battery SOH with accuracy around 1% Mean Absolute Error.

3.3.2. Recurrent neural network

SOH estimation involves tracking a slow battery ageing process from battery signals that exhibit dynamic states and memory. As a result, employing a recurrent neural network that contains internal memory is a natural approach to tackle SOH estimation.

A simple approach was presented in [148], where the authors built a dynamically driven recurrent network to estimate both the SOC and SOH of two Li-ion batteries. The RNN SOC estimation portion was described in the previous section. The SOHc estimate is fed back as delayed recurrent inputs; this gives the DDRN an associative memory feature, which is responsible for reducing the amount of data necessary to encode the dynamics in the network parameters. Other inputs to the RNN, include voltage, current, temperature, and time-delayed voltage and current. **Figure 3.18** shows the DDRN structure for SOH estimation. The battery life in this work was measured for several cycles versus terminal voltage. Each cycle was acquired after placing the battery in a climate chamber at 60ºC for a week to accelerate ageing, and then the batteries were charged and

discharged at 25ºC ambient temperature with the terminal voltage measured and recorded every second during the discharge.

The training dataset consisted of four milestones: 100 cycles, 200 cycles, 1600 cycles, and 1800 cycles, where the 100 cycles milestone was deemed battery beginning of life and 1800 cycles as the end of life. The validation dataset employed seven milestones, and it was divided as follows 300, 500, 700, 800, 1000, 1200, and 1400 cycles. The structure of the DDRN was composed of an input, a single hidden layer (L=1) and a single output. The hidden layer had 15 neurons (N=15) with a sigmoid function as its activation function. The authors developed their discharge and charge power profiles for this work but they may not be a good representation of the xEV application domain. Therefore, the effectiveness of this approach needs to be further investigated. As the SOC and SOH estimators were independently trained using the same input vector but with different objective functions, no integration between SOC and SOH estimations were explored. With a larger and more dynamic dataset, there may be some benefits to integrating SOC and SOH estimation, and this is recommended as an area of future work.
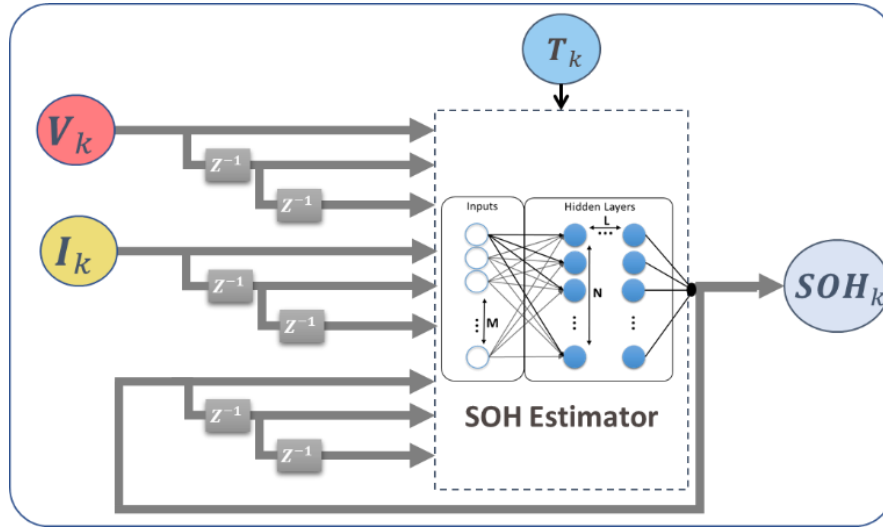
Figure 3.18. SOH estimator using DDRN [148]**, where the terminal voltage V_k, load current I_k and ambient temperature T_k are the inputs obtained by sensors, the delayed inputs were V_{k-1}, V_{k-2}, I_{k-1}, I_{k-2}, and recurrent inputs SOH_{k-1}, and SOH_{k-2}**

In [154], the authors created a novel approach to estimate the SOH based on a series of sequential snapshots of the battery current and voltage over time. This new approach aims to surpass the problems of the historical distribution discussed in the authors' previous work using an FNN approach [149]. The snapshot-based method takes into consideration the values of the battery current and terminal voltage within a window segment, with a fixed horizon width that shifts along with time. Moreover, this sliding window calculation happens only during charging, as it is a more stable and predictable condition than discharging. The proposed method utilizes LSTM layers similar to those shown in **Figure 3.19**. The output of this LSTM block, shown in **Figure 3.19**, is a set of vectors whose elements correspond to rolling time windows at different points in time, e.g. the first corresponds to the first window segment, and the last is shifted to reach up to the most recent point in

time. A pooling block processes the output vectors of the LSTM blocks. Three different approaches for this block are possible; the first directly passes the most recent vector, the second averages all input vectors, the third is a bidirectional approach that performs an averaging of a kind of forward/reverse elementwise multiplication. This latter method aims to mitigate an often mentioned vanishing problem [155]. Finally, the pooling layer output is fed into a linear regression layer to estimate the SOHc.
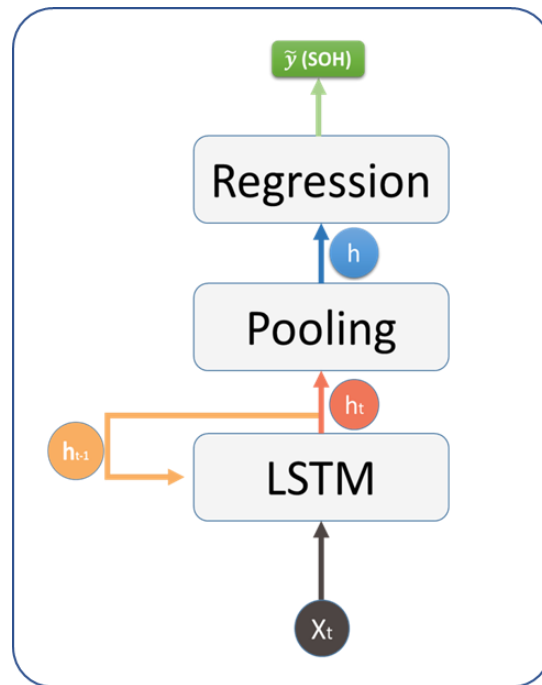
© 2020 IEEE

Figure 3.19. SOHc estimation architecture based on snapshot approach employing LSTM and linear regression [153]

The neural network structure was trained using backpropagation to update the weights and bias in each layer, aiming to minimize the error between a SOHc reference value and the estimated SOHc. Two other variations of this method were presented, including a merge with the historical distribution method (FNN approach)

89

and the use of a BiLSTM. A dataset of 40 dynamic drive profiles tested at four different ambient temperatures (10, 25, 45, and 60°C) was employed. The batteries were aged via cycling until 70% of their original capacity remaining. The proposed framework was empirically verified, obtaining average error not higher than 0.0765 Ah on the testing dataset investigated at all temperatures.

In [156], the authors have also used an LSTM to estimate the battery SOHc where it was trained using a 2.3Ah LFP cell dataset, simulated from an electrochemical model of the cell at different SOH's. The data used to train the LSTM was based on the correlation of the cell capacity variation, voltage, current, and temperature. The dataset used to train the model was obtained by simulating an ageing procedure using the LFP electrochemical model, which includes submitting the model to high currents and temperature inputs. Then the SOHc was estimated only during charging profiles from the model simulated dataset. As ML can only be as good as the data used to train it, the dataset generated from a model should have a certain amount of error added to it, ensuring the estimation method has data representative of a real application. As an alternative to model-generated data, publicly available datasets can be used as well, as listed in **Table 3.4**. For example, a dataset from several Li-ion cells, provided by NASA Prognostics Center of Excellence [157], can be downloaded and used as the author did in a similar work [158].

The authors in [159] have developed and validated a model based on an LSTM to estimate both SOC and battery internal resistance (SOHr) simultaneously,

meaning that it has two outputs instead of only one. The internal resistance data was first obtained from an ECM model implemented for this purpose. The inputs to the LSTM based model are the current, temperature, voltage, and voltage variation, which is the voltage value calculated from its difference at time step t and $t-1$, or just $U_t = V_t - V_{t-1}$. The relevance of the voltage variation was tested and shown to be valuable to improve model accuracy. The authors did not mention much detail about the chemistry of the Li-ion cell used besides some of its characteristics, e.g., Nominal capacity 2Ah, 18650 formats, nominal voltage 3.6V. The dataset used to train and validate the approach was obtained from the Li-ion cell by cycling the battery with US06, DST, and FUDS profiles at 0ºC, 25ºC, and 45ºC. Only US06 and DST data were used to train the model, and FUDS was used to test. Although the method was shown to perform better in comparison to other ML models, a constraint regarding this approach is related to the accuracy of the internal resistance obtained from the ECM, as the LSTM can only be as accurate as of its objective function. Therefore another method, such as EIS, could be used to validate or determine the accuracy of the values generated by the ECM.

The authors in [160] have used EIS to determine and validate the parameters of an ECM capable of finding correlations with the Li-ion SOC, then developed an RNN to predict the SOH of the Li-ion battery based on both the battery capacity fade and increase of its equivalent series resistance. The criteria of the battery EOL in this work is either when the capacity decreases 20% or when its equivalent resistance increases 100%, based on the battery BOL values. Datasets were

experimentally obtained through months of tests by placing an NCA Li-ion cell under an accelerating ageing test protocol, which included a combination of ambient temperature varying from 40⁰C to 50⁰C, currents from 65A to 130A, and SOC from 20% to 40%. These datasets were finally used to train RNNs capable of estimating the battery capacity and equivalent resistance and combined to estimate SOH, as shown in **Figure 3.20**. The RNNs were trained and tested by using cell temperature, current, SOC variation, and the capacity and resistance of previous time steps. The SOH estimator model has shown an accurate prediction of the battery SOH when compared to the experimental data, obtaining less than 1% mean squared error (MSE) on both capacity and resistance estimations.
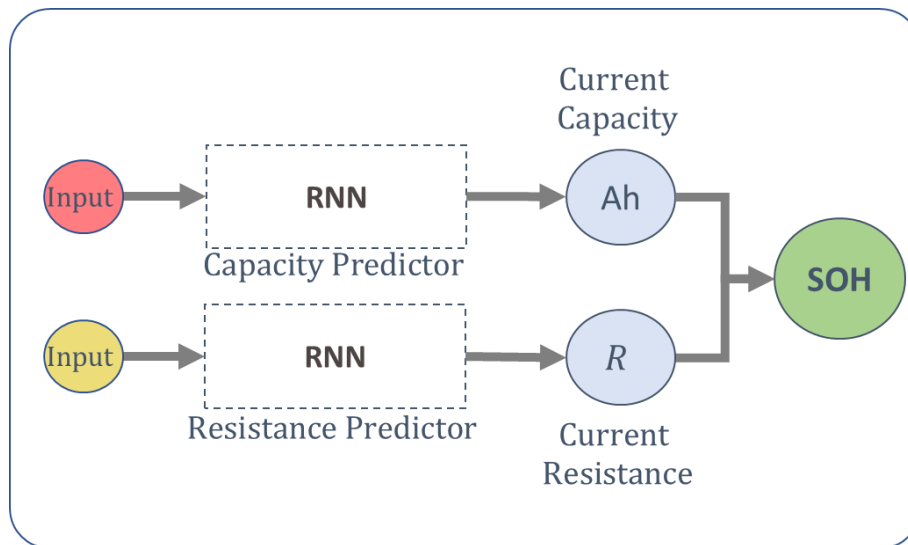
Figure 3.20. SOH estimation architecture based on battery capacity and resistance estimation using RNN [160]

3.3.3.   Radial basis functions

A sparse Bayesian predictive modelling (SBPM) algorithm can be used to identify the nonlinear relation of different features within a dataset. In [161], the authors

used an SBPM to determine the relationship between the battery capacity and voltage sequence sample entropy, where the SBPM employs the concept of radial basis functions in its design. An HPPC procedure was used for testing a set of battery cells. The sample entropy assesses the dependency of a given data point on values of previous points and is averaged over the entire time-series [162]. In this case, the sample entropy is used to identify the pattern of the battery terminal voltage over time. The proposed SBPM-based method procedure is shown in **Figure 3.21**.
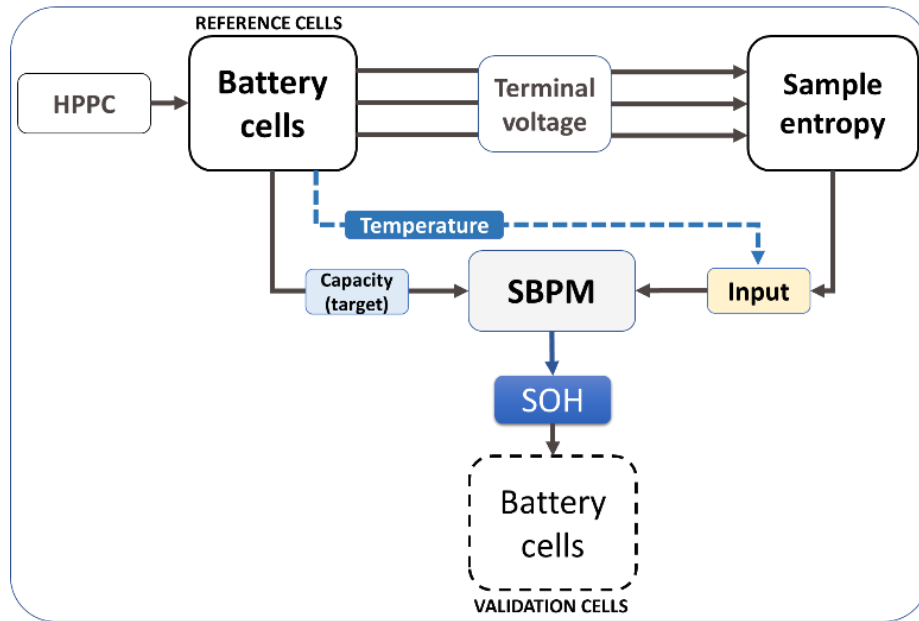
Figure 3.21. SBPM diagram to estimate the SOHc [161]

The SBPM was trained and tested using data collected from NMC Li-ion cells (Panasonic UR14650P) at ambient temperatures of $10°C$, $22°C$, and $35°C$. The SBPM was also compared to an SVM, which like the SBPM, also adopted a radial basis function to correlate the nonlinear relationship between the capacity loss and

the sample entropy. It was observed that as the sample entropy increases, the capacity decreases.

3.3.4. Hamming neural network

A Hamming neural network (HNN) contains both an FNN and an RNN, and an example is shown in **Figure 3.22**. The HNN has found extensive applications in pattern recognition, specifically binary pattern recognition. In [163], a Hamming Network was used in cooperation with a Dual Extended Kalman Filter (DEKF) to estimate SOC, capacity (SOHc) and resistance (SOHr). An equivalent circuit modelling approach was employed in the paper.
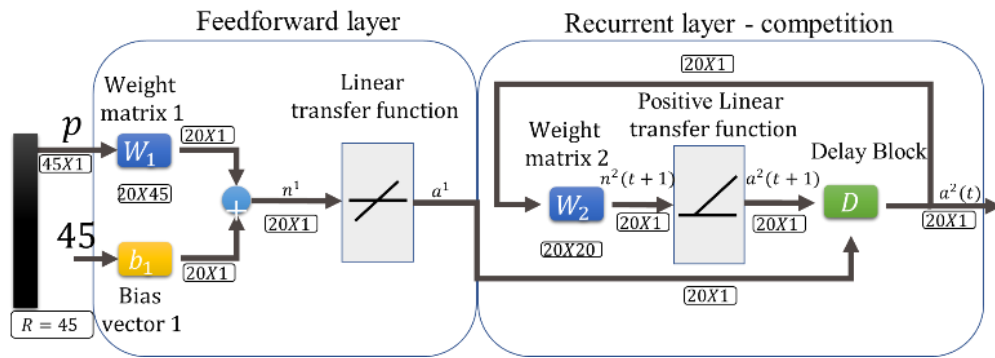
Figure 3.22 Hamming Neural Network [163]

The HNN was used to estimate the ECM parameters based on charge/discharge voltage patterns, capacity patterns, and how they change over time. The parameters estimated were fed to a DEKF to perform battery state/parameter estimation. The HNN used reference patterns experimentally extracted from 20 Samsung 18650 Li-ion batteries tested at an ambient temperature of 27⁰C.

The battery data patterns were classified into 15 different categories. To be suitable for use in the HNN, the data needed to be transformed into binary arrays with elements of -1 or 1. The feedforward layer computes the internal product with the input pattern data, and the recurrent layer is responsible for outputting the dominant response using the winner-take-all principle [43]. After the HNN determines which of the predetermined patterns is the closest to an arbitrarily selected battery, the corresponding ECM parameters are selected, e.g. resistance $R^{selected}$. Resistance based SOHr was calculated as

$$SOH_r = \left| \frac{R^{selected} - R^{aged}}{R^{fresh} - R^{aged}} \right| \tag{3.20}$$

Where $R^{selected}$ is the resistance of an arbitrarily selected battery determined by the HNN, R^{aged} is the resistance of an aged or EOL battery and R^{fresh} is the resistance of a new BOL battery.

Like many machine learning approaches, a significant part of the effort comes in the form of data acquisition and preparation before the data is ready to be used in the HNN. Moreover, the experimental results in this research were limited to a single temperature. Additional sophistication of the approach would be needed to handle an expanded temperature range and the resulting change in ECM parameters [27].

3.3.5. Support vector machine

The SVM was initially introduced in section II.D. for SOC estimation. This section will focus on methods using the SVM applied to xEV SOH estimation, including

the work presented by the authors in [164], which uses an SVM to estimate SOHc and SOHr. For [164], data were acquired from the vehicle battery-based on charge and discharge profiles at four different temperatures (0ºC, 10ºC, 30ºC, and 40ºC). The data was used to train and validate the SOH estimation method based on both battery capacity and internal resistance variation. The SVM was initially trained to estimate the battery voltage drop response during 10s discharge pulses to calculate the battery resistance variation (SOHr) and capacity variation (SOHc) during C/3 partial or full discharge profiles. The inputs for the SVM were the battery current, temperature and SOC. The SOH estimation accuracy provided by the SVM was calculated from the measured values to be 0.63% RMSE for SOHc and 6.2% RMSE for SOHr. Computational performance measurements were also provided, showing potential viability for onboard vehicular applications.

Another work using an SVM to estimate SOH was presented in [165]. In this case, the authors combined an ECM with a relevance vector machine (RVM) and particle filter (PF) to estimate the SOC, SOH, and remaining-useful-life (RUL) of Li-ion batteries. The RVM, a supervised learning machine used in this case for regression, was trained to adaptively change the ECM internal parameters as the battery ages or fault processes occur. The data used to train the RVM was obtained from cycle-life tested 18650 Li-ion cells. EIS and various sensors were utilized to acquire the battery data, including but not limited to voltage, current, and temperature. Once trained, the RVM combined with the PF could generate a probability distribution over time to anticipate operational conditions and predict

the SOH and RUL. Another work, presented in [166], proposed a new method combining the estimation of both SOC and SOH using an adaptive sigma point Kalman filter and an SVM. The work acknowledges the interdependence of SOC and SOH, which is likewise mentioned by many of the papers in this section. It is concluded that an accurate estimation of SOC or SOH can benefit the estimation of the other.

The authors in [167] have developed a model based on SVM, which is capable of learning and estimating SOHc online from battery voltage data acquired during charge, although only from a monotonic section of the data. The SVM strongly depends on finding the appropriate coefficient β; therefore, by adjusting the value of β as the battery ages, it is possible to adapt the SVM to update the SOHc properly. The initial value of β and the support vectors are determined using regression with the BOL battery data (voltage and battery capacity). During online operation, the coefficient β is updated using a least-squares algorithm. Segments of about 15 minutes in length are shown to be sufficient for the SVM to check for correlation within the data and to update the model parameters. This proposed approach is of interest because it avoids the need for online training, which is very computationally costly and hence avoided or merely impractical. The dataset was experimentally acquired from two NMC cells, where they were repeatedly cycled 60 times at 1C and 50ºC and discharged at 25ºC at 0.33C and 0.5C rates to measure capacity. This cycling sequence was repeated until the batteries reached 80% of their original capacity.

3.3.6. Bayesian network

A Bayesian network has the objective to find causation based on conditional dependencies by computing the probabilistic relationship between variables, and its dynamic version also considers the relationship at each sequential timestep. In [168], the authors have applied a Dynamic Bayesian Network (DBN) using only the observed battery terminal voltage to estimate the battery SOH. The DBN model was trained using data from Li-ion cells at different ageing states and constant current charging process with error not greater than 5%. Another similar work using a probabilistic distribution based on a Bayesian network (BN) was presented in [169]. The network uses the constant current time, voltage drop, and OCV after a CC/CV charge cycle and a rest period to estimate the SOH from the data extracted from 110 Li-ion batteries, where data from 100 were used to train and 10 to test the method. The accuracy obtained from the test was an average error of 0.28%.

3.3.7. Comparison of soh methods

Several characteristics of some of the techniques and research works presented in this section are summarized in **Table 3.3**, including the error for the SOHc, SOHr, or other SOH methods investigated, the battery type, and the temperatures considered.

Table 3.3 Comparison of SOH Methods

ML Method	Lowest Error (only at 25^{0}C)	SOH approach	Battery	Multi-Temperature consideration.
FNN w/ k-means[149]	SOHc: 0.66%(RMSE)	Based on capacity loss during charging	Li-ion 18650 3.1Ah	0℃, 10℃, 25℃, 45℃, and 60℃
RNN(LSTM)[154]	SOHc: 0.96%(RMSE) @ Validation R1 dataset	Based on capacity loss during charging	Li-ion 18650 3.1Ah	0℃, 10℃, 25℃, 45℃, and 60℃
DDRN[148]	SOHc: 0.1126Ah (RMSE) LFP@EOL SOHc: 0.34Ah (RMSE) LTO@EOL	Based capacity loss and number cycles	LFP (3.6V) LTO(2.6V)	25 ℃ and 60 ℃ (for accel. ageing)
FNN[153]	SOHr: 0.81% (MAE) LFP	Based on the internal resistance extracted from voltage variation	Li-ion IFP1865140	25℃
RNN[162]	SOHc: 0.46% (MSE) SOHr: 0.29%(MSE)	Based on Capacity and resistance estimation	NMC Li-ion (100Ah, Pouch))	40℃, and 50℃
SBPM[161]	SOHc: 1.38% (average relative capacity error)	Based capacity loss and sample entropy	NMC Li-ion Panasonic UR14650P (3.7V, 0.94Ah)	10℃, 22℃, and 35℃
FNN (SNN) w/ ECM[150]	0.32% (mean voltage deviation)@13,000km 0.28% % (mean voltage deviation)@80,000km	Based on ECM internal resistance estimation	Li-ion Saft VL6P (3.6V, 6.5 Ah)	23℃ up to 50℃ were considered
HNN w/ DEKF[163]	-	Based on ECM internal resistance estimation	Li-ion Samsung 18650(1.3 Ah)	No
SVM[164]	SOHc: 0.63%(RMSE) SOHr: 6.2% (RMSE)	Based on capacity and resistance variation	Li-ion Enerdel (17.5Ah, 2.5V, Pouch)	0℃ to 40℃
DBN[168]	SOHr: <5%(MAE)	Based on resistance	Li-Mn (3.7V, 6Ah)	25℃ and 55℃
BN[169]	SOHr: 0.28% (Avg Error) SOHr: 1.15% (Std Dev.)	Based on resistance	Li-Co (3.7V, 2.4Ah)	1℃ and 23℃

Almost all of the proposed methods can estimate capacity or resistance with 1% or less error, showing they are all promising candidates for SOH estimation. Two of the best methods are the FNN with k-means and RNN(LSTM) methods presented in [149] and in [154], which have low errors of 0.66% and 0.96% respectively despite the challenging multi-temperature dataset used to train and validate the networks.

It is challenging to draw more specific comparative conclusions about the methods, though, because of the differences between datasets, battery types, test conditions, and target criteria. As previously discussed in section II-F, ML models are data-driven algorithms and, therefore, the quality of the data used to train and validate is undoubtedly one of the essential aspects to be considered. Many of the works presented in this section have used datasets that are only good for preliminary studies, but insufficient to be used to compare methods intended to be applied to an xEV application. Therefore it is recommended that future ML SOH estimation works use publicly available datasets, as shown in **Table 3.4**, or share their datasets so others may benchmark their methods against the prior art. The dataset available in [170], for example, was obtained from 124 LFP cells acquired at fast-charging conditions at varying SOC ranges. The training guidelines suggested in section 3.1.6 can as well be applied to SOH estimation.

Table 3.4 Publicly Available Battery Datasets

Dataset Repository	Reference
Li-ion Panasonic NCR18650PF	[139]
Li-ion -NASA Ames Prognostics Data Repository	[157]
Li-ion LFP A123 (APR18650M1A)	[170]
Li-ion LG 18650HG2	[171]

3.4. Concluding remarks

Based on the studies presented and summarized in this work, a wide range of machine learning approaches are suitable for the estimation of battery SOC and SOH. Many of the studies presented in this review did not use data with sufficient realistic dynamics that usually occur in a real xEV application. For example, only three studies, including the contribution of this work in section 3.2.6, validated their method at negative ambient temperatures, where the estimation of SOC and SOH is even more challenging. Simplified comparisons were made among the different SOC and SOH estimation methods, providing some general insight with each work and showing that in general, SOC and SOH can be estimated with an error of around 1%.

The studies reviewed also highlight the importance and challenge of collecting and preparing the data used to train and validate the algorithms; this is a crucial and challenging task when using data-driven algorithms. The data collection process can require months or years of testing, especially when SOH estimation is the objective. Despite the increasing amount of data being generated and the recent advances in the ML, their use and efficiency are still limited by not only the quantity but also the quality of the data. The computational complexity required to train and

deploy ML-based models should be further investigated and compared in future work since it has not been addressed consistently within the surveyed work.

Many publications have used datasets that are good for preliminary studies but can be insufficient to compare methods intended for xEV application. Therefore, a table referencing publicly available datasets has been presented to facilitate the access to high-quality data and hence help improve further the quality of future works in the field. Additionally, the importance of the intrinsic random nature of the NN training process and the resultant variation of its accuracy was demonstrated by repeating the training of two different NNs fifty times. A simple set of guidelines is suggested to be followed when training and comparing ML algorithms, which considers the use of the same validation dataset, the number of ML fitted algorithm parameters and training process repetitions.

4. NON-RECURRENT DEEP NEURAL NETWORKS DESIGNED FOR STATE-OF-CHARGE ESTIMATION AT MULTIPLE TEMPERATURES

4.1. Introduction

This chapter focuses on the use of feedforward deep neural networks to estimate battery SOC. An FNN is investigated due to its simplicity and advances with this algorithm in areas outside the automotive industry [111]. Additionally, the FNN, compared to recurrent networks such as the LSTM, requires less computing power to train and may require fewer computations per time step of the operation. A simplified SOC FNN concept diagram is depicted in **Figure 4.1**, where I_k, V_k, and T_k are measured battery current, voltage, and temperature and SOC_k is the measured state of charge. Because the FNN has no internal memory, one of the drawbacks compared to the LSTM, for example, filters based on the moving average values of current and voltage are uses as inputs to effectively give the network an external memory. The NN structure includes multiple hidden layers and a variable number of neurons. Large datasets are needed to fit or train the NN learnable parameters, such as the neurons' weights and biases shown in **Figure 4.1**.
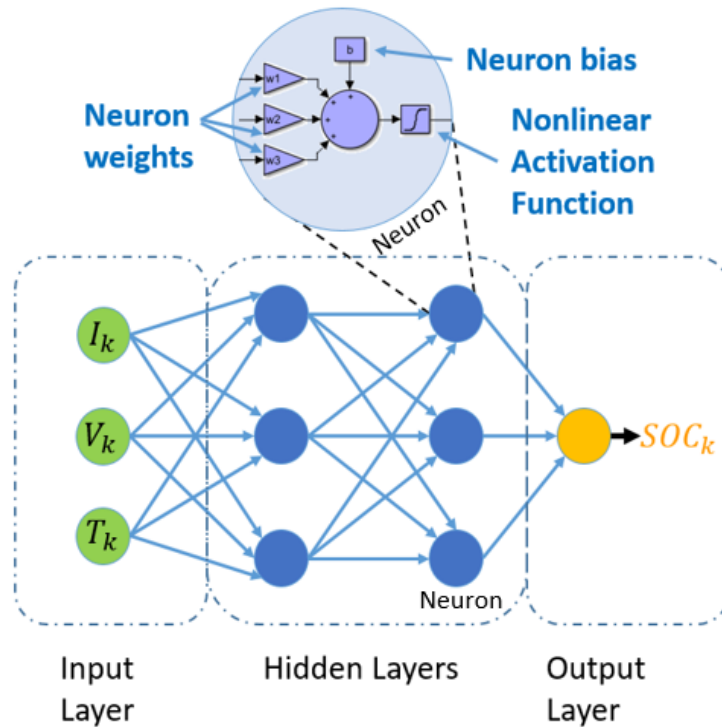
Figure 4.1 Simplified concept FNN structure for SOC estimation.

4.2. Feedforward neural Network training process

The concept of supervised machine learning is applied, where the FNN parameters are determined by minimizing an error cost objective function, e.g. the sum of squared SOC estimation errors. A flowchart of the FNN training process is shown in **Figure 4.2**, where a training dataset, often divided into batches or fractions, is fed into the FNN. So-called forward propagation computes an initial output and then compares to a reference SOC to compute a loss (sum or errors). The loss is backpropagated, using a series of partial derivatives concerning each of the FNN internal parameters (weights and biases) updating their values, then a new iteration repeats. This iterative process continues until pre-set criteria, such as reaching a target error or number of iterations, are met.

At regular intervals during the training iterations, a separate testing data set is used to validate the accuracy of the FNN. The model is tested with separate data to demonstrate that the trained model can perform well in conditions that are present in the application domain but not used in the training process. When the model performs well only for the training dataset, the FNN is said to have been overfitted to the data, i.e. the fitting is too specialized to the given training dataset. A more thorough explanation of the FNN training process can be found in [19].

4.3. Data acquisition and preparation

As an FNN is a data-driven method, the quality of the data can be inferred based on how much of the targeted domain information can be found within the dataset used to train the NN, as well as how much noise or irrelevant information it contains. Although it is essential to remark that despite being unwanted in the application, measurement noise and error in most cases cannot be removed and therefore, should be considered when training and testing a neural network. Consequently, the noise becomes part of the targeted domain information. Later in this chapter, this subject will be addressed in more detail and used to improve the robustness of the SOC estimator.
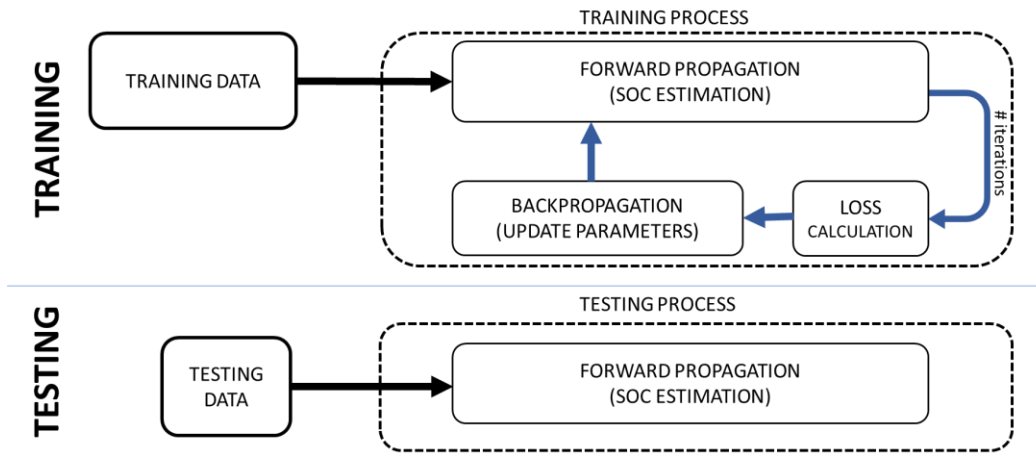
Figure 4.2 Neural network training and testing/validation overview process

Table 4.1 Battery datasets specifications [171]

BATTERY	*CAPACITY*	*FORMAT*	*PROFILES*	*TEMP.*
PANASONIC 18650PF (PANASONIC)	2.9 Ah	Cylindrical 18650	Mix (1-4), HW, UDDS, LA92, US06, NN, CC	-10ºC, 0ºC, 10ºC, 25ºC
LG HG2 (LG_HG2)	3 Ah	Cylindrical 18650	Mix (1-8), UDDS, LA92, HW, US06, CC	-10ºC, 0ºC, 10ºC, 25ºC

In the case of this work, the battery datasets acquired to train and validate the SOC estimator need to be representative of xEV applications, the targeted domain. The batteries were tested with a series of power profiles calculated for an electric vehicle, including the automotive industry-standard drive US06, LA92, UDDS, and HW cycles. To increase the amount of training and testing data available, eight additional drive-cycles were also created by combining time-shifted portions of the four drive cycles, referred to as "Mix 1-8". The four standard cycles and five of the mixed cycles were tested on the Panasonic cell, and the four standard cycles and all eight mixed cycles were tested on the LG HG2 cell, as shown in **Table 4.1**. Each drive cycle is repeated until the battery is fully discharged, and the battery is then

charged. The same charge method is always used, 1C constant-current, constant-voltage charging, which is commonly referred to as CC-CV charging. Each dataset contains the measured cell voltage, current, battery temperature, and the amp-hours consumed or supplied by the battery.

The equipment used to generate the power profiles and log the battery data are listed in **Table 4.2**, and the schematic of the lab test bench is shown in **Figure 4.3**.

<p align="center">Table 4.2 Test equipment specifications</p>

Cycler manufacturer	Digatron firing circuits
Test channel used	25A, 0-5 V *(Panasonic)* 75 A, 0–5 V *(LG_HG2)*
Voltage/current accuracy	±0.1% full scale
Data acquisition rate	1Hz
Thermal chamber	Cincinnati Sub-Zero *(Panasonic)* Envirotronics *(LG_HG2)*
Temperature sensor	Type K thermocouple *(Panasonic)* AD592 *(LG_HG2)*
Size	8 cu. Ft.
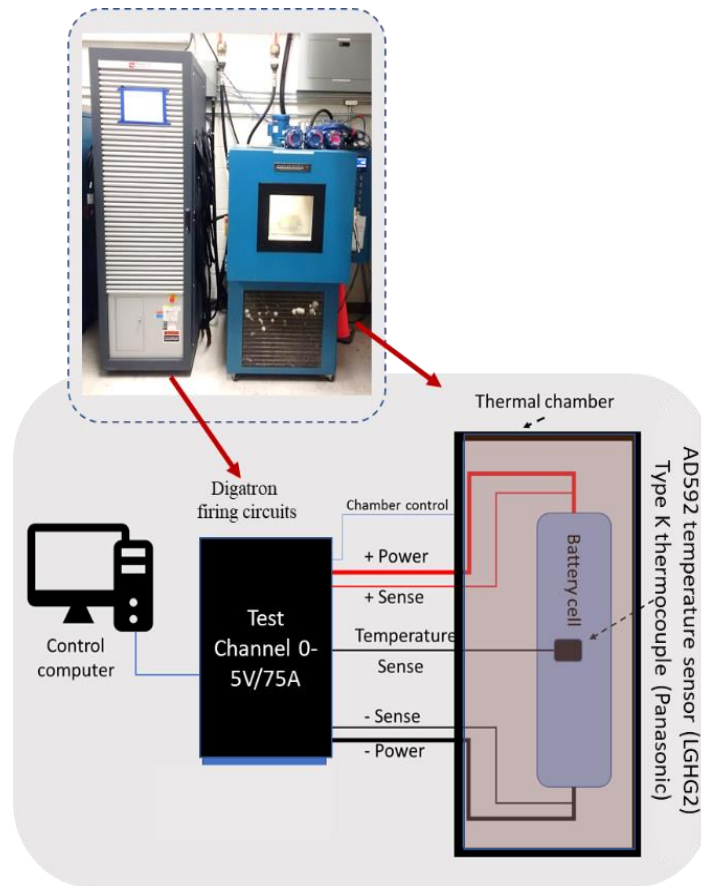
Figure 4.3 Schematic of the test bench and data logging system

Following battery testing and data logging, the battery data is split into two subsets, where 7 of 12 cycles (64%) of the available data was assigned for training and 4 of 11 cycles (36%) for testing in the case of the LG_HG2 cell; and 5 of 8 cycles (63%) and 3 of 8 cycles (37%) for respectively the training and testing for the Panasonic cell. Both datasets were arranged very similarly with consecutive charge and discharge cycles. For each battery, the training dataset is composed of all of the "Mix" drive cycles and associated charges and the test dataset by the UDDS, US06, and LA92 cycles with the associated charges. **Figure 4.4** shows the histogram of the voltage, current and battery temperature from training and testing datasets.
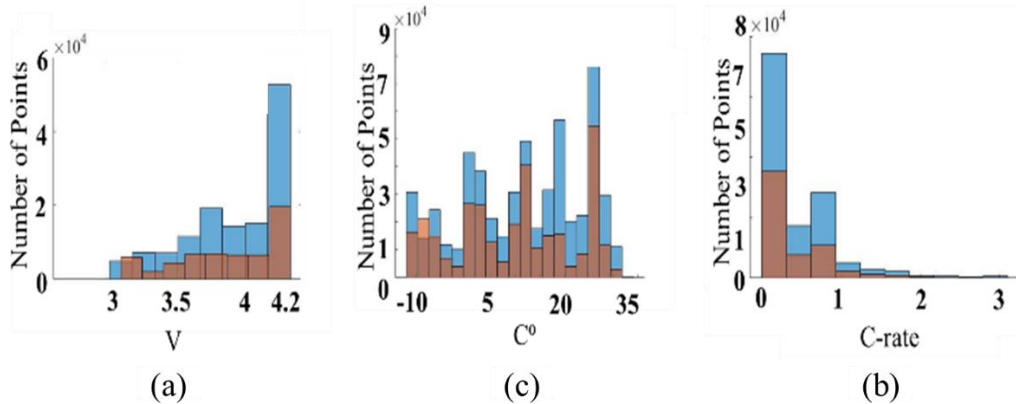
Figure 4.4 (a) Histogram of the battery voltage (V), (b) temperature (C⁰), and (c) current (C-rate) from training and testing datasets from the LG_HG2 cell

The FNN algorithm is used to predict SOC, which is calculated from the measured amp-hours discharged from the battery. The Ah is accurately obtained from the cycler presented in **Table 4.2**. The amp-hour measurement is reset to zero (100% SOC) after each full charge and is rescaled to SOC ranging from 0 to 1, where 0 is equivalent to 0% SOC and 1 to 100% SOC.

Normalizing the dataset before using it to train the model is another essential step of the data preparation. Normalization improves the model performance during the training process by reducing the distortion of scale among values in the training dataset. For example, instead of feeding the FNN with (15 A; 4.2 C; 35⁰C), respectively current, voltage and battery temperature, the values could be normalized to (1; 1; 1). Normalization, in practice, can significantly reduce the training time as the input values can be better compared, and the "learnable" parameters quickly adjust during training [21]. Another critical step is to use the correct data structure, especially if the dataset requires more memory than is available on the computer or graphics processing unit (GPU). For these large

datasets, it is necessary to use data repositories to manage the data and to feed the data appropriately during training. This also improves the training efficiency considerably as it can provide options like the use of multiple central processing units (CPU) cores and even multiple GPUs when available. Both Matlab and Tensor Flow provide such options. The list below shows a sequence summarizing the main steps taken to prepare the datasets in this work before use to train an NN to perform a SOC estimation.

1. Acquire or use data that is representative of the intended application.

2. Search the dataset to find possible inconsistencies and errors during experiments.

3. As this is a time-series problem certify that each data file was acquired using the same sample rate, if not is necessary to rescale and to match the data rate, e.g. if discharge data is acquired at 1Hz and charge data at 0.01Hz, charge data should be upsampled to 1Hz

4. Split the dataset into two completely distinct subsets (Training and Testing) to validate the model during and after the training process

5. Use normalization to improve the training process efficiency. Note: MATLAB provides the option of batch normalization on the input layer, check the documentation.

6. Use a data repository when the data is too large to fit in the available computer memory; it will also improve the efficiency of the training process. In the case of this work, as the data set is not very large, it could be easily trained in a CPU

with simple data arrays. To make the method more generalized, though, a datastore structure was used in all cases, e.g. 'datastore' function on Matlab or '*tensorflow_datasets*' when using Tensor Flow.

4.4. Robust Li-ion SOC estimation using FNN

Depending on the problem tackled, the choice of the type, shape, size and number of inputs of the FNN can vary widely. Building an FNN is an iterative process, and it is possible to prototype and check the initial results quickly and to use this information to perform structural changes and another iteration. In the case of SOC estimation for Li-ion batteries applied to xEVs, some assumptions and methods, based on the published literature [19][137][172] were applied, i.e. the use of voltage, current, and temperature are essential, but not always sufficient to estimate SOC with a reasonable 1% MAE. The choice of FNN in this article was mainly due to its simplicity and the assumption that it could run more efficiently in a BMS.

However, it is noted that some necessary adjustments could increase its overall complexity, such as increasing the number of inputs and creating more data preprocessing steps. Knowing that the battery data variable, SOC, voltage, current, and temperature, have a dependent relationship over time, we chose to approach the solution using regression. To serve as an initial reference for this work, a recently published work [21] uses an FNN model to estimate SOC for a Li-ion battery, where the inputs were battery terminal voltage, battery temperature, averaged terminal voltage, and averaged current. The averages created for the current and voltage were on a rolling window of 400 timesteps, where each time step is one second.

The 400 timesteps window have presented the best results when compared to 100 timesteps.

The use of voltage and current averages on a rolling window was crucial for reducing the SOC estimation error to a reasonable value when compared using only the current and voltage at each time step. The averaged values transfer information from past timesteps to the present calculation, which gives the FNN the capability to consider past information. Other NN approaches, such as the LSTM recurrent neural network has within its gated structure the capability to record and select which past and current information can be used to calculate its output. The LSTM has been used recently to estimate Li-ion battery SOC in [137] and [23], where no average input was necessary, only $V(k)$, $I(k)$, and $T(k)$. However, the training process is significantly longer for an LSTM, especially when only a CPU (no GPU) is available for training. For example, training an FNN (2 hidden layers, 50 hidden units, 25ºC dataset) takes less than an hour with a CPU and may take many times longer for an LSTM with a GPU.

4.5. FNN Structure selection and number of neurons search

The chosen structure for SOC estimation at 25ºC was an FNN with five inputs: voltage $V(k)$, current $I(k)$, battery temperature $T(k)$, averaged terminal voltage $V_{avg}(k)$ and averaged current $I_{avg}(k)$ at time step k. The averages were computed based on the 500 previous one second time steps (rather than 400, as mentioned in the prior section, although in our exploration 400 and 500 seconds averaging had

similar results). The FNN structure was composed of two hidden layers, *L*, and numbers of neurons, *N*, in each hidden layer, as shown in **Figure 4.5**.
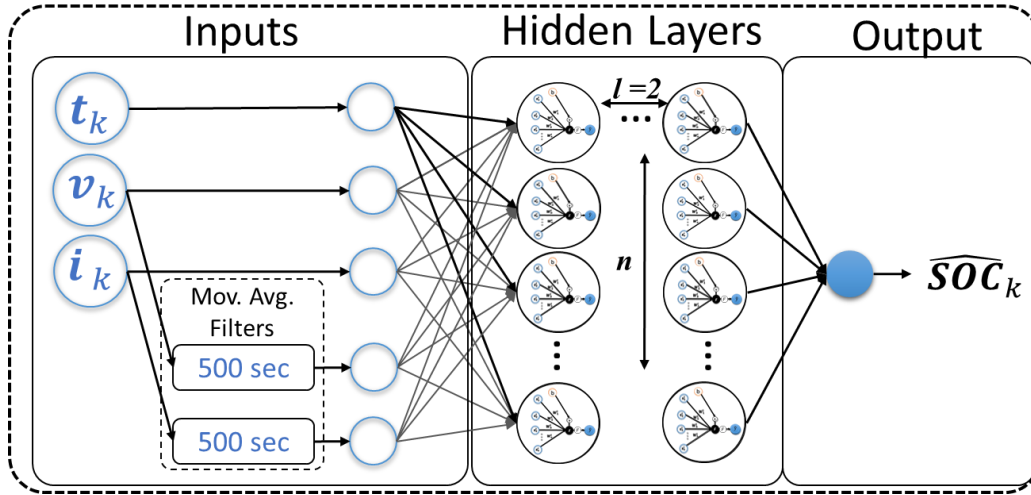
Figure 4.5 FNN structure used to estimate battery SOC

The FNN was trained with the number of hidden layers fixed to $L = 2$ and for the LG_HG2, 25ºC dataset, presented in **Table 4.3**. An algorithm, based on a simple "for loop" increment, was set to vary the number of neurons in each hidden layer, *N*, from 1 to 100, and the training was repeated for each configuration 100 times to ensure a consistent result.

The underlying reason to have such variation and repetition was to take into account the random initial weight/bias values when starting the FNN training process. Different seed values can lead to different local minima. The error ranged over nearly a factor of two for the 100 repetitions of the training performed for each FNN configuration shown in **Figure 4.6**, e.g., the FNN with 100 neurons in each hidden layer had RMSE minimum of 0.90% and max 1.45%, making it clear the initial values have a substantial effect on the training process.
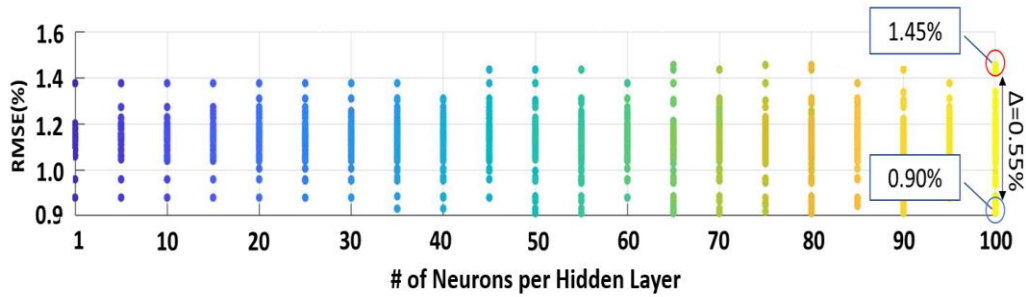
Figure 4.6 2000 model SOC estimation results divided into twenty groups of model configurations, based on the # of neurons per each of two hidden layers, where each configuration was submitted to 100 training repetitions.

The parameters used in all training processes are presented in **Table 4.3**, where each time the data passes through the NN during training is referred to as an epoch, and the learning rate (LR) is a scalar that is used to tune the step size of the gradient descent during the backpropagation. The learning rate is an essential tuning parameter because if it is too large, the local minima may not be found, and if it is too small, it will slow the training time considerably. A larger learning rate is used at the start of training, and the value is gradually reduced to improve the training process performance over time. This is implemented by scheduling several epochs, after which the LR will be reduced (LR drop period) and defining how much the LR will be reduced each time (LR drop factor). The LR drop factor is multiplied by the learning rate to update the value of LR for the next training iteration.

Table 4.3. FNN parameter values for structured training

Number of epochs	5100
Initial learning rate	0.01
Learning rate drop period	1000
Learning rate drop factor	0.1
# of hidden layers, L	2
# of neurons per hidden layer, N	1 to 100

115

Figure 4.7 shows the results from a different test where the FNN was trained only once at each variation of neurons per hidden layer, where the number of layers is again two. The three best results were obtained when the number of neurons per hidden layer was 55, 82, and 99 neurons.

The number of neurons for the NN structure was chosen to be N=55, the lowest number of neurons among the three best results in **Figure 4.7**. Fewer neurons imply that the model has fewer parameters and will require less computational resources. The detailed NN structure and the LG_HG2 li-ion SOC estimation plot is shown in **Figure 4.8**. The NN structure it is composed of five inputs, two hidden layers, 55 neurons in each hidden layer, the hyperbolic transfer function between both hidden layers, a 0.03 leaky rectified linear unit (RELU) layer, where a negative value will be multiplied by 0.03, and an output layer with a clipped RELU with the ceiling at 1. The use of the leaky RELU layer has significantly reduced the max error at the end of each discharge segment.
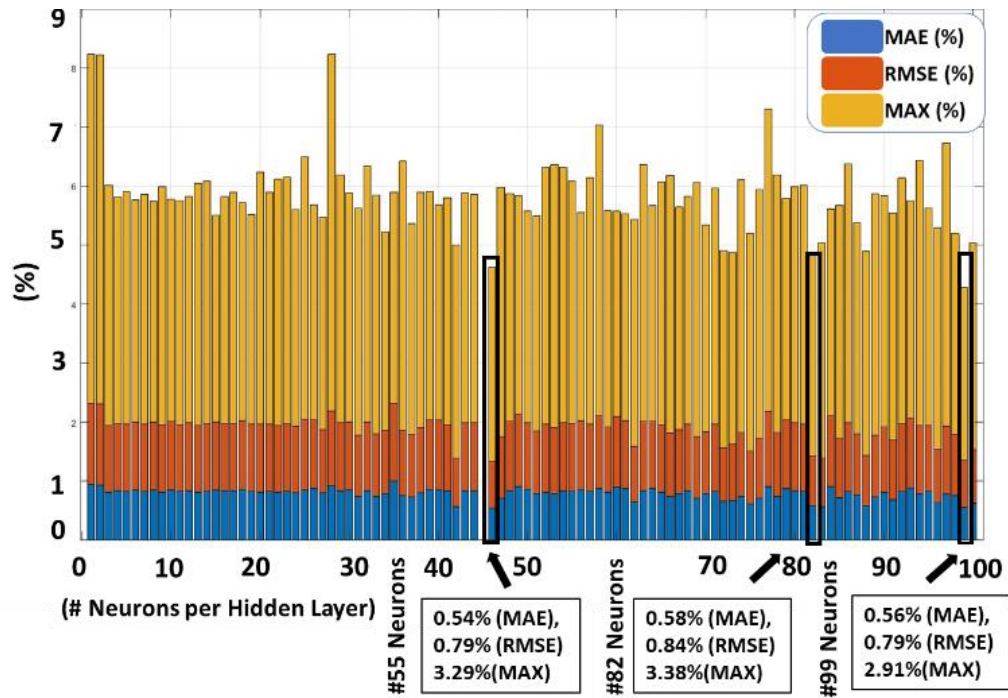
Figure 4.7 Lowest error case for each number of neurons per hidden layer case investigated, where N = 55, 82, and 99 have the best overall performance
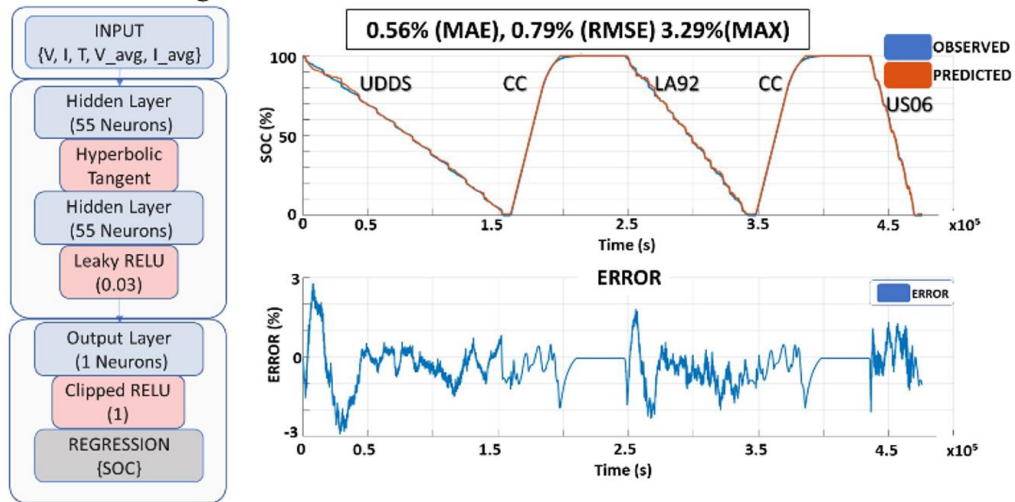
Figure 4.8 NN structure used to estimate LG HG2 battery SOC at 25⁰C, composed of five inputs, 55 neurons and 0.03 leaky RELU

4.6. Improving the robustness of the SOC estimation FNN model

As mentioned before, the FNN is a data-driven method, so the quality of the data used to train is paramount for the quality of the FNN as well. Although sometimes

the data with the necessary information to train the FNN model is not available or is very expensive to obtain, then as an alternative, some information can be artificially generated and added to the current dataset; this is referred to as data augmentation. There are several ways to artificially generate more data, such as using physical-based mathematical models. In the case of image classification problems, images can be augmented by creating distortions in the original image, for example, by flipping the original data horizontally as a mirror and adding the augmented image to the training dataset.

In the case of SOC estimation for xEVs, the sensors used to capture voltage, current, and temperature have a significant error due to the low-cost sensors typically used. If the expected error is known during the model design, the NN training dataset can be augmented to include error on the signals, improving the robustness of the resulting network. Table 4 shows the gain and offset error values that were used to augment the dataset for each feature in the dataset. The error values are similar to what would be seen in an automotive application. The SOC data based on the measured Ah was kept unchanged, as it is the objective. The model error is calculated based on the difference between the accurate measured values of the SOC and the model predicted values.

Table 4.4 Additional error added to the training dataset

Feature	Offset Error	Gain Error
Voltage	$\pm 4mV$	-
Current	$\pm 110mA$	$\pm 2\%$
Temperature	$\pm 5^{\circ}C$	-

The offsets values were added to its corresponding feature, e.g. if the voltage at time step k has initially been 4V, after adding the offset of +4mV, it became 4.004V. Likewise, a measured current of 1A with again error of -2% would become 0.98A.

Table 4.5 Cases used to increase the dataset with extra information

Cases	Current Gain Error	Current Offset	Voltage Offset	Temperature Offset
1 (Original)	0	0	0	0
2	+2%	0	0	0
3	+2%	+110mA	0	0
4	+2%	+110mA	+4mV	0
5	+2%	+110mA	+4mV	+5ºC
6	-2%	0	0	0
7	-2%	+110mA	0	0
8	-2%	+110mA	+4mV	0
9	-2%	+110mA	+4mV	+5ºC
10	+2%	-110mA	0	0
11	+2%	-110mA	+4mV	0
12	+2%	-110mA	+4mV	+5ºC
13	+2%	-110mA	+4mV	-5ºC
14	0%	-110mA	-4mV	-5ºC

Using the 14 Cases in **Table 4.4**, each with a different combination of current, voltage, and temperature offset or gain error. Therefore, the training dataset became fourteen times longer than the original Case 1.

4.7. Results and analysis of FNN trained for robustness, second cell type, and multiple temperatures

4.7.1.   Robustness of FNN with LG HG2 25ºC dataset

The NN structure and configuration presented in **Figure 4.8** (two layers, 55 neurons per layer) and the 25ºC LG_HG2 Li-ion dataset containing all 14 augmentation

cases listed in **Table 4.5** were used to train and test the estimation model. The results are presented in **Figure 4.9**, where it shows that despite the error added to the measured data, the model was still able to compensate and predict the SOC with reasonably good accuracy even when sensor error is significant (i.e. case 13). The RMSE, MAE and max model error is about double the error for the FNN trained with no error (**Figure 4.7**), but this is to be expected because the sensor errors add to the uncertainty of the relation between the model inputs and state of charge.

The error could likely be further reduced by training the FNN a large number of times as was done in the prior section, but this was impractical due to the large size of the dataset increasing the training the time needed for 10 hours. Higher accuracy could also be achieved by using genetic algorithms or backtracking search algorithms to select the number of layers [118] and optimum NN structure.
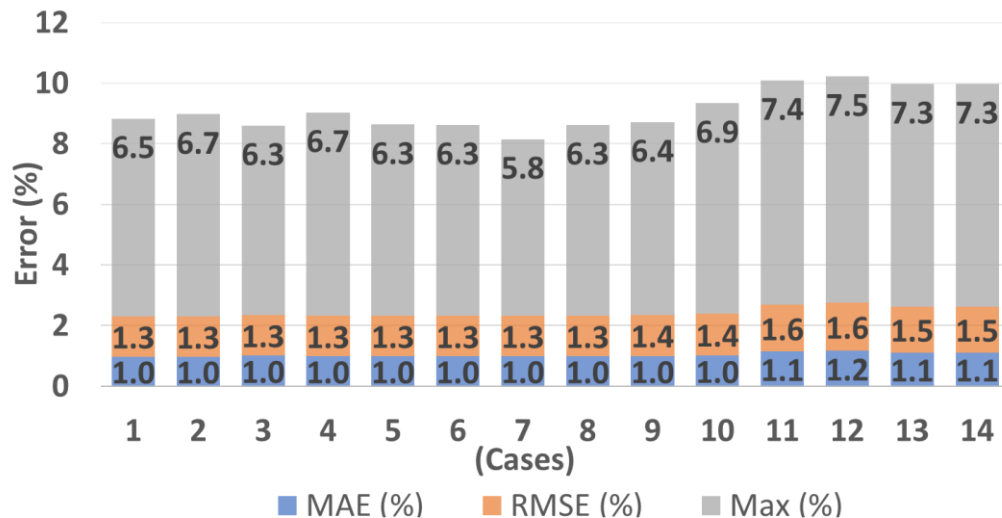
Figure 4.9 LG_HG2 SOC estimation error for each case described in Table 4.5

4.7.2. Validation of FNN on the Panasonic 25⁰C dataset

The same FNN structure shown in **Figure 4.8** and initially trained on the LG_HG2 data at 25⁰C was trained on the Panasonic 25⁰C dataset, as presented in **Table 4.1**. The FNN is only trained once, and 0.85% MAE and 6.65% MAX are observed, about double the error achieved with the LG_HG2 dataset in **Figure 4.7**. The SOC estimation plot in **Figure 4.10** shows that the error is generally less than 1% MAE and that it is the greatest for the most aggressive of the cycles, the US06. No augmented data was used in the case, as the purpose is just to demonstrate the model form also works well for another cell type. While the error is reasonable, it could be reduced by training the network multiple times or sweeping the number of neurons, as was done in prior sections.
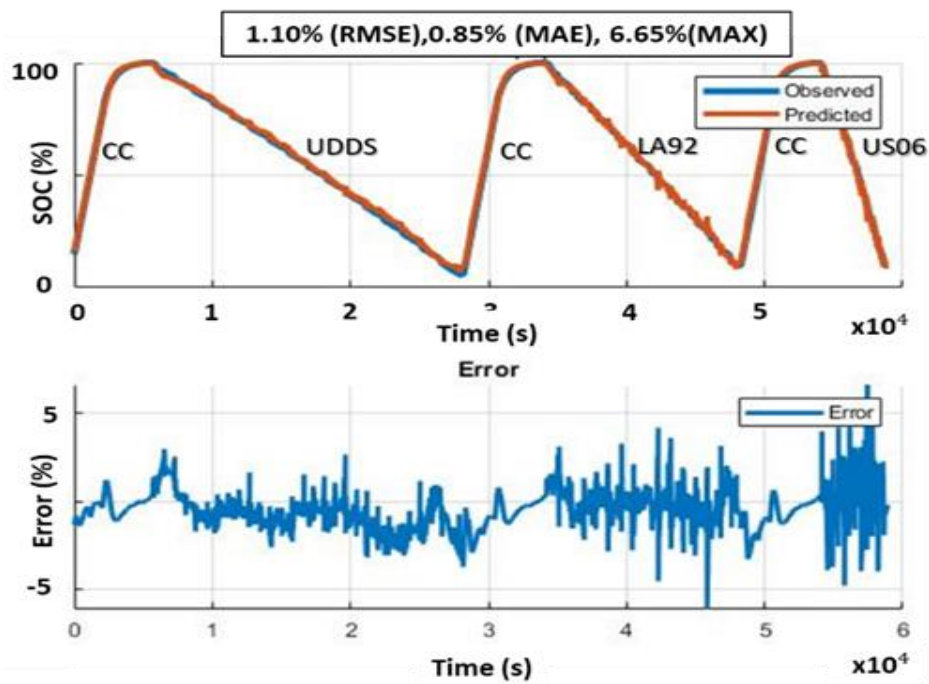
Figure 4.10 Results for two-layer, 55 neurons per layer FNN trained with the PANASONIC dataset at 25⁰C

4.7.3. Validation of the FNN model for LG HG2 with multiple temperatures

The whole LG_HG2 dataset (-10⁰C, 0⁰C, 10⁰C, and 25⁰C) is now used to train the two-layer, 55 neurons per layer FNN. The dataset is four times larger than the initial tests at 25⁰C. At low temperature, the Li-ion battery is subjected to effects that can reduce its life, power capability, and increase the complexity necessary to estimate its SOC, as discussed in [1]. This results in a higher error for the low-temperature cycles.

The results of the FNN trained on the multi-temperature LG_HG2 dataset are presented in
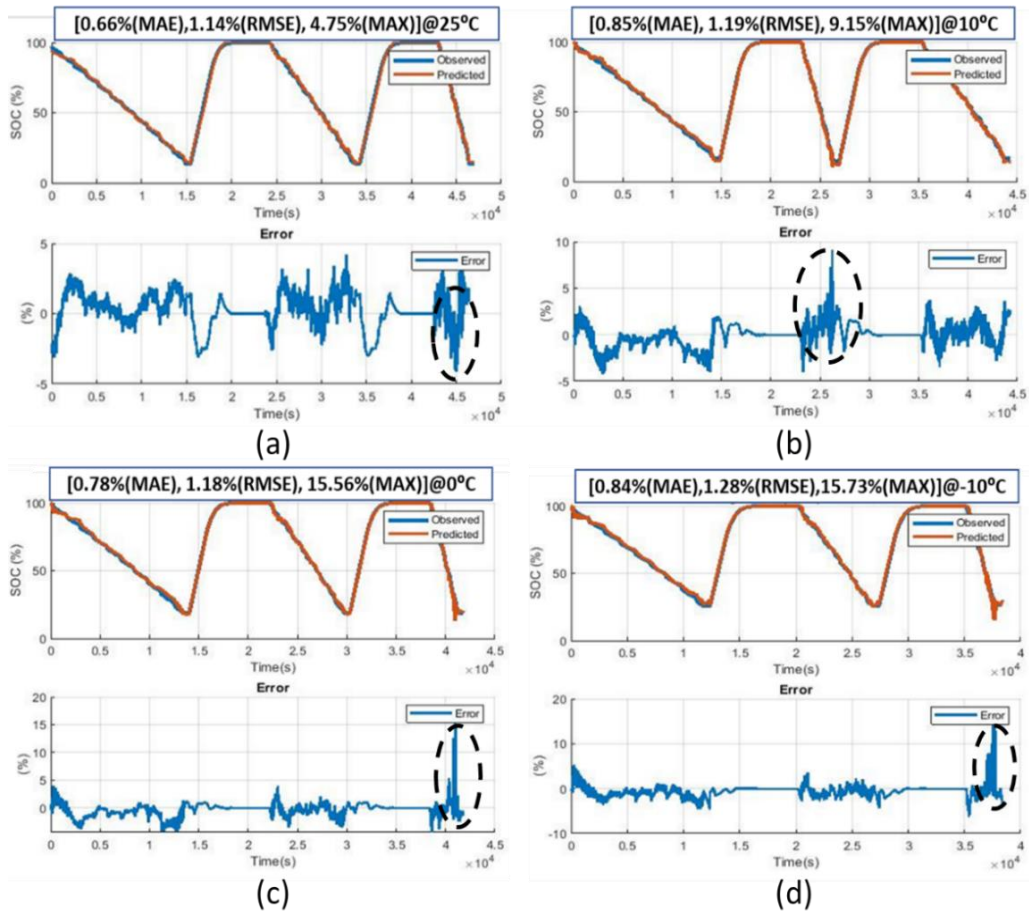
Figure 4.11 Results from the FNN model trained with an LG_HG2 dataset at four different temperatures (-10ºC, 0ºC, 10ºC, and 25ºC). (a) 25ºC dataset, (b) 10ºC dataset, (c) 0ºC dataset, and (d) -10ºC dataset. Dotted circles in the figure showing the max errors.

. Results show MAE kept under 1%, although the MAX error is close to 16% at 0⁰C and -10⁰C, and close to 9% at 10⁰C. In all cases, the higher error happens at the end of the US06 discharge, as shown in dotted circles in **Figure 4.11**.

Table 4.6 Results from the FNN model to estimate Li-ion SOC trained from the LG_HG2 dataset with multiple temperatures.

Temperature	RMSE (%)	MAE (%)	MAX (%)
25⁰C	1.14	0.66	6.65
10⁰C	1.19	0.85	9.15
0⁰C	1.18	0.78	15.56
-10⁰C	1.28	0.84	15.73

The higher error is due primarily to the much higher battery internal resistance at low temperatures. The US06 cycle is also a more challenging case, with a much higher discharge rate than the UDDS and LA92 cycles [9].
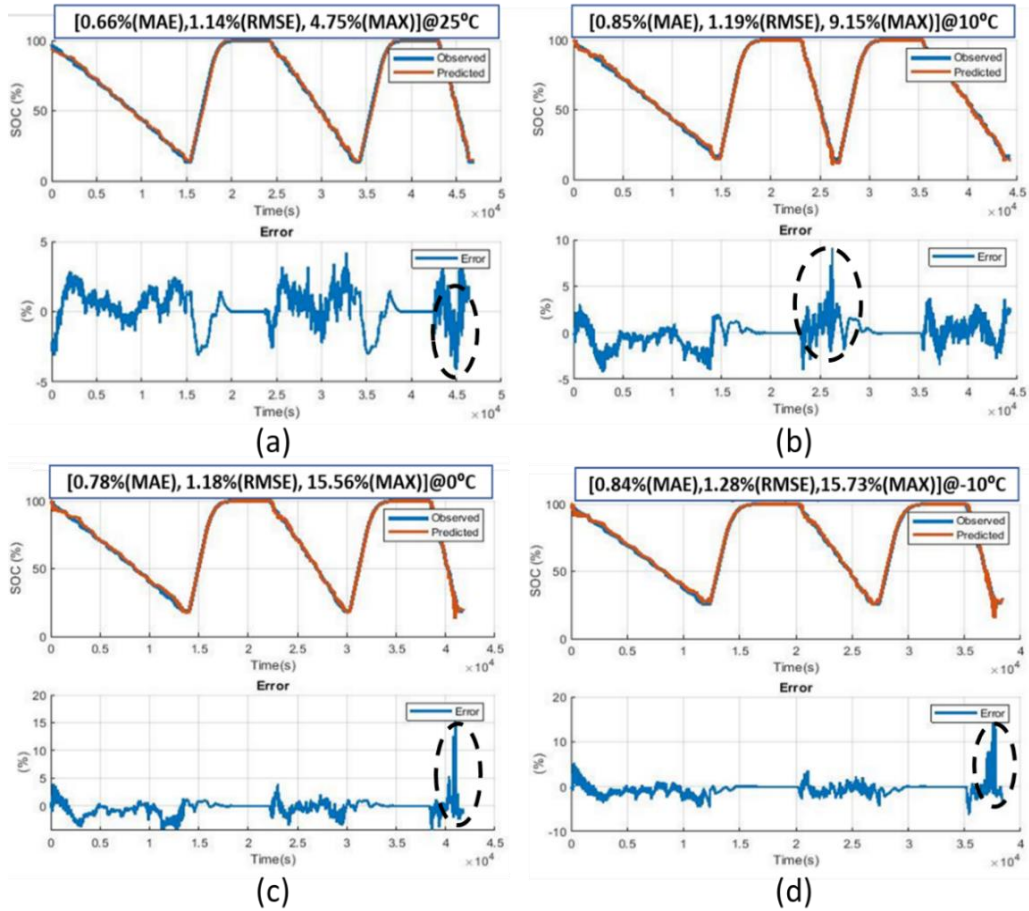
Figure 4.11 Results from the FNN model trained with an LG_HG2 dataset at four different temperatures (-10⁰C, 0⁰C, 10⁰C, and 25⁰C). (a) 25⁰C dataset, (b) 10⁰C dataset, (c) 0⁰C dataset, and (d) -10⁰C dataset. Dotted circles in the figure showing the max errors.

4.8. Hybrid Energy Storage System State-of-Charge Estimation Using Artificial Neural Network for Micro-Hybrid Applications

Many jurisdictions around the world, which have considerable automotive vehicle markets, are challenging the automakers to improve the fuel efficiency of cars and reduce emissions. The three biggest automotive markets, Europe, USA and China, have established targets to reduce CO_2 emission to 12%, 12%, and 18% respectively from 2017 to 2020. These reduction targets are related to an average of all new vehicle sales, and each automaker should achieve the targets, reducing their fleet CO_2 emissions on average, which means that the automakers can achieve different levels of efficiency for different cars if the average of the sales fleet achieves the target [1]. The electrified powertrain is one of the most effective technologies to enable the improvement of efficiency required, but to find the best trade balance between efficiency, production cost, and selling price is a challenge [5].

For the entry segment market, an engine start-stop system, i.e., a 12V micro-hybrid powertrain, which uses a belt starter generator instead of the alternator, coupled to the engine crankshaft by the front engine accessory drive (FEAD) belt can provide up to 7% energy recuperation[173].

Despite all benefits brought by this micro-hybrid powertrain to improve vehicle efficiency, the current amplitude of about 300A is required from the battery during charging and discharging. A standard Lead-acid (LA) battery, used on today's start-stop systems, is not capable of providing efficiently and continuously,

without severe degradation, this level of current for as long as it will be required [10]. Voltage instability is another issue observed when using only one LA battery as the vehicle voltage oscillations can cause, for example, fluctuations in heating, air conditioning fan, and lights. Although this problem can be solved by using an additional and smaller LA battery, e.g., 6 Ah, specifically for auxiliary load support, but it is still not solving the high current demand mentioned before. Another option would be to use one large 12V Li-ion battery, e.g., 60 Ah, but its relatively high cost shall reduce the affordability for this market segment, and crank capability is reduced for extremely low temperatures, e.g., -30℃, although, there were few improvements in this regard [174].

To satisfy all the requirements of this micro-hybrid vehicle, a 12V hybrid energy storage system (HESS) is proposed, combining two batteries in parallel: LA and Li-ion batteries as shown in **Figure 4.12**; where the LA battery is the battery responsible for providing the energy to the cold crank and also to supply energy to the vehicle electric auxiliary loads and a small Li-ion battery responsible for the power assist and regenerative braking[173].
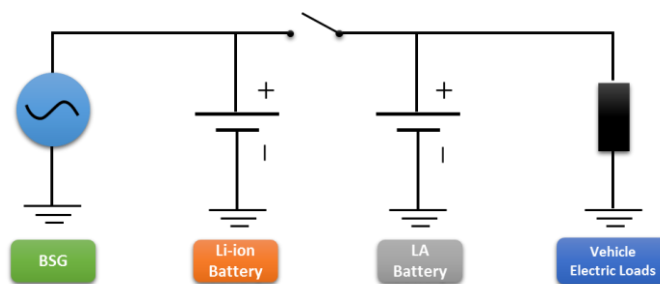
© 2020 IEEE

Figure 4.12 12V HESS topology

As mentioned before, this powertrain configuration is to address entry segment markets and then this system design is driven by its low cost and fuel consumption limited efficiency. Therefore, it is desired to reduce or avoid as much as possible higher costs, e.g., use of additional engine control unit (ECU) to perform the hybrid controls. For that kind of system, a simplified map-based control is used, and an accurate estimation of the batteries SOC is mandatory, as the entire map-based controls are dependent on the SOC. There are several methods to estimate the SOC. The most common is by using Coulomb counting (*4.1*), which integrates the current over time, as shown below:

$$SoC(t) = SoC(t_{init}) - \frac{1}{Q_{Ahr} * 3600} \int_{t_{init}}^{t} I(t)\eta_{bat} dt \qquad \textbf{(4.1)}$$

where Q_{Ahr} is the maximum capacity of the battery in Ah, η_{bat} is the efficiency of the battery [175][176][3]. Two main drawbacks of the Coulomb counting is the dependency on a reasonably good estimation of the initial SOC of the battery and its vulnerability to sensors accuracy errors that tend to increase by accumulation as the current is integrated. These problems can be solved by combining with Kalman Filters [177] that can rectify the initial value of SOC and then integrate the current over the desired period correcting the estimation towards the real SOC value. Another method, ECMs, has been used for modelling the voltage dynamics with the high current variation of batteries, where a typical ECM can be developed by adding one internal resistance in series to an open circuit voltage source and one resistance-capacitance (RC) circuit network to capture the first-order dynamics of

128

the battery terminal voltage, but more RC pairs can be added to capture higher orders dynamics [178]; for this method, it is also necessary to have a table with accurate OCV-SOC relation to estimating the SOC.

Recently, machine learning algorithms, such as artificial neural networks have been used to estimate the battery SOC as it can predict if appropriately trained, the SOC of any kind of battery without requiring any prior knowledge of its intrinsic physical characteristics, e.g., chemical composition or OCV-SOC relation [178], [179][151][180][48][137]. In this chapter, a new method to estimate the SOC of both batteries using only one FNN model is proposed. To develop this method, a set of different drive cycles, commonly used in the automotive industry, was used as a reference to train the FNN model [181][48]. The experimental batteries data was generated from a battery cycler using different drive cycles, and the batteries used in this work was an 8Ah Lithium Iron Phosphate (LFP) 12V battery and a 60Ah LA battery.

4.8.1.   FNN Model for SOC estimation

As stated before, the capacity of a feedforward neural network to approximate any function without knowing its features makes it a powerful tool to capture the nonlinear behaviour of batteries [182]. In this work for the first time, an FNN model was created to estimate the SOC of a 12V micro-hybrid vehicle HESS. Another interesting contribution from this work is the design of the FNN structure to estimate the SOC of both batteries simultaneously, as shown in **Figure 4.13**.

4.8.1.1.   Preprocessing and selecting data

Firstly, the available data were analyzed regarding consistency and quality to be confident that it can be appropriately used and avoid misinterpretation of initial simulation results.

The data used in this work was collected using a 100 Hz sample rate from six different homologation drive cycles. This represents roughly 1.5 million data points. Although, by analyzing the data, it was observed that the influence of the measurement variations within ten milliseconds is negligible. It was implying that resampling the data to a lower rate can be done without losing relevant information to estimate the SOC. Afterwards, the data were resampled to 1 Hz, reducing the processing time considerably during FNN training.

Another critical step was the scaling of the data, setting all input values between 0 and 1, which in this case proved to reduce the estimation error considerably, e.g. by a factor of over a hundred [151].

Finally, a selection had to be done regarding what data shall be used for training and what shall be used to validate the SOC estimation. For simplicity and to avoid mistakes, it was decided to use 5 of the 6 available drive cycle data to train the model and the sixth drive cycle data not used during training to validate the model. The drive cycle selected for validation was the Worldwide harmonized Light vehicles Test Cycle (WLTC) created by the United Nations Economic Commission for Europe (UNECE) to represent the typical driving characteristics in different places over the world [183][184].

4.8.1.2.   FNN structure

The structure of the FNN was created in Matlab 2016 environment using its neural Network Toolbox. The FNN structured was configured to divide the training data into training, validation and test set. However, it was randomly separated according to the respective proportional distribution of 70%, 15%, and 15%. This division is necessary to perform validation checks during the training process to update the weights and biases, as explained before. The first neural network performance, during training, has been measured by using the mean square error (MSE). The number of epochs initially set was 2000, and a max validation check, also known in as patience, was set to 100. These parameters were tuned in a way to avoid overfitting and, at the same time, maintain good generalization to adapt well when tested with unknown data. After several adjustments theses parameters were set as follows: performance (MSE) set to a minimum of $1e^{-5}$ and max epochs set to only 50.

The transfer function chosen to compose the structure was the hyperbolic tangent transfer function "*tangsig,*" which keeps the neurons output values bounded between -1 and 1. To improve the generalization of the neural network, Bayesian regularization method is used, which can automatically set the regularization ratio to avoid overfitting. On Matlab, this is realized by the training function "*trainbr.*" The training process can be observed on the Matlab toolbox diagnostic window.

Another critical step is the selection of the number of hidden layers and the number of neurons in each hidden layer. The larger the number of neurons and hidden layers, the longer it will take to train the neural network. Finding a good balance between the accuracy and complexity of the neural network is a challenge that, in general, requires great engineering experience and effort. In this work, the best configuration found was 12 inputs with 2 hidden layers, with 4 and 2 neurons, respectively, on the first and second hidden layers. This structure was designed to estimate the SOC of both LA and LFP batteries at the same time, as shown in **Figure 4.13**.
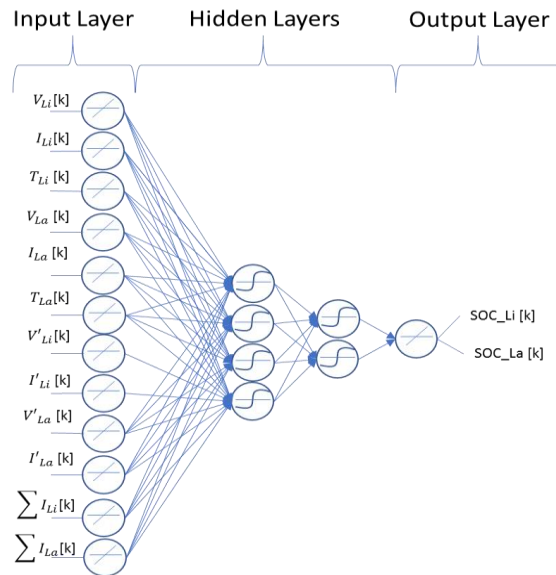
Figure 4.13 The architecture of the four-layers network and 12 inputs, 6 from each battery, for estimating SOC from LFP and LA batteries

The use of the terminal voltages, currents, and temperatures from both batteries as inputs were not sufficient to accurately estimate the SOC. Other inputs had to be derived, including the first derivative of both voltages and currents from the two

batteries and the integration of each battery current. All data acquisition happened at ambient temperature, but battery temperature increased considerably during each test, e.g. the LFP went from 23℃ to 51℃ on FTP75 and from 23℃ to 37℃ on WLTC. By including the temperature as an input, it is observed to reach better accuracy on SOC estimation.

4.8.2. Battery data acquisition

The LA battery used in this experiment was a 12V Enhanced Flooded Battery (EFB), which is a type of LA battery used for partial state of charge (PSOC) applications that are required by start-stop and hybrid electric vehicles [185]. The Li-ion battery used in this work was an 8 Ah LFP, which is known to be one of the safest Li-ion chemistries, is also known to be one of the most difficult to estimate the SOC due to its almost flat relation between the OCV and SOC, especially on mid-SOC regions as shown on **Figure 4.14**, where the variation of voltage is disproportionally smaller than the SOC [8].
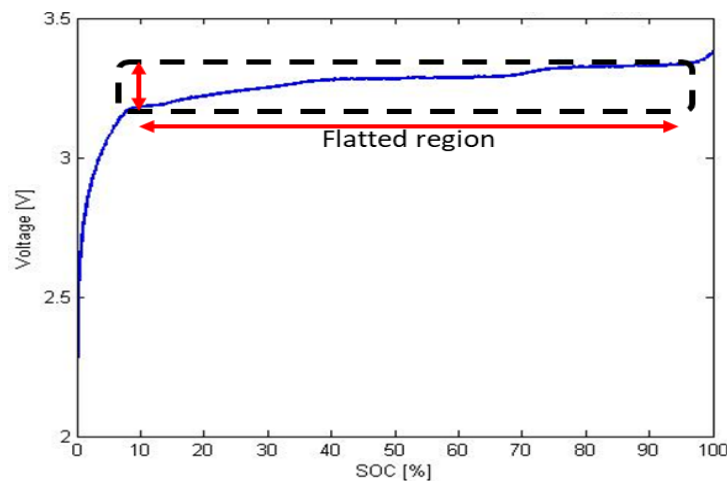
© 2020 IEEE
Figure 4.14 LFP cell OCV [V]-SOC [%] relation

The two batteries are connected, as showed in **Figure 4.12** and were tested inside of the thermal chamber, controlling the environment temperature to be constant at 23℃. Only one sample of each battery has been used to perform the drive cycle tests.

The test was managed by an AVL's PUMA, an automation system that controls the tests and all measurements. A micro-hybrid vehicle simulation running on the Matlab environment to generate the current and voltage demand profiles for both batteries were generated; those profiles were uploaded on the AVL PUMA to connect to a battery cycler. The battery cycler operation range is shown in **Table 4.7**.

Table 4.7 Battery cycler

Battery cycler operation range			
Output	*Min*	*Max*	*Accuracy*
Current	+ 600 A	- 600 A	+/- 0.1%
Voltage	8 V	60 V	+/- 0.1%

For this experiment, each drive cycle was tested only once to avoid any damage to the battery samples. Six homologation drive cycles were used in the experiment: NEDC, WLTP, US06, FTP75, Highway, and GUDC, which is a drive cycle that emulates a real-world driving condition.

Two different SOC estimations were generated in the experiment:

i. *From the battery cycler, an accurate SOC estimation, used as a reference to measure the accuracy of our method for both batteries.*

134

ii. From a commercially available BMS equipping only the LFP battery that will be served in this work as benchmarking.

4.8.3. Results and discussion

After building the FNN model to estimate the SOC of both batteries it was possible to optimize to obtain good accuracy to the objective SOC. The FNN was trained using the combination of five of the six drive cycles. The drive cycles used to train the FNN was the FTP75, NEDC, US06, GUDC, and Highway. As already mentioned, the WLTC drive cycle was not used during the training section to be used after training to validate its capacity to estimate the SOC.

The lowest estimation errors are presented in **Table 4.8**, together with the approximation error of the BMS for the LFP. Only 50 epochs were necessary to reach an RMSE below 1%.

Table 4.8 NN Backpropagation RMSE result

Drive Cycle - WLTC			
Method	**Battery**	**RMSE (%)**	**MAE (%)**
FNN	LFP	0.33	0.27
	LA	0.84	0.80
BMS	LFP	0.60	0.46
FNN	LFP	0.33	0.28
±3% Input bias	LA	0.84	0.80

© 2020 IEEE

Although the BMS has an accurate SOC estimation with an RMSE around 0.60%, the FNN proves to have more accurate estimation with an RMSE around 0.33%. The plot of the SOC estimation from the FNN, BMS, and battery cycler is shown in **Figure 4.15**.
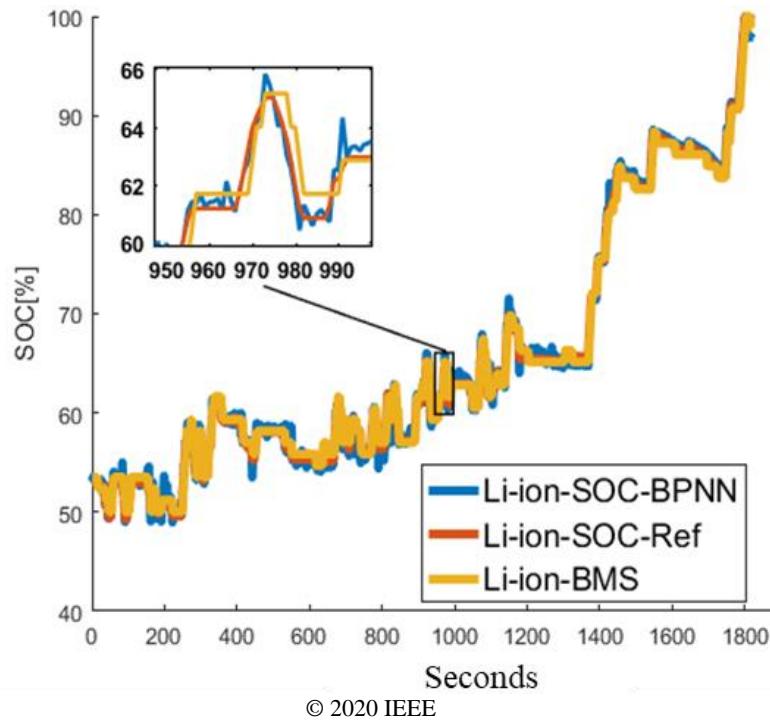
Figure 4.15 WLTC LFP battery SOC [%] estimation from PBNN, BMS and Reference (Cycler)

The results presented from the FNN method encouraged other tests to understand its limitations better. As it is well known that current sensors exhibit measurement error, and it is an important parameter to be taken into account when, for example, using EKF [186][187]. To improve the model robustness to input noises, in a more straightforward way to what was presented in section 4.5, it was added +3% and -3% gain to the voltage, current, and temperature inputs of both batteries, during training and validation. This was done to investigate how the FNN would respond. The results are shown in **Table 4.8**. Similar results were achieved when the test was performed without the input gain, which indicates that if the neural network is properly trained considering similar sensor noises in the training dataset used, this method can compensate for the error and can accurately estimate the SOC. **Figure**

136

4.16 shows in the same plot the SOC estimation of both batteries with the -3% bias on the inputs.

© 2020 IEEE
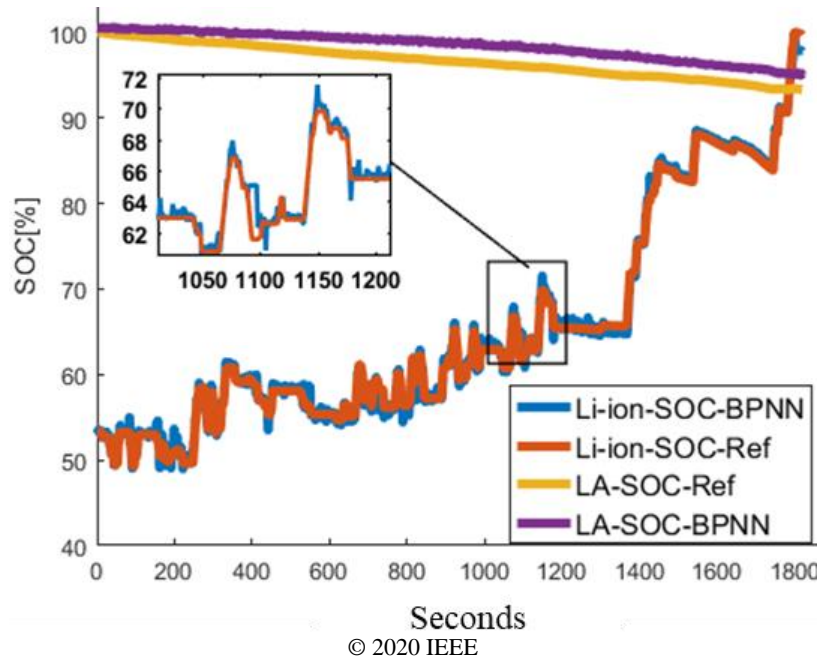
Figure 4.16 WLTC LA and LFP battery SOC [%] estimation with -3% bias on inputs

It is possible to see that the SOC of the LA presented a slow descent during the cycle, from 100% to about 96% SOC, while the LFP shows a charging and discharging behaviour, starting from 52% SOC. The obtained LA SOC RMSE is about 40% less accurate than the LFP SOC RMSE. Due to the use of only one structure to estimate the SOC of the two batteries, great effort was necessary to correctly tune the FNN to obtain a good tradeoff between both estimations. For example, a much lower estimation error for the LA was obtained while the LFP estimation error was, in general, ten to a hundred times higher.

137

4.9. Concluding remarks

The process of designing an FNN to estimate the SOC of a Li-ion battery for xEV applications requires several iterations and variations of design variables. A good understanding of the intended application is also necessary to perform augmentation of both data and modification of the FNN structure to improve SOC estimation. The FNN performance is a strong function of the training data, and the quality of the data is, therefore, essential for achieving good performance.

In order to improve the robustness of the model, as shown in section 4.4, the data used to train the FNN was augmented with information based on the expected limitations of the sensors typically found on an automotive BMS. The FNN showed some limitations, especially regarding a higher maximum error when trained with multiple temperatures, but this may be improved by including augmented data and run more training iterations to select the best model, as done for the single temperature model shown in **Figure 4.6**. The FNN model was found to be capable of estimating the battery SOC with accuracy under 1% MAE in section 4.7.

In section 4.8, an FNN was built to estimate the SOC of a HESS composed of one 12V LFP battery and one 12V LA battery. The results were compared to the SOC calculated by a battery cycler. The lower SOC approximation error obtained for the LFP battery was 0.33% RMSE, and the LA battery was 0.84% RMSE. The FNN LFP approximation error was also compared to a commercially available BMS showing better results. The FNN was also tested, including a ±3% gain to its

inputs to simulate the measurement noise commonly observed in sensors for automotive applications. This approach is similar to what was presented in section 4.4. As expected, the results were similar to those obtained without including the extra gain. A significant contribution from this part of the work was the use of only one neural network structure to estimate the SOC of two different batteries, which proved challenging as it required great effort to establish the right neural network parameters to estimate both batteries SOC under 1% error RMSE.

However, factors such as battery ageing were not considered; they remain items considered for future work as well as a more detailed analysis of each drive cycle, especially the more aggressive ones. Other avenues for future work include the comparison and the use of recurrent neural networks such as LSTM as well as the test of different NN training algorithms and structures to reduce the accuracy variation in the search for the global minima. The datasets, LG_HG2 and Panasonic, used in section 4.7, as well as the Matlab script used to train the NN, are publicly available to download in [171].

5. RECURRENT DEEP NEURAL NETWORKS APPLIED FOR BATTERY TERMINAL VOLTAGE MODEL AT MULTIPLE TEMPERATURES

5.1. Equivalent circuit type battery models

As an alternative to Thevenin based ECMs briefly presented in the previous chapters, this chapter presents machine learning methods based on gated recurrent neural networks. A similar approach was presented in [188] when a Li-ion cell Voltage Model (VM) based on a GRU (GRU-RNN) was used to estimate the battery terminal voltage. Two VMs based on LSTM and GRU are developed and compared in this chapter. As one of the main contributions of this work is that until the present moment, the VMs, based on LSTM (LSTM-VM), is developed and presented for the first time. The LSTM-VM is benchmarked to GRU-VM, and a third-order Thevenin based ECM on a wide range of temperature and two different Li-ion batteries. Therefore, the novel LSTM-VM and a comprehensive comparison to GRU-VM and Thevenin ECM compose the main contribution of this chapter.

In sections 5.2 and 5.3, the models are presented, in section 5.4, training methods for the LSTM-VM and GRU-VM is presented as well the data collection information, and in section 5.5 the models are compared based on their performance and accuracy.

5.2. Thevenin ECM

As already presented in section 2.3.2 the ECM, based on Thevenin theorem, can represent the battery dynamics reasonably well, using an electric circuit representation with one or more parallel RC, where the higher the number of RC series elements are incorporated, the higher becomes the polynomial order and the more complex become the model[42], [43]. To maintain the model accuracy when

submitted to a wide range of ambient temperatures, it requires the OCV-SOC and R_0 to be a function of the temperature. As the temperature has a significant impact on the internal battery phenomena, for example affecting the diffusion rate, internal resistance and battery capacity. It may be necessary to increase the order of the ECM and add the Butler-Volmer relationship to represent the nonlinear aspect of the resistance, especially at low temperatures and therefore improve the accuracy of the model. However, as a consequence, the engineering effort, computational complexity to obtain all the parameters for ECM also increases.

The ECM used as a benchmark for this work was a third-order ECM, which consists of an OCV in series with a nonlinear resistance, R_0 and three parallel RC pairs, as shown in **Figure 5.1**. An HPPC test method, together with quadratic-based programming, was used to parametrize the model variables. This author did not develop the Thevenin ECM used to generate these results used as the benchmark.
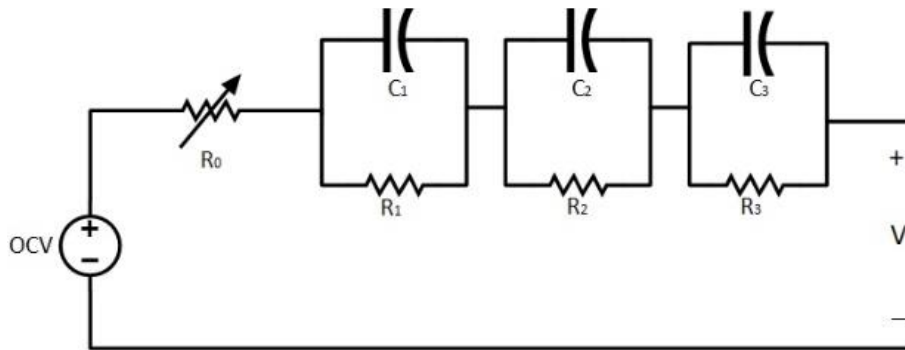
Figure 5.1 Third-order ECM with nonlinear resistance R_0

5.3. LSTM and GRU recurrent neural network ECM

As mentioned in section 3.2.5, the recurrent neural network is a sub-type of neural networks that reuses information from previous time steps in a closed-loop fashion.

Some RNNs have limitations when encoding long-term dependencies from the data into the model. This is due to the *vanishing* or *exploding* gradient that happens during backpropagation, the process where model parameters are proportionally adjusted based on the partial derivative of the loss function [134]. To reduce the vanishing or exploding gradient problem, gated regulated RNNs, such as the LSTM [135], bidirectional LSTM (**Figure 3.9**), and GRU (**Figure 3.10**), use a set of *gates* and the hidden and memory states to help the RNN learn long-term dependencies embedded in the data. **Figure 5.2** shows the LSTM and GRU unfolding in time, as their states generated in a time-step are used as input in the next. The LSTM, compared to the GRU, has a more complex structure, with three gates (input, forget, and output) rather than two (reset and update), and the LSTM uses a memory cell and hidden states components to encode time-related content, unlike the GRU that has only the hidden states. For further details, refer to sections 3.2.5.1. For these reasons, it was hypothesized that the LSTM would perform better for ECM type modelling, a hypothesis that is generally supported by comparing the results of this chapter to the GRU-VM investigated in [188].
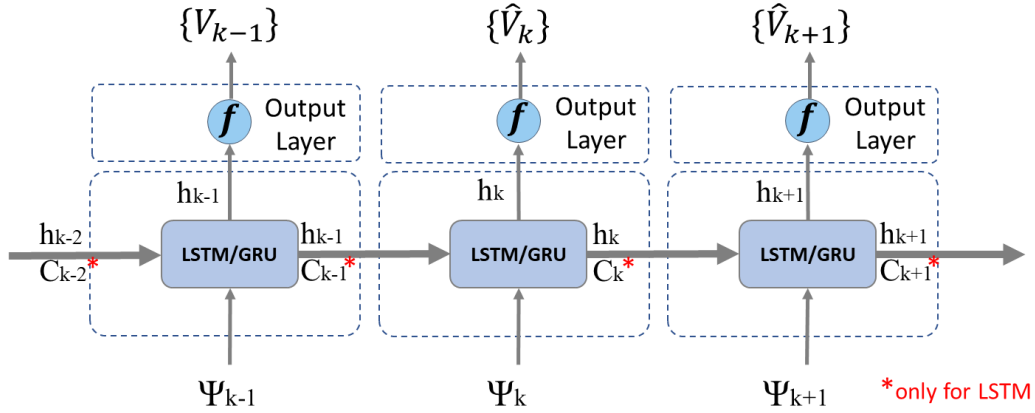
Figure 5.2 LSTM or GRU models unfolded in time, although the GRU has only hidden states (h_k) and no C_k as it does the LSTM

The LSTM-VM and GRU-VM models are composed of ten and twelve hidden units, respectively and an output layer with a fully connected layer with one neuron, as illustrated in **Figure 5.3(a)** and **Figure 5.3(b)**. The activation function in the output layer is a clipped rectified linear unit (Clipped RELU), which limits output values between zero and one. The input matrix is $\mathbf{\Psi}_k = \{\boldsymbol{Ah}_k, \boldsymbol{I}_k, \boldsymbol{T}_k\}$, where $\boldsymbol{Ah}$ is the calculated ampere-hours discharged from the cell (analogous to SOC), $\boldsymbol{I}$ is the measured battery current, and $\boldsymbol{T}$ is the measured battery temperature. The models' output is the estimated battery terminal voltage, represented by $\widehat{\boldsymbol{V}}$. The total number of learnable weight and bias parameters for the LSTM-VM and GRU-VM, respectively, are 571 and 589, but from now on will be referenced as 600 parameters for both models. Although, the GRU-VM presented in [188] also used as a benchmark has 3150 parameters
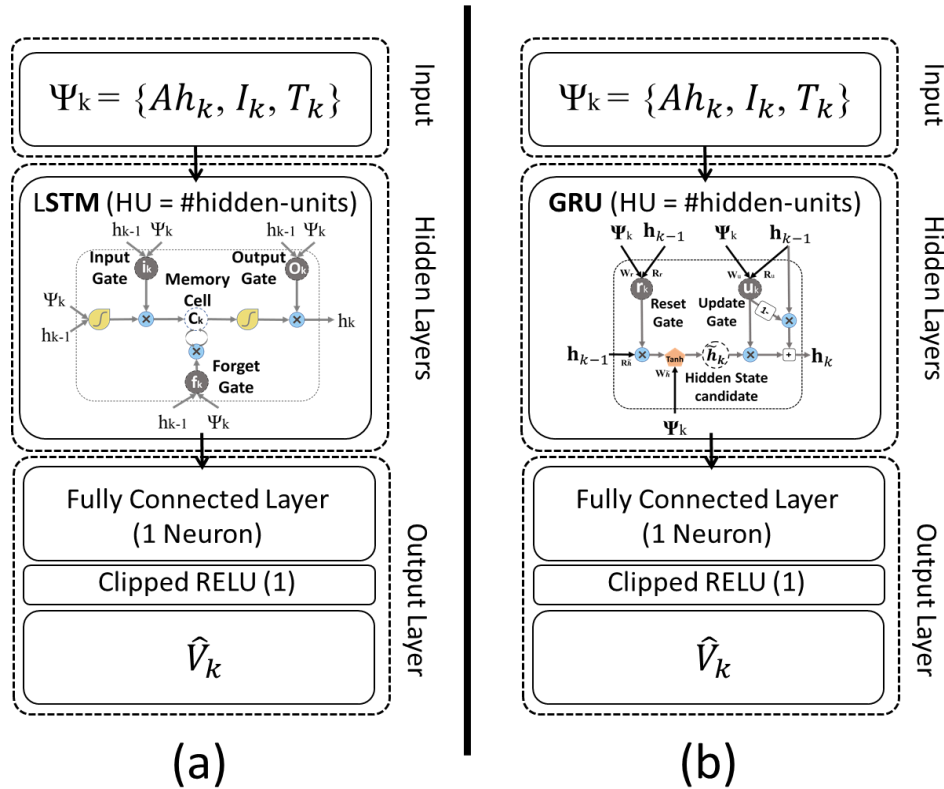
Figure 5.3 (a) LSTM-VM, and (b) GRU-VM model structure for xEV Li-ion battery

5.4. LSTM-VM and GRU-VM Training

Both LSTM-VM and GRU-VM models were trained and tested using the dataset and equipment presented in **Table 5.1** for each of the batteries, Panasonic and Samsung T30, including all listed temperatures. The schematic of the test bench and the data logging system is presented in **Figure 4.3**. The testing dataset it is also listed in **Table 5.1**, but in the case of the Panasonic dataset only UDDS, LA92, and NN were used to validate the models, but in the case of the Samsung T30 only the "Mix" drive cycles were used to train and the UDDS, LA92, HWFET, and US06 cycles for testing. About 2/3 of the data is used for training and 1/3 for testing, a common ratio of training to testing data, which helps to ensure good training and

thorough evaluation of the network's performance. The whole dataset was down-sampled to 1Hz to reduce the amount of time required to train the model. The data was also normalized, which improves model accuracy and training speed by setting all inputs and outputs to a similar value [13].

Table 5.1 Batteries, datasets and lab equipment

Battery Datasets	Panasonic[189]	Samsung T30
Training	Mix 1 to 4, HW, and US06	Mix 1 to 8,
Testing	UDDS, LA92, NN	US06, UDDS, HW, LA92
Temperatures	-10ºC, 0ºC, 10ºC, 25ºC	-20ºC, -10ºC, 0ºC, 10ºC, 25ºC, 40ºC
Cycler manufacturer	Digatron firing circuits	Digatron firing circuits
Test channel	25 A, 0–18 V channel	75 A, 0–5 V channel
Data acquisition	10 Hz	10 Hz
Accuracy	±0.1% full scale	±0.1% full scale
Thermal chamber	Cincinatti subzero ZP8	Envirotronics
Size	8 cu. Ft.	8 cu. Ft.
Accuracy	-	±0.5 ∘C

For each training case, the process continued for around twenty thousand epochs and took about eight hours. As mentioned previously, an epoch represents a pass of the whole training dataset through the model, and in this case, the dataset was organized in one batch, so one epoch also represents one update of the model parameters. The initial learning rate was set to 0.01, with the learning rate reduced by 85% every 2000 epochs. The network was created in MATLAB 2019b, and an NVIDIA Titan X Pascal GPU was used to train the model. The training process was repeated at least five times due to the reasons addressed in sections 3.2.7 and 4.5.

5.5. Results and Analysis

In this section, the results from the novel LSTM-VM proposed model are compared with the ECM, third-order Thevenin based, and GRU-VM models using the dataset of two different Li-ion batteries at a wide temperature range, including low

146

temperatures situations. This section is divided into parts: 5.5.1 LSTM-VM versus ECM, and 5.5.2 LSTM-VM versus GRU-VM.

5.5.1. LSTM-VM vs ECM

In this section, all the results presented are based only on the Samsung T30's *UDDS*, *HW*, *LA92*, and *US06* drive cycles at each of the six tested temperatures presented in **Table 5.1**. The measured current, amp-hours or SOC, and cell temperature are the inputs for each model, $\Psi_k = \{Ah_k, I_k, T_k\}$, and the estimated terminal voltage is the output, $\hat{V}$.

The third-order ECM model parameters are calculated, through quadratic-based programming, at each time-step by interpolating between the model parameter, based on the temperature and SOC input values. At the same time, for the LSTM-VM, this relation is extracted directly from the data during the training process. The RMSE of the voltage estimations presented in **Figure 5.4**, showing that in 92% of the cases, the LSTM-VM performed better than the Thevenin ECM. The RMSE of the ECM and LSTM-VM range from 15 to 120 mV and 13 to 46 mV, respectively. At 25^0C and 40^0C, the ECM achieves relatively low RMSE between 15 and 37mV and performs slightly better than the LSTM-VM for the UDDS cycle.
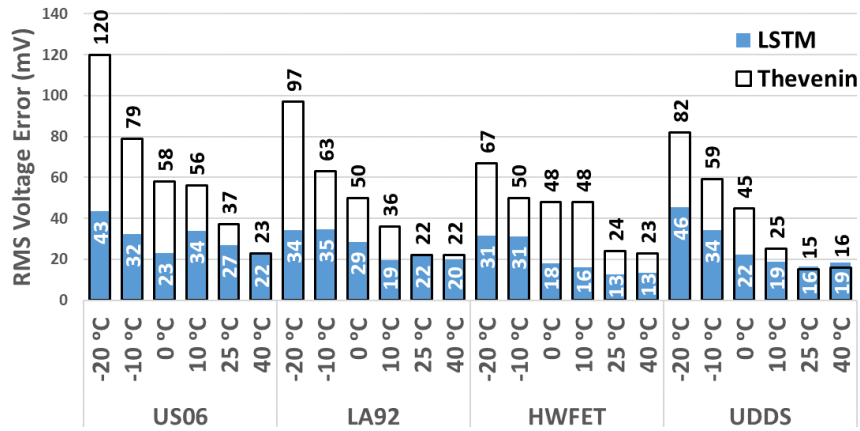
Figure 5.4 Samsung T30 ECM and LSTM-VM RMS voltage error for each drive cycle and temperature

The performance of the two models starts to diverge as the temperatures get lower, though, with the LSTM-VM having RMSE less than half that of the ECM for temperatures ranging from -20 to 10°C. The average RMSE for the four tested cycles at each temperature present as a function of temperature in **Figure 5.5**, showing that at low temperatures, the ECM error is double or more than the LSTM-VM error. The nature of the LSTM-VM training, which weights the error at every timestep equally, also results in the error being more similar across temperature. The LSTM-VM training process effectively gives up some accuracy at higher temperatures to achieve greater accuracy at lower temperatures, a reasonable trade-off considering that the main limitation of the ECM is the high error at low temperatures.

148
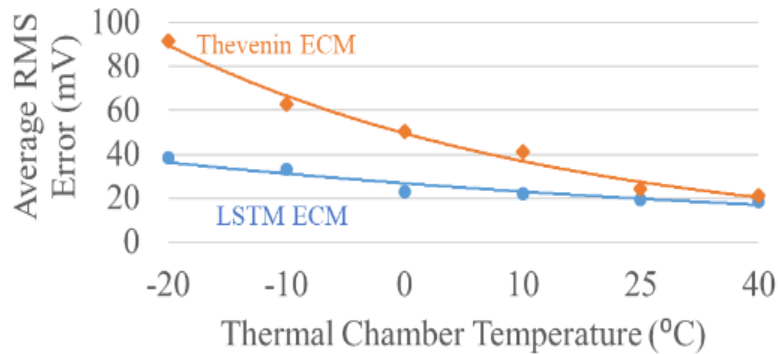
Figure 5.5 SamsungT30 ECM and LSTM-VM average RMS voltage error versus all temperatures

In summary, the Thevenin ECM performs well for the 25⁰C and 40⁰C cases but has significant error for lower temperatures. The LSTM-VM performs well at all temperatures and has much lower error than the ECM at low temperatures. For cases where only higher temperatures are of interest, or where less aggressive drive cycles or other discharge profiles are used, the ECM should be sufficient, while for more challenging cases the LSTM-VM is likely to achieve superior performance as it has here.

To provide further insight into the differences between the two models, **Table 5.2** provides a brief comparison of the models according to a few quantitative and qualitative aspects. This shows the ECM has some benefits, including lower computational effort required to determine its parameters and the use of parameters that can be derived from a physical paradigm. Then, on the other hand, LSTM-VM has fewer model parameters, requires less engineering effort to develop, and has a greater ability to fit the nonlinear and time-dependent behaviour of the battery,

presumably due to the deep neural network model form and the training of the model with actual drive cycle data rather than HPPC data.

Table 5.2 Comparison between LSTM-VM and ECM

	ECM[*]	LSTM-VM
Parametrization Tests Required at Each Temperature	HPPC	Eight drive cycles (Mix 1-8)
Number of Parameters	960	600
Computational Effort of Model Parametrization	Low *(Fitting)*	High *(Training)*
Engineering Effort to Create and Parametrize Model	High *(Custom software tools)*	Medium *(Standard software tools)*
The ability of the Model to Incorporate Complex Nonlinear, Time-Dependent Behavior	Medium *(Function of model form and HPPC data)*	High *(Model captures behaviour in training data)*
Can trace to a physical paradigm	Yes *(Parameters capture OCV, R)*	No *(Parameters are abstract)*

5.5.2. LSTM-VM vs GRU-VM

In this section, all the results presented are based only on Panasonic's UDDS, LA92, and NN drive cycles at each of the four tested temperatures presented in **Table 5.1**. As shown in **Figure 5.3**, the measured current, amp-hours, and cell temperature are the inputs for each model forming the input matrix, $\boldsymbol{\Psi}_k = \{\boldsymbol{Ah}_k, \boldsymbol{I}_k, \boldsymbol{T}_k\}$, and the estimated terminal voltage is the output, $\widehat{\boldsymbol{V}}$.

As already mentioned in section 0, the GRU-VM has already been introduced in [188]. Although, despite using the same battery dataset, Panasonic dataset available in [189], the LSTM-VM presented better accuracy than the GRU-VM, as shown in **Figure 5.6** when both models were compared based on the NN drive cycles at different temperatures. It is showing that only at 25⁰C, the GRU-VM

(3150 parameters) presented better results, despite using more than five times the

number of parameters used for the LSTM-VM (600 parameters).
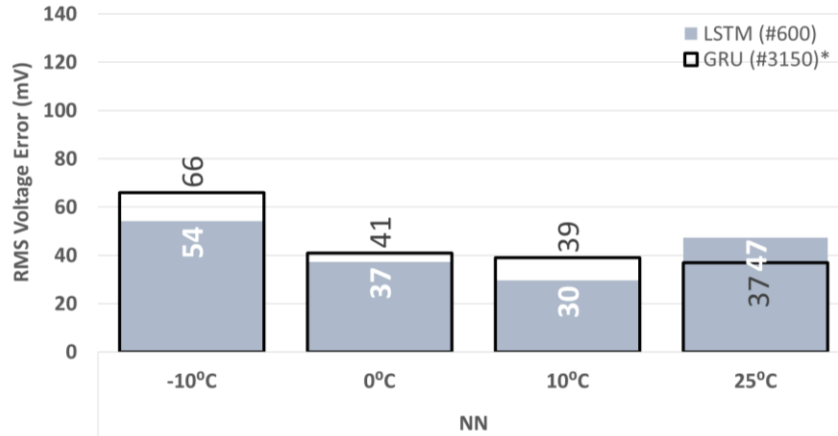
Figure 5.6 Panasonic RMS voltage error for selected LSTM-VM model results comparing to GRU-VM result presented in [188]

Even though this initial comparison is not sufficient to guarantee that the LSTM-

VM is indeed superior to the GRU-VM. One crucial difference relies upon the fact

that the GRU-VM developed in [188] have used a different part of the Panasonic

dataset to train the model, as shown in **Table 5.3**, and was not mentioned by the

author whether or not they have considered the variation of the results due to

different local minima.

Table 5.3 LSTM-VM

Model	LSTM-VM	GRU-VM[188]
Number of parameters	600	3150
Battery Datasets	Panasonic[189]	Panasonic[189]
Training	Mix 1 to 4, HW, and US06	US06, UDDS, HW, LA92
Testing	UDDS, LA92, NN	NN
Temperatures	-10ºC, 0ºC, 10ºC, 25ºC	, -10ºC, 0ºC, 10ºC, 25ºC

Therefore to reduce the uncertainties regarding the comparison between the two

modelling approaches, six LSTM-VMs and nine GRU-VMs were trained using the

same datasets for training and testing as well the same parameters used to tune the training process as shown in **Table 5.4**.

Table 5.4 LSTM and GRU VMs training parameters

Battery Datasets	Panasonic[189]
Training	Mix 1 to 4, HW, and US06
Testing	UDDS, LA92, NN
Temperatures	-10ºC, 0ºC, 10ºC, 25ºC
Number of epochs	~20000
Initial learning rate	0.01
Learning rate drop period	2000
Learning rate drop factor	0.85
Parameters	600*

*571 for LSTM-VM and 589 for GRU-VM

The extended comparison between the two models approach is shown in **Figure 5.7**, where an average of the results per drive cycles and temperatures is presented in **Figure 5.7**(a) showing that only in 2 out of 12 cases the GRU-VM presented better results than the LSTM-VM. **Figure 5.7**(b) and **Figure 5.7** (c) shows how the results are distributed for each trial in each drive cycle and temperature, therefore concluding that based on the same training conditions and dataset used in this work, the LSTM-VM approach presented lower error than what could be achieved by the GRU-VM approach, despite the larger number of trials.
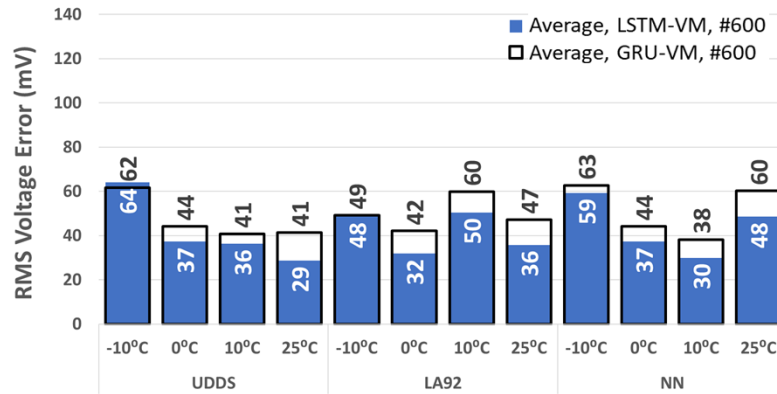
(a) Panasonic, LSTM-VM and GRU-VM
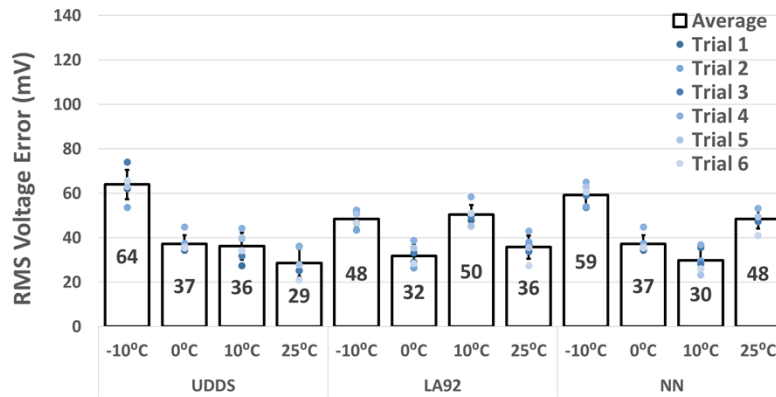
(b) Panasonic, LSTM-VM, 600 parameters
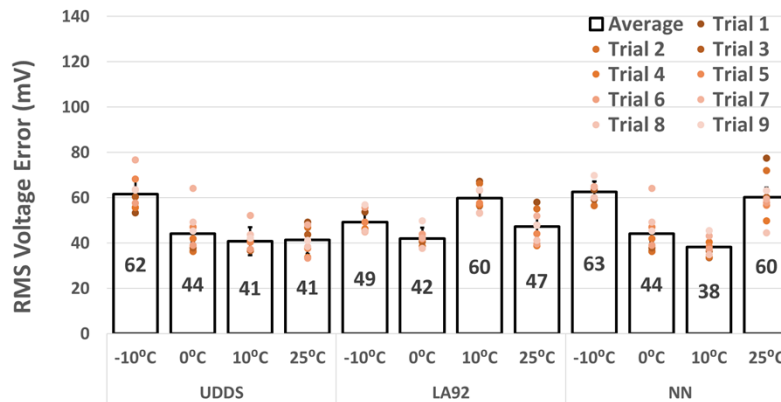
(c) Panasonic, GRU-VM, 600 parameters

Figure 5.7 Panasonic RMS voltage error for (a) average of results from LSTM-VM and GRU-VM, (b) trial results for LSTM-VM, and (c) for GRU-VM. Both models with 600 parameters and tested from -10ºC to 25ºC for each of three drive cycles (UDDS, LA92, and NN).

5.6. Concluding remarks

Three ECM approaches were presented in this chapter for two different Li-ion batteries datasets. The first approach is a third-order ECM with nonlinear resistance. The second and third models are based on two machine learning approaches using RNNs, the LSTM and GRU, respectively. The ECM is fitted based on the HPPC test data using quadratic programming, while the LSTM-VM and GRU-VM models were trained using different drive cycles data at different temperatures. For the Samsung T30, presented considerably better results than the ECM. Between the LSTM-VM and GRU-LSTM, for the Panasonic dataset, the difference also benefitted toward the LSTM-VM, maybe due to the extra gate and memory state embedded in its structure. For future work, a different structure of the GRU-VM can be able to match the LSTM-VM by stacking another GRU layer or fully connected layer.

6. POTENTIAL OF TRANSFER LEARNING FOR IMPROVED STATE-OF-CHARGE ESTIMATION WITH A RECURRENT NEURAL NETWORKS

6.1. Problem statement

The process of training machine learning algorithms is task-specific, though, so the algorithm must be trained with a substantial amount of data from each specific application. Furthermore, the data must cover as much as possible of the whole operating range, which will be required by the intended application. In the case of Li-ion modelling or Li-ion SOC estimation, the data may include, but are not limited to, time-domain measurements of voltage, current, temperature, and amphours over a wide range of temperature, state of charge, and current or power values. To create a sufficiently large battery dataset to train a NN for SOC estimation can, therefore, be a significant burden. This work proposes to reduce the necessary training data necessary for estimating the SOC of different types of Li-ion batteries. A model based on LSTM can be trained for one battery type with a "full" dataset, and then re-trained for a different battery type with a lesser amount of data and time using transfer learning (TL) [190], this is the first time TL has been used for a battery SOC estimation application.

6.2. xEV li-ion SOC estimation with LSTM

A model based on LSTM can "remember" past information, which makes this approach especially useful to solve problems that include long sequential data or time-series data, such as speech recognition and battery SOC, as shown in previous chapters. Up to the time of the publication of this study [23], LSTMs have been validated in the literature for SOC estimation of at least one battery type, a

156

Panasonic 18650PF Li-ion battery cell [137]. This work expanded on the prior art, to test LSTMs for additional battery types and to demonstrate transfer learning. The battery dataset necessary to train the LSTM has to be representative of the intended application, in this case, xEV. For this research, the batteries are tested with power profiles calculated for an electric vehicle performing the US06, UDDS, and LA92 industry-standard drive cycles. Four datasets were acquired from four different Li-ion batteries, a Panasonic 18650PF, LG HG2, Samsung 48G, and Samsung T30. Each dataset contains the measured cell voltage, current, battery temperature, and the amp-hours consumed from each battery. The batteries and dataset profiles are summarized in **Figure 6.1**, where each "Mix" drive cycle profile is created from a time-shifted mix of portions of the US06, HWFET, UDDS, LA92 profiles, and CC is a 1C constant-current, constant-voltage charging profile. All tests were performed in a thermal chamber set to 25⁰C, and the measured battery surface temperature increases beyond 25⁰C due to losses in the battery.

Table 6.1. Battery datasets specification

BATTERY	CAPACITY	FORMAT	TEST PROFILES
PANASONIC 18650PF (PANASONIC)	2.9 Ah	Cylindrical 18650	MIX (1-4), HW, UDDS, LA92, US06, CC
LG HG2 (LG_HG2)	3 Ah	Cylindrical 18650	Mix (1-8), UDDS, LA92, US06, CC
SAMSUNG 48G (SAM_48G)	4.8 Ah	Cylindrical 21700	Mix (1, 2, 6, 7, 8), UDDS, LA92, US06, CC
SAMSUNG T30 (SAM_T30)	3 Ah	Cylindrical 21700	Mix (1-8), UDDS, LA92, US06, CC

157

The NN learning process with one or more LSTM layers is very similar to that for other NN structures, and consists of four simplified steps: 1) feedforward the input data through the network with its learnable parameters, 2) compute the error based on the difference between the output (i.e. estimated SOC) and the desired target (i.e. measured SOC calculated from measured amp-hours), 3) backpropagate the error to update the network parameters using gradient descent, 4) repeat steps 2 and 3 until the error is less than the desired threshold or until other conditions are met such as exceeding a maximum iteration setpoint, e.g. max epochs. See **Figure 4.2**, a simplified view of the NN training and testing/validation process.
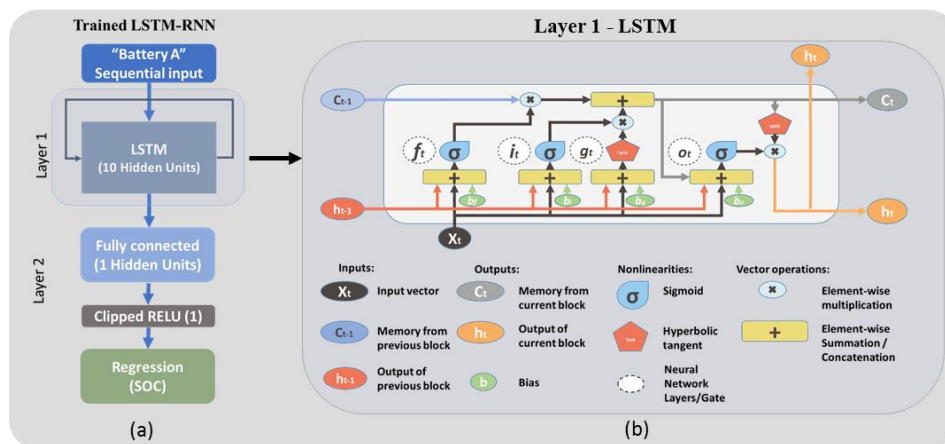
Figure 6.1 (a) LSTM structure for Li-ion SOC estimator, (b) Long short-term memory cell details

Figure 6.1(a) shows the full NN model structure used to estimate the SOC from a battery dataset, where Layer 1 is the LSTM layer with ten hidden units, and layer two is composed of a feedforward network structure, here referred as fully connected (FC). The total of learnable parameters for this model structure is 571, including weights and biases. The LSTM layer structure, as shown in **Figure 6.1(b)**,

where the LSTM layer is composed of input, output, and recurrent connections, each with its own set of learnable parameters, as well as a memory cell (Ct), and four gates responsible for regulating how much of the current information should be processed (it), pass through (gt) to be stored in the memory (Ct), passed forward to be used in the next time step (Ot), and which previously-stored information should be forgotten (ft)[191].

6.3. Li-ion SOC estimation using LSTM with transfer learning

Transfer learning is the transference of knowledge from a previously learned task to a new task. Transfer learning is performed for battery SOC estimation by training the NN model for one battery type and then training the model for another battery type using the previously trained network parameter values as a starting point. Some of the NN layer parameter values may also be "locked," preventing them from varying during the training process, or "unlocked," allowing them to vary and attain a new value during the training process.

Another definition of TL is presented in [192] where a Domain D is defined as a composition of a feature space $\mathcal{X}$ and a probability distribution $P(X)$, where $X=\{x\_1,...,x\_n\} \in X$, or for a specific domain, $D=\{X,P(X)\}$. Then for a given source domain D_S and a learning task T_S, a target domain D_T and learning task T_T, transfer learning aims to help improve the learning of the target predictive function $fT(.)$ in D_T using the knowledge from D_S and T_S, where $D\_S \neq D\_T$, or $T\_S \neq T\_T$., or $P\_S(X) \neq P\_T(X)$. As shown in **Table 6.2**, it is possible to classify TL into three types based on the relation of domains and tasks.

For this work, it is assumed that the feature space $\mathcal{X}$ and probability distribution *P(X)* of different types of Li-ion batteries are different but related to each other. Therefore, transductive transfer learning can be used in which the source and target data are different but related, and the source and target task (SOC estimation) are the same as described in **Table 6.2**.

Table 6.2. Characteristics of traditional machine learning and the three types of Transfer Learning

Learning settings		Source and Target Domains	Source and Target Tasks
Traditional ML Training		The same	The same
Transfer learning	**Inductive** or **Unsupervised**	The same	Different but related
		Different but related	Different but related
	Transductive	Different but related	The same

The differences between the Li-ion batteries used in this study are summarized in **Figure 6.2(a)** and **Figure 6.2(b)**.

(a)

160

(b)
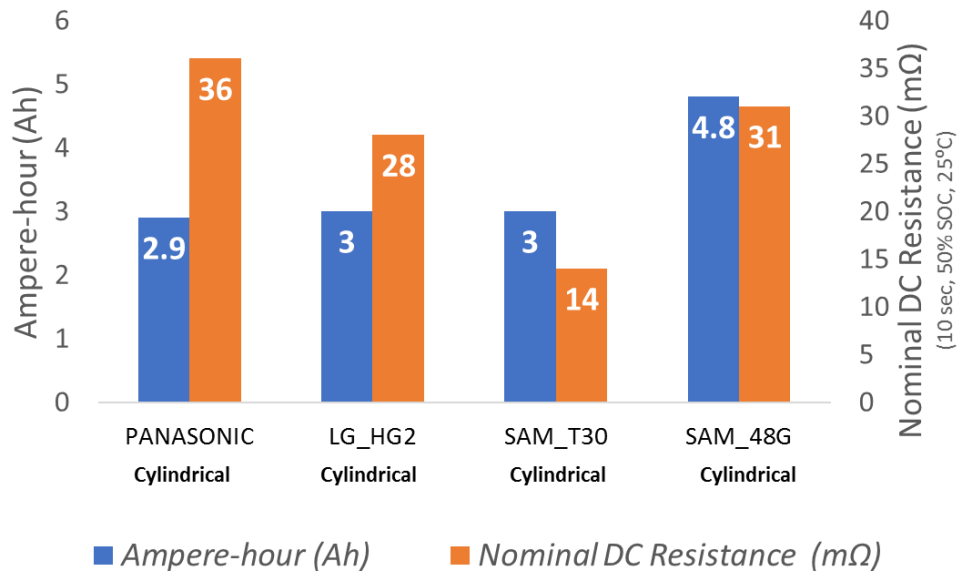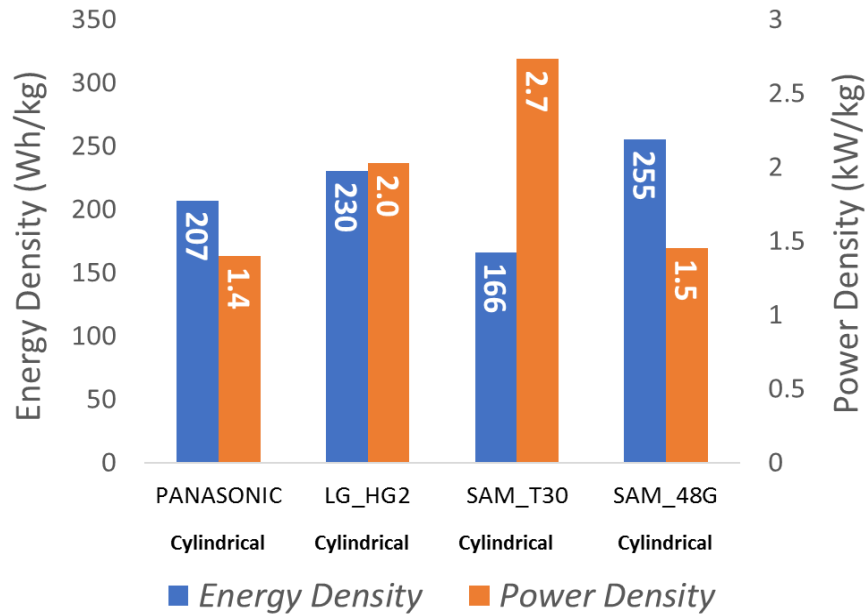
Figure 6.2 Characteristics of tested batteries (a) Nominal capacity and DC resistance at 50% SOC (b) Energy and power density

Through the use of transductive transfer learning, it is expected that during the retraining process, the neural network will initially have higher performance (lower error) and that it will reach lower with fewer training cycles and end up with an overall lower error, as is illustrated in **Figure 6.3**. This hypothesis will be tested in section 6.4, determining whether the expected benefits – reduced training time, computing power, and training dataset size can be achieved.

higher slope

higher asymptote

Performance

higher start

Training

	Without transfer learning
	With transfer learning
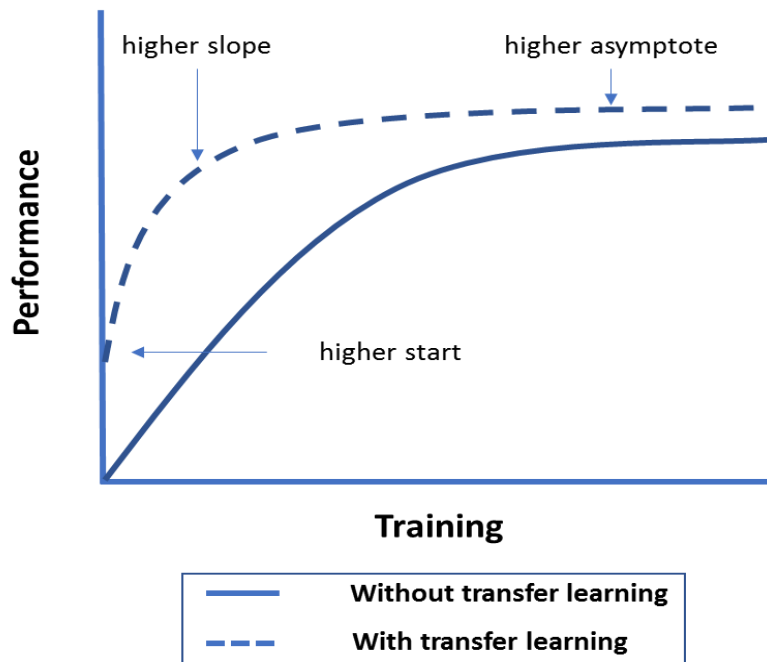
Figure 6.3 Example of neural network performance (SOC estimation accuracy) improvement achieved with transfer learning
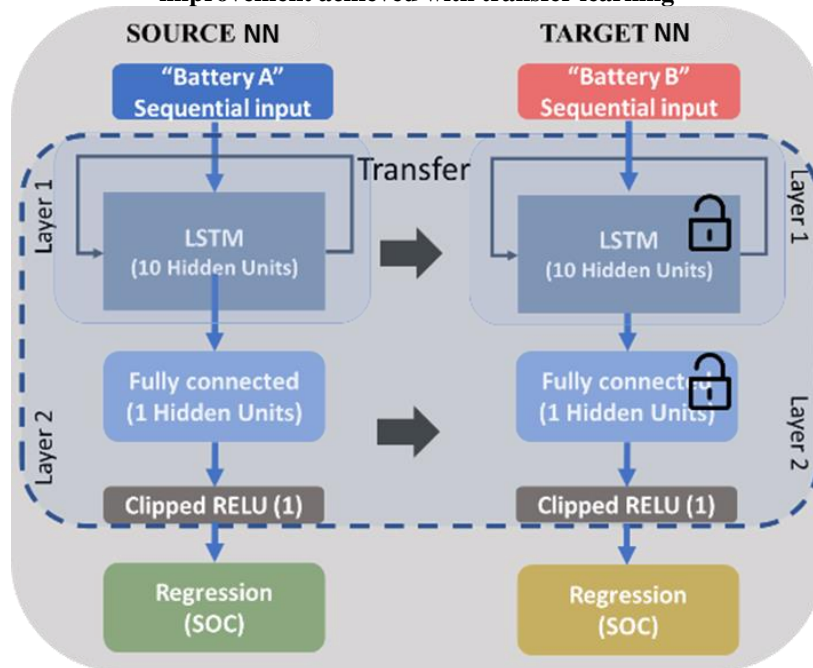
Figure 6.4 Transferring all learned parameters from Source NN to Target NN, leaving the parameters "unlocked" for the Target NN training process

The transfer learning approach implemented in this work is illustrated in **Figure 6.4**, where the source NN is initially trained with a "Battery A" dataset. The learned parameters in Layers 1 and 2 are then transferred to the Target NN. The parameters are updated when trained with a different "Battery B" dataset, which can be either a data of a different type of battery or just a reduced amount of data from the "Battery A" dataset.

6.4. Results and analysis

6.4.1. NN structure and training

As the focus of this work is to present the benefits of using transfer learning to improve the SOC estimation process, only one NN structure and one set of hyperparameters were selected and used for all cases, as shown in **Table 6.3**. The NN structure and hyperparameters do not necessarily achieve the highest accuracy and computational efficiency, but they allow for consistent comparison across all cases. The hyperparameters include the learning rate (LR), LR drop factor, LR drop period, as well as the maximum epochs for training, minibatch size, and optimizer type (ADAM). The battery data acquired and used as an input was battery terminal voltage (V), current (I), and battery temperature (T). The battery ampere-hours (Ah) calculated by the battery cycler during the data acquisition was used as a reference to calculate the SOC objective function during training.

The NN was implemented in Matlab version R2018b, which provides quick prototyping and intuitive design of NN structures, and trained using two graphical processing units (GPU), an NVIDIA Titan X Pascal and a GeForce GTX 1080 TI.

The schematic of the test bench and data logging system used to acquire the SAM_T30, SAM_48G, LGHG2 datasets is shown in **Figure 4.3**, the PANASONIC dataset is available in [189]

Table 6.3. NN structure and hyperparameters

NN Structure	Number of Parameters	Hyperparameters
Sequential Input (*V, I, T*)	-	• Initial LR: 0.01
LSTM (10 hidden units)	Input Weights = 120 Recurrent Weights = 400 Bias = 40	• LR drop factor: 0.5 • LR drop period: 100 • Max Epochs: 515
Fully Connected (1 hidden units)	Input Weights = 10 Bias = 1	• Optimizer: ADAM • Dataset normalized
Clipped RELU (clipped on 1)	-	
Regression output (SOC)	-	
	Total # of parameters: 571	

6.4.2. Experimental data collection and test cases

All of the battery datasets used in this work are listed in **Table 6.1** and were acquired using lab equipment like that in **Table 4.2** and the setup described in **Figure 4.3**. Before the NN training process, the battery test data was divided into Training and Test datasets. The Training datasets consist of all of the available Mixed drive cycles for each battery, as listed in **Table 6.1**, and the accompanying charges (CC) for each mixed drive cycle. The Test dataset is the UDDS, LA92, and US06 profiles and the corresponding charges (CC). The objective is to evaluate the SOC estimator's ability to correctly estimate the battery SOC when subjected to a dataset not used during training [19], so the estimator is always tested with the independent Test data.

The NN was then trained in four different ways. As a benchmark, the NN was trained without transfer learning using the full training dataset, as described in Case 1 of **Table 6.4**. For the other cases, the NN was initially trained with Source data from a different battery type, then its learned parameters transferred to another NN structure to be trained with the data from the Target battery, which will be used to estimate SOC. The neural network was trained with different combinations of Source and Target data to highlight the benefits of transfer learning for different cases, as described in Cases, 2-4 in **Table 6.4**. For cases 3 and 4, partial Training datasets consisting of cycles MIX 1-3 (1,2, & 6 for the Samsung 48G) were used to highlight the performance of the estimator when a smaller dataset is available.

6.4.3.   Case 1: Baseline SOC estimator with no transfer learning

The NN SOC estimator was first trained as a typical neural network would be, without transfer learning. The training was continued for 515 epochs, which took approximately 1 hour for each battery. Following the training, the Test dataset is input to the network and the RMSE, MAE, and Maximum error (Max) are determined. For this test case, RMSE of 1.9 to 3.5% and max error of 10.1 to 19.9% was observed, as shown in **Table 6.5**.

Table 6.4. NN SOC Estimator cases investigated

CASE	TRANSFER LEARNING	TRAINING DATASETS		TEST DATASET
		Source	Target	
1	No	FULL *One Cell Type*	-	UDDS, LA92, US06, CC
2	Yes	FULL *One Cell Type*	FULL	UDDS, LA92, US06, CC

3	Yes	FULL *One Cell Type*	PARTIAL (MIX 1-3)	UDDS, LA92, US06, CC
4	Yes	PARTIAL (MIX 1-3) *All Cell Types*	FULL	UDDS, LA92, US06, CC

Table 6.5. Baseline SOC results without Transfer Learning -Case 1

BATTERY	RMSE	MAE	MAX	TRAINING TIME
PANASONIC	2.6 %	2.2 %	10.1 %	1 hour
LG_HG2	1.9 %	1.3 %	13.1 %	1 hour
SAM_48G	3.5 %	2.5 %	19.9 %	1 hour
SAMT_30	2.3 %	1.6 %	14.3 %	1 hour

This error is rather high but is reasonable considering the small number of epochs and relatively simple training structure. For the remaining test cases, all of which use transfer learning, much lower error was observed, even when the network is trained with a partial dataset.

6.4.4. Performance of SOC Estimator with Transfer Learning

Three transfer learning cases were investigated to demonstrate the different ways in which transfer learning can be beneficial. Each case is described, and the results are summarized in the following subsections.

6.4.4.1. *Case 2: FULL source (one cell type) and FULL target datasets*

For Case 2, the networks for each of the four battery types from Case 1 were used as the *Source* network. Each network was then trained using transfer learning for the other three battery types. In total, twelve networks were trained, three for each battery type, covering all combinations of *Source* and *Target* datasets. The RMSE error for each test case was compared to the error for Case 1, **Table 6.5**, and then

plotted in **Figure 6.5** on the following page. The RMSE error for the networks trained with TL is lower for all but one case and is substantially less for many cases. For example, RMSE was reduced by 64% for the case where the network has initially been trained for the LG_HG2, then transfer learned to SAM_T30. Overall, this demonstrates that for the same number of epochs of training, more accurate SOC estimation will result when the network parameters have already been trained from another battery.

© 2020 IEEE
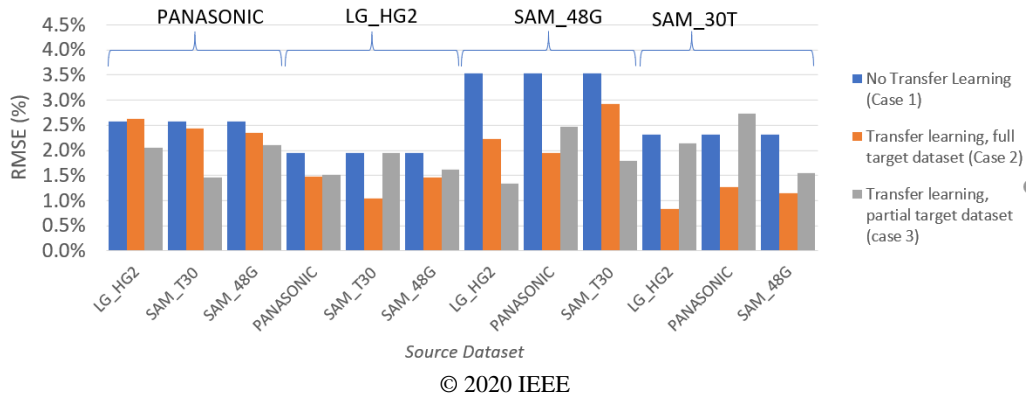
Figure 6.5 Transfer learning performance for FULL (Case 2) and PARTIAL (Case 3) target datasets

The observed and predicted SOC and SOC estimation error is also shown for the SAM_T30 battery in the time domain plot in **Figure 6.6**. The error is quite low (<4%) for both the drive cycles and the charging.

6.4.4.2. Case 3: FULL source (one cell type) and PARTIAL target datasets

To investigate what performance can be achieved with a lesser amount of training data, for Case 3, the network with TL was trained with Target data consisting of just three of the mixed drive cycles and accompanying charges. Improved accuracy

167

compared to the no transfer learning case was achieved for all but two of the training scenarios, as shown with the grey bars in **Figure 6.5**. This demonstrates that transfer learning does reduce the number of training cycles required needed to achieve good accuracy, confirming another hypothesis for the proposed transfer learning method.

6.4.4.3. *Case 4: Partial source (all cell types) and FULL target datasets*

For the prior two transfer learning cases (Case 2 & 3), the network was pre-trained with Source data from just one cell type. For this case, Case 4, the network is now pre-trained with partial Source data consisting of three mixed drive cycles from each of the four battery types.
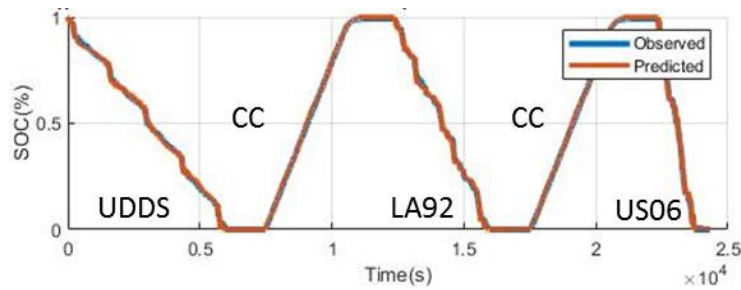
© 2020 IEEE
(a) Observed versus predicted SOC
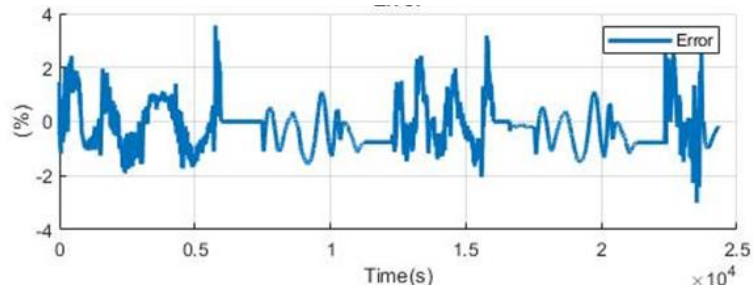
© 2020 IEEE
(b) SOC estimation error

Figure 6.6 Samsung T30 battery SOC estimation for Transfer Learning from LG HG2 source data (Case 2)

168

By using Source data from each battery type, the network is exposed to data from a range of battery types and the network parameters are therefore assumed to be a good starting point for the TL process. After training with TL for 515 epochs with the Target data, the SOC estimator performed better for each of the battery types, as shown in **Figure 6.7**. The normalized RMSE is between 53 %, and 96% of that achieved for the no TL case, and the improvement is in the same range achieved for the Cases 2 & 3. It is therefore clear that training the network with TL and data from multiple batteries is useful, but it is not necessarily more effective than training with data from a single battery type.
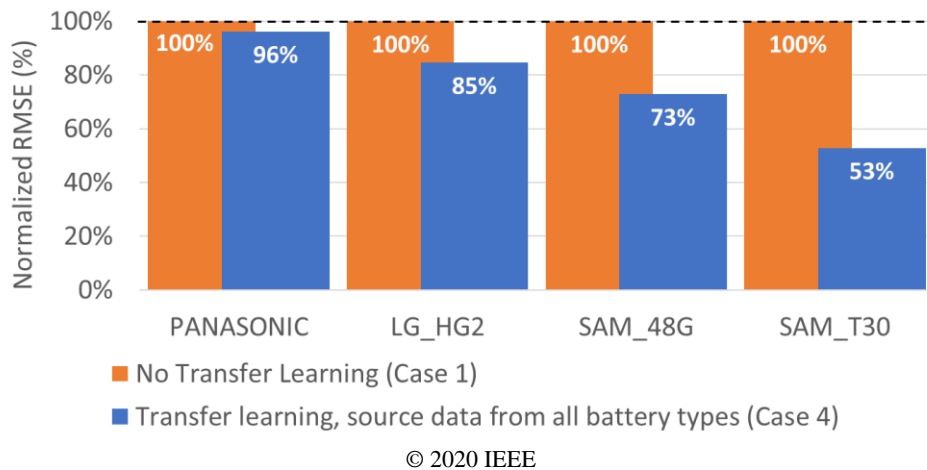
Figure 6.7 Transfer learning performance for source network trained with partial datasets from all battery types (Case 4)

6.4.5.   Transfer learning compared to no transfer learning with training for a greater number of epochs

It is common to train a neural network until the error asymptotes at a minimum value. For Cases 1-4, though, the network was trained for a fixed number of epochs (515), to allow for easy comparison of cases with the same number of training

iterations. For this last case, the network is instead trained without transfer learning for a large number of epochs (5100), so the error reaches a minimum value. The error achieved for 5100 epochs of training and no transfer learning is compared to the error achieved for 515 epochs of training with transfer learning in **Figure 6.8** for the Samsung T30 cell.
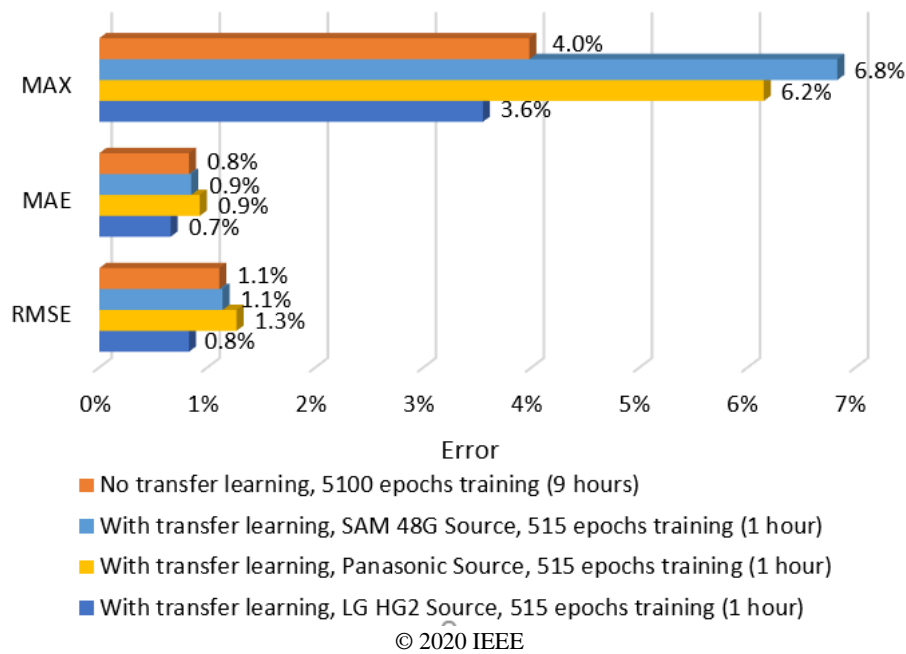
Figure 6.8 SOC estimation performance for Samsung T30 cell with 5100 epochs of training and with transfer learning (Case 2)

The MAX, MAE, and RMSE are less for one of the transfer learning cases and greater for the other two, this demonstrates there is potential for transfer learning to reduce training time and improve SOC estimation accuracy even when training is continued for a long period, but the result is dependent on the *Source* data. A more thorough analysis would be required to come to a definitive conclusion, taking into consideration the result variation due to the randomized initial NN parameter

values, which can lead to different local minima, therefore, especially for benchmarking purposes should be considered.

6.5. Concluding remarks

A NN using the LSTM structure was implemented to estimate the SOC of four different Li-ion battery types. The NN was first trained for each battery type of estimating SOC without transfer learning as a baseline case. Transfer learning, where the network is first trained with data from another battery type and then trained with data from the Target battery type, is then applied in several different ways to investigate the potential benefits. TL was shown to result in improved SOC estimation accuracy when the network is trained with both full and partial Target datasets (Case 2 & 3), demonstrating that not as much test data is required when transfer learning is used. The network was also first trained with Source data from all of the battery types, also resulting in improved estimation accuracy. Finally, it was shown that TL with 515 epochs of training could outperform 5100 epochs of training without TL, but the improvement was only observed for one of three tested cases. Overall, the chapter demonstrates the promise of transfer learning for reducing training time, improving SOC estimation accuracy, and decreasing the amount of required training data. For future work, the random parameter initial values effect discussed in sections 3.2.6 and 4.5, should be taken into consideration to reinforce the above conclusion.

7. COMPARATIVE ANALYSIS OF RECURRENT AND NON-RECURRENT DEEP NETWORKS FOR STATE-OF-CHARGE ESTIMATION OVER A WIDE TEMPERATURE RANGE

7.1. Introduction

As mentioned in previous chapters, the recent years increasing amount of data has been generated daily due to the technological advancements and commercial applications of connected devices coupled with the capacity to treat and create useful models and information using Artificial Intelligence have reshaped the world economy [7], [193]. In 2019 the daily amount of data generated by each connected vehicle was four terabytes, but the total amount of data from all sources is expected to be 44 zettabytes in 2020[16], which in turn forecasts to generate 750 billion dollars by 2030 [17]. Although this is only a small fraction when compared to the 15 trillion dollars that AI can add to the world economy by 2030[18]. Within this scenario, general-purpose technologies, such as AI, can be applied to solve many engineering problems, including SOC estimation. This chapter presents a comprehensive comparison between two potential deep learning approaches to solve SOC estimation for the increasing demand of electrified vehicles.

7.2. Deep neural networks for SOC estimation

This section presents the two methods used to perform xEV SOC estimation: FNN and LSTM based models. This chapter is organized by initially presenting the design choices followed by the models' final structures, and finalizing with the description of the framework used to train and compare the models. The basic concept of each of the modelling approaches discussed in this chapter was previously introduced in sections 3.2.1 and 3.2.5. The training stop condition for both LSTM and FNN used in this work is based on the Validation Patience or the

rate of improvement of the validation error; this will be discussed further in this chapter.

7.2.1. Feedforward neural network for xEV SOC estimation

To create an FNN-based model to estimate the xEV battery SOC, several configurations of the model structure were investigated and listed below. For each case configuration, the selection was based on the lowest RMSE, and each configuration was trained at least four times.

a) Four model configurations have been tested by varying the number of hidden layers l from 1 to 10, and the number of learnable parameters between 190, 600, and 2900. Based on the results presented in **Figure 7.1**, the selected configuration, in a dotted circle, was the one with two hidden layers and 600 parameters as it presented the lowest RMSE and in comparison to 1 hidden layer it shall have lower computational complexity due to lower number of layers with matching number of parameters [21]

b) Six different combinations of activation functions F have been tested using Tanh (3.3) and RELU (3.5) varying the number of hidden layers from l=1 to l=2, but all in cases maintaining the number of parameters at 600.

c) Differently from the LSTM models, the FNN does not have a memory cell embedded in the model showed to be extremely relevant for SOC estimation [13], [21], although a workaround is to create new model inputs using a moving average filter [21], [22] or a Butterworth filter. Both

options have been thoroughly tested, using equivalent filtering frequency (5.0m Hz and 0.5m Hz), but the option with the Butterworth filter presented considerable error reduction, as shown in **Figure 7.2**. The use of the Butterworth filters is one of the main contributions of this chapter.
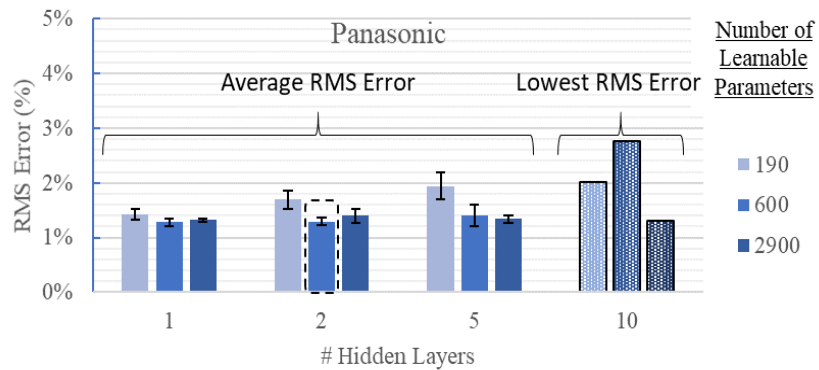
Figure 7.1 Number of hidden layers search for the FNN model structure. The dotted circle shows the selected two hidden layers with 600 parameters as the final model structure
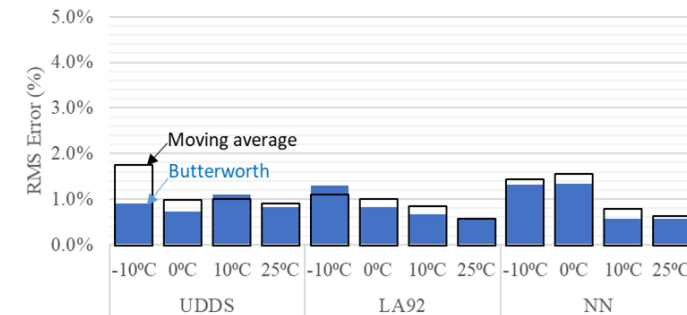
(a)
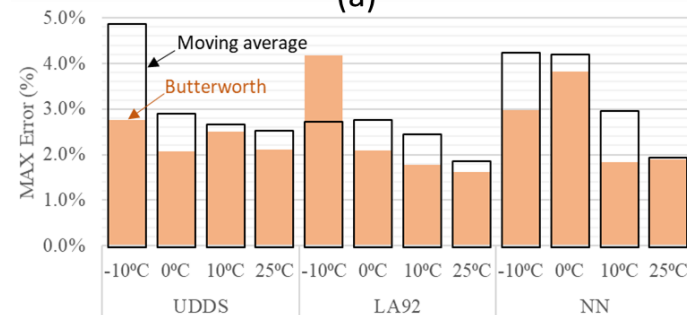
(b)

Figure 7.2 Comparison from the FNN using a Butterworth filter and moving average (a) RMS error (b) Maximum error.

The selected final FNN structure is shown in **Figure 7.3**, where the number of hidden layers selected is $l = 2$, based on the best RMSE using the Butterworth filters at 0.5m Hz and 5.0m Hz. The Butterworth filter frequencies were empirically selected by increasing from 0.2m Hz (500 seconds), similar to the moving average filter used in [22], to 0.5m Hz (2000 sec). The lower frequency can capture longer passed information, which turned to be relevant to improve the model accuracy. This led to assume that by replacing the transient voltage and current inputs by higher frequency filtered input, 5.0m Hz, could as well improve the model accuracy to capture shorter passed information.

Therefore, the final FNN inputs are represented by $\Psi_k = \{T_k, V_{(0.5mHz)k}, I_{(0.5mHz)k}, V_{(5mHz)k}, I_{(5mHz)k}\}$, where T_k is the battery temperature, $V_{(50mHz)k}$ and $V_{(5mHz)k}$ terminal voltage filtered at 0.5m Hz and 5.0m Hz respectively, $I_{(50mHz)k}$ and $I_{(5mHz)k}$ the battery current filtered at 0.5m Hz and 5.0m Hz, respectively. Using Butterworth filters has significantly improved the accuracy of the FNN, as shown in **Figure 7.2** and will be further discussed in section 7.5. Finally, the activation function selected was RELU (3.5) in all hidden layers.
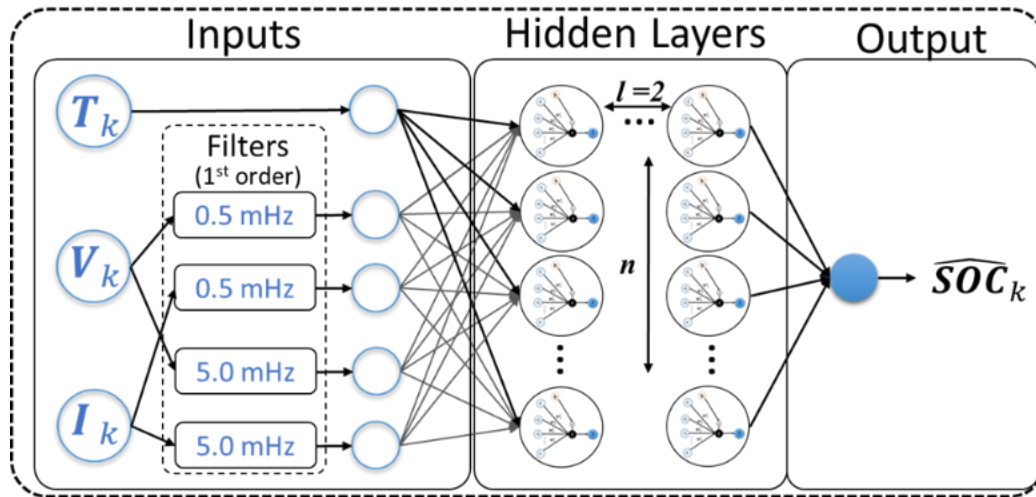
Figure 7.3 FNN model structure for xEV SOC estimation

7.2.2.　Long short-term memory recurrent neural network for

xEV SOC estimation

The use of RNN model with LSTM (LSTM-RNN), including some variations, has

shown promising results [22], [23], [137], [140] when applied to xEV SOC

estimation, being able to maintain good accuracy even at negative temperatures,

which impose more difficulty for the model [9]. Another benefit provided by the

LSTM-based models is its internal states, which give the model the ability to better

cope with sudden inputs variations or interruptions. Later in this chapter, it will be

further detailed and demonstrated in some examples.
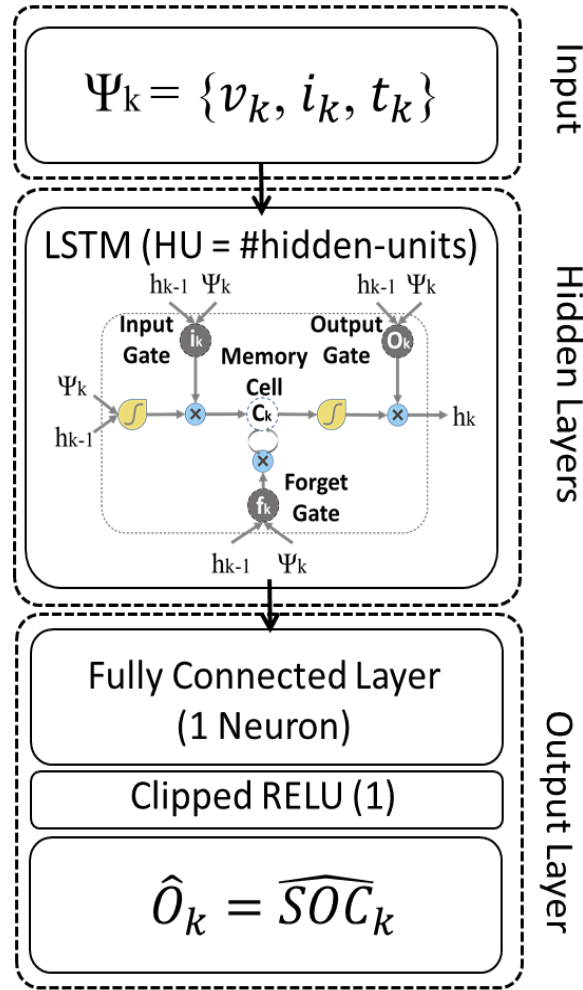
Figure 7.4 LSTM-RNN Structure for xEV SOC estimation, formed by one LSTM layer with N numbers of hidden-units, the input the matrix $\Psi_k = \{V_k, I_k, T_k\}$, where V_k is the battery terminal voltage, I_k the current, and T_k the battery temperature. The model output is the estimated SOC represented by $\widehat{SOC}_k$ at timestep k.

To estimate the SOC from a Li-ion battery dataset, the LSTM-RNN-based model use as input the matrix $\Psi_k = \{V_k, I_k, T_k\}$, where V_k is the battery terminal voltage, I_k the current, and T_k the battery temperature. The model output is the estimated SOC represented by $\widehat{SOC}_k$ at timestep k. shows the LSTM-RNN structure used in this work to estimate the battery SOC. The number of hidden-units, HU, also showed in **Figure 7.4**, represents the number of neurons in each

gate of the LSTM layer, which in turn is equivalent to the length of the weight vectors used in each gate, e.g. if HU equal do ten and $\Psi_k = \{V_k, I_k, T_k\}$, it means that W_i, the input weight vector from (3.12), has dimension (3x10).

The total number of parameters refers to the total number of weights and biases considered within all the models' structures, and it will help to compose the comparison baseline between LSTM-RNN and FNN models through the rest of the chapter.

7.3. Neural network training framework

To have a consistent comparison framework, the same set of parameters and resources listed in **Table 7.1** have been used to train both LSTM-RNN and FNN models. Despite listed in **Table 7.1**, the relationship between some of the parameters may require further explanation about its roles in the training process. For example, when setting the learning rate (LR) to 0.01, its value will change incrementally by multiplying by the Learning rate drop factor, 0.85, at every Learning rate drop period, 2000 epochs, until the end of the training process. Another relevant information regards to the Validation Patience parameter, 12300 Epochs, which links the training stop condition to the number of validation error checks that shows no error reduction, e.g. if at epoch 1000 the validation RMSE is 0.90% the training process will continue and automatically stop at epoch 13300 if the validation error does not get lower than 0.90%. Therefore, the only condition to stop the training process is if the validation error stops decreasing for as long as the Validation Patience permits.

TABLE 7.1 Neural Networks training baseline characteristics

Initial learning rate	0.01
Learning rate drop period	2000 Epochs
Learning rate drop factor	0.85
Loss function optimizer	ADAM
Number of Minibatches	1
Validation Patience	12300 Epochs
Number of Parameters	Vary from 20 up to 2900
Training repetition	Minimum of 4 times
Software platform	Matlab 2019b
GPUs	NVIDIA Titan X Pascal and GeForce GTX 1080 TI
CPU	Intel Core i7-3960 CPU@3.30GHz

Each training session is repeated at least four times to consider a possible variation of the results due to different local minima or saddle points [13], [194], [195]. The selection of the initial values of the weights and bias are randomly distributed using the Glorot initializer [196] at the start of every training session, which can lead to different local minima, as mentioned above.

7.4. Batteries and datasets

The datasets of two considerably distinct Li-ion batteries, Panasonic and Turnigy, have been chosen to train and validate several FNN and LSTM-RNN models to estimate the batteries' SOC. As presented in **Table 7.2**, the Panasonic has higher energy density than the Turnigy, although Turnigy has four times the specific power of the Panasonic, which is also reflected in the batteries' normalized resistance. The intention of using these two batteries is to intrinsically test the capabilities of the two modelling approaches to perform on very different batteries.

Table 7.2 Li-ion batteries characteristics

Battery	Panasonic	Turnigy
Model	18650PF	Graphene 65C
Format	Cylindrical	Pouch
Chemistry	NCA	NCA*or NMC*
Rated Capacity	2.9 Ah	5.0 Ah
Normalized Resistance	104 mΩAh	14 mΩAh
Specific Power	1.7 kW/kg	7.3 kW/kg
Specific Energy	207 Wh/kg	134 Wh/kg
Energy Density	577 Wh/l	329 Wh/l

*This is was not informed by the manufacturer, but an assumption made by the authors

The batterie's datasets were acquired using the lab equipment presented in **Table 7.3** following a series of data profiles calculated from an xEV, including automotive standard drive cycles UDDS, US06, LA92, HW. Each battery was placed in a climate chamber where the ambient temperature was varied from -10ºC to 25ºC, and the voltage, current, battery temperature, and Ampere-hour were logged at 10 Hz. These data were then cleaned, concatenated and normalized following the sequence from which the data were acquired. Then the data were split into Training and Testing datasets. The testing dataset is not used to update the weights and biases; therefore, it is used to validate the models' capability to generalize, hence been able to perform well when submitted to unknown data. All the results presented in this work are based on the error calculated from the Testing dataset. The test and training data points distribution for both batteries used in this chapter is similar to the LG_HG2 dataset, presented in **Figure 4.4**, where the test dataset accounts for approximately one-third of all the data available.

Table 7.3 Battery datasets and lab equipment

Battery Datasets	Panasonic	Turnigy
Training	Mix 1 to 4, HW, and US06	Mix 1 to 8, US06
Testing	UDDS, LA92, NN	UDDS, HW, LA92
Temperatures	-10⁰C, 0⁰C, 10⁰C, 25⁰C	-10⁰C, 0⁰C, 10⁰C, 25⁰C
Cycler manufacturer	Digatron firing circuits	Digatron firing circuits
Test channel	25 A, 0–18 V channel	75 A, 0–5 V channel
Data acquisition	10 Hz	10 Hz
Accuracy	±0.1% full scale	±0.1% full scale
Thermal chamber	Cincinatti subzero ZP8	Envirotronics
Size	8 cu. Ft.	8 cu. Ft.
Accuracy	-	±0.5 ◦C

7.5. Results and analysis

Several hundreds of FNN and LSTM-RNN models have been trained and tested using both Panasonic and Turnigy datasets, which in turn have required thousands of uninterrupted hours of computing resources. The most relevant results are presented in this section to support the following analysis and conclusions.

The LSTM-RNN has an inherent advantage in comparison to the FNN due to its capability to take contextual data to estimate its output, which makes it a compelling choice for speech recognition and natural language processing [110]. This capability is directly related to its memory cell and LSTM layer internal gated configuration, which enables the use of data directly measured from the battery into the model showing high SOC estimation accuracy even when exposed to negative temperatures. To match the accuracy provided by the LSTM-RNN, a large portion of the effort to produce the results presented in this section was directed to the improvement of the FNN model, as described in previous sections.
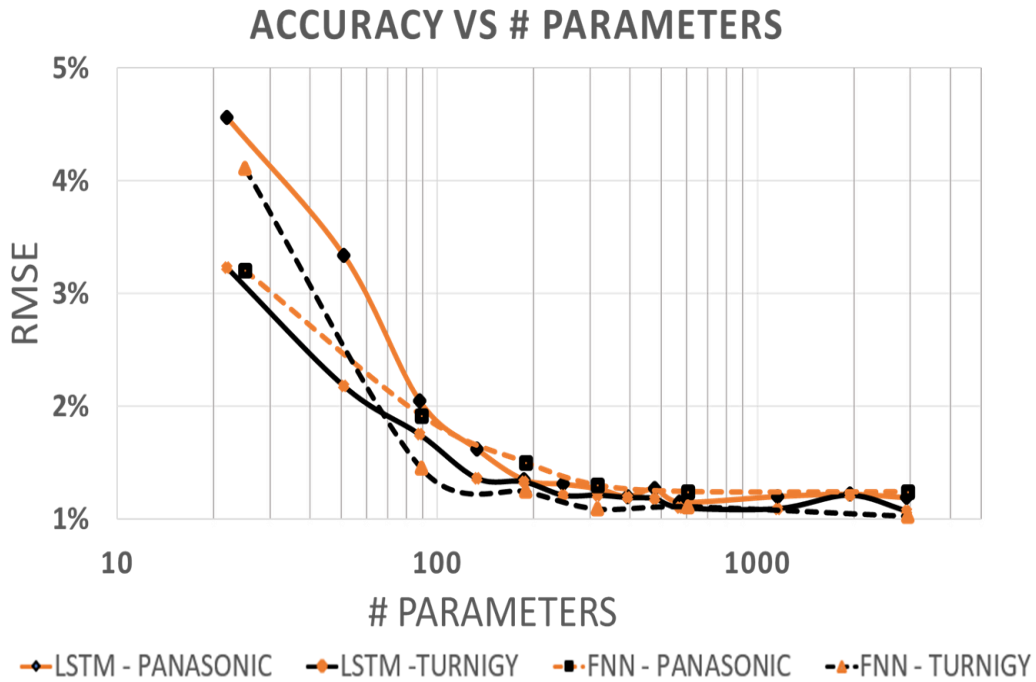
Figure 7.5 FNN and LSTM model accuracy versus the total number of parameters. The accuracy is calculated based on the validation dataset average RMS Error.

After establishing the final structure of the FNN and LSTM-RNN presented in

Figure 7.3 and **Figure 7.4**, each model was trained at least four times by varying

the total number of parameters from 20 to 2900 to understand the influence of

widening the model with more learnable parameters. **Figure 7.5** shows the trend of

accuracy versus the number of parameters in a logarithmic scale. The accuracy is

calculated based on the average RMSE of the validation dataset SOC estimation. It

is possible to observe that the improvement of accuracy has a diminishing return as

the number of parameters increases. The accuracy of the models with 600

parameters and 2900 are similar.
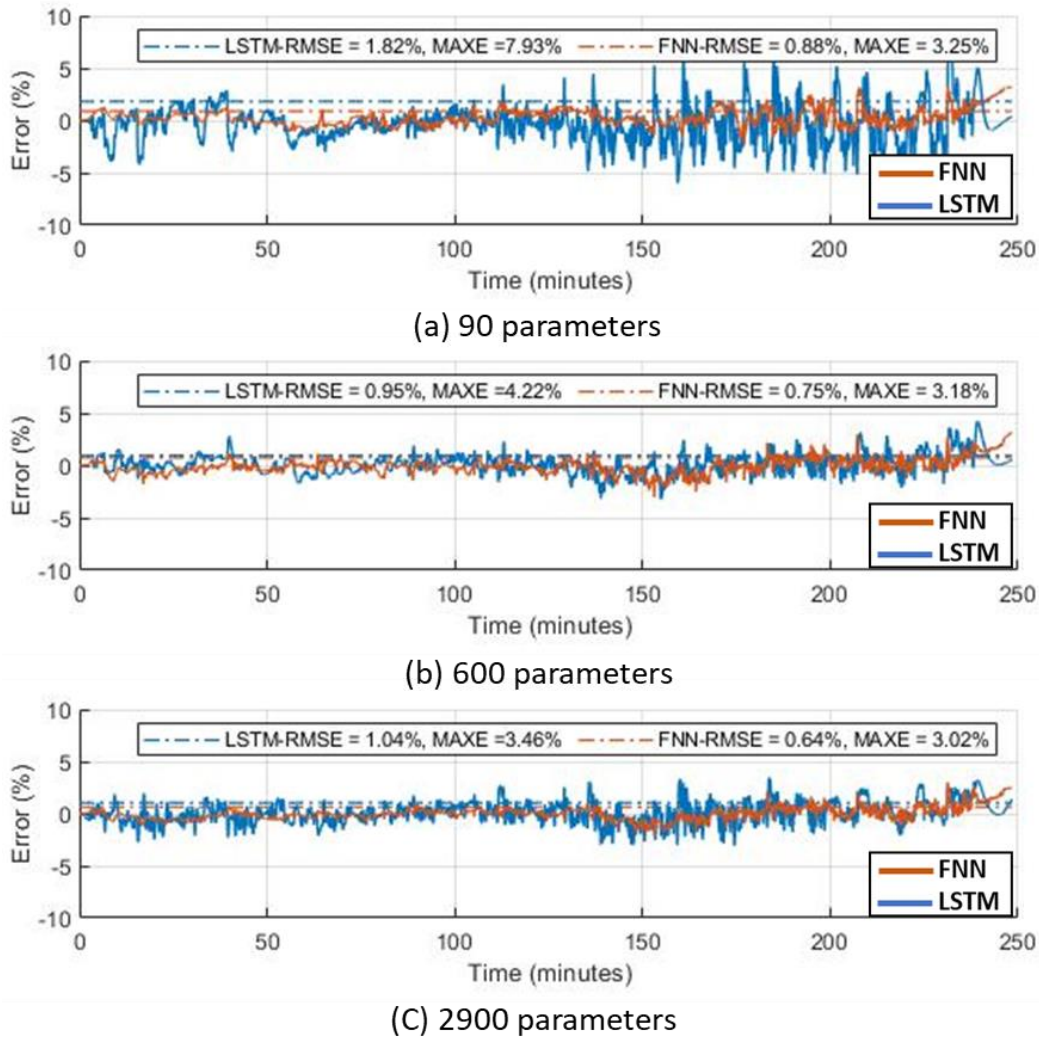
Figure 7.6 FNN and LSTM-RNN Errors plots from Turnigy LA92 at -10⁰C with (a) 90, (b) 600, and (c) 2900 parameters.

Figure 7.6 shows RMSE results from FNN, and LSTM-RNN SOC estimation case, picked from the Turnigy LA92 at -10⁰C with 90, 600, and 2900 parameters. For both FNN and LSTM-RNN, the increase in the number of parameters shows diminishing returns, especially for the FNN. The training and testing framework established and presented in section 7.3 has been used to compute the results presented in **Figure 7.7**, where it shows the result of each trial and the averaged

result, using the case with 600 parameters. Each trial shown in **Figure 7.7** represents a model trained. The results variation between trials was introduced in sections 3.2.6 and 4.5. Although in this chapter, a more significant number of models were trained to compose the results and discussion.

The results presented in **Figure 7.8** and **Figure 7.9**, shows a clear advantage for the FNN concerning the LSTM-RNN in most cases, although, at lower temperatures, the difference is reduced or in the case showed in **Figure 7.8(c)** at -10ºC and with 2900 parameters the LSTM-RNN presented slightly better accuracy. The LSTM performed slightly better than the FNN when the temperature suddenly varied from 0ºC to 25ºC as shown in **Figure 7.8(b)** and **Figure 7.8(d)**, as well as in **Figure 7.9(b)** and **Figure 7.9**(d). **Figure 7.10** shows the temperature variation overtime for both Turnigy HW and LA92.
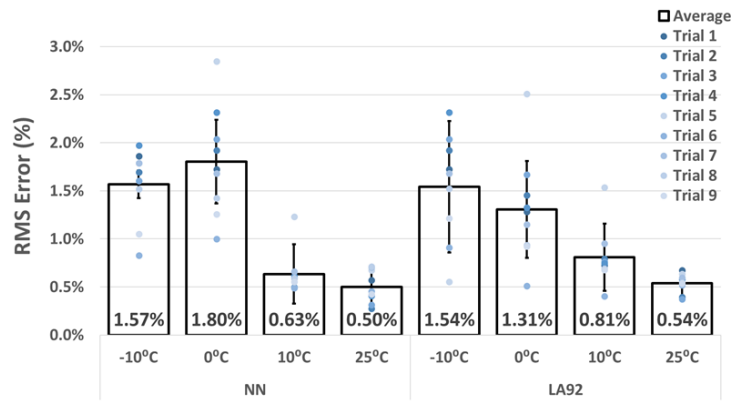
(a) Panasonic, FNN, 600 parameters

(b) Tunigy, FNN, 600 parameters
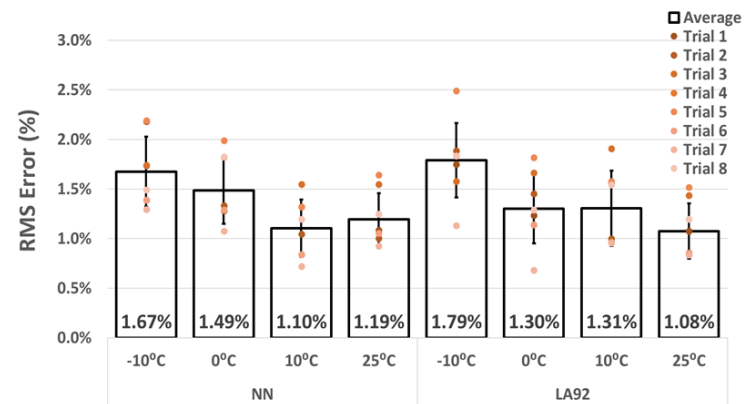
(c) Panasonic, LSTM, 600 parameters
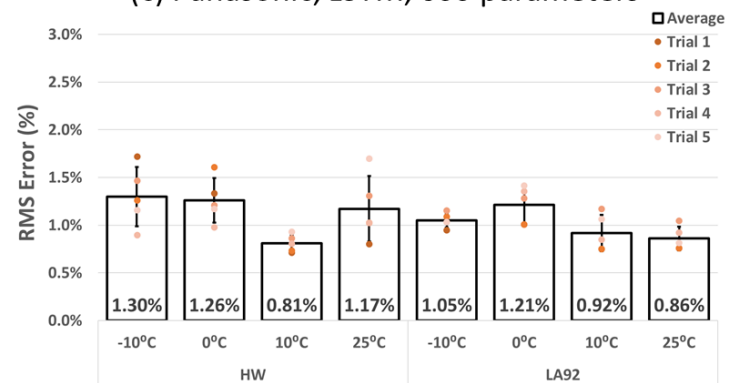
(d) Tunigy, LSTM, 600 parameters

Figure 7.7 FNN and LSTM model results by trials and averaged result, with 600 parameters
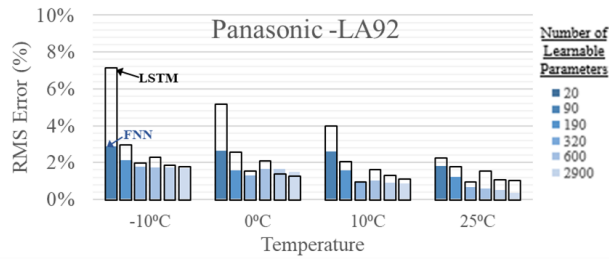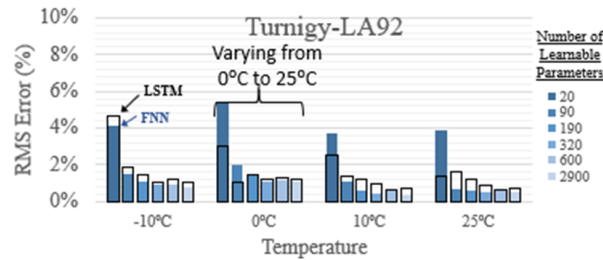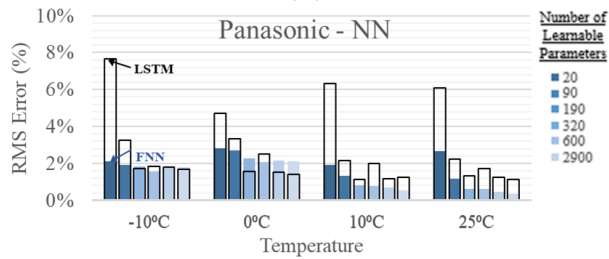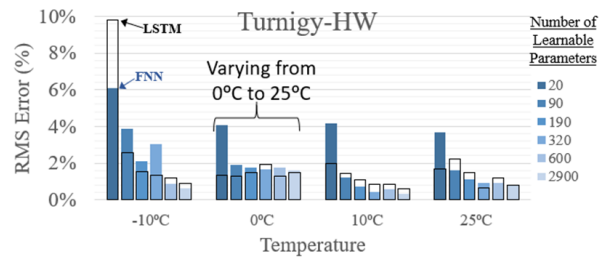
Figure 7.8 LSTM versus FNN Results based on the average RMS error SOC estimation results, varying from 20 to 2900 total parameters (a) Panasonic, LA92, (b) Turnigy LA92, (c) Panasonic NN, and (d) Turnigy HW. At 0ºC from all Turnigy results, (b) and(d), the temperature varied from 0ºC to 25ºC
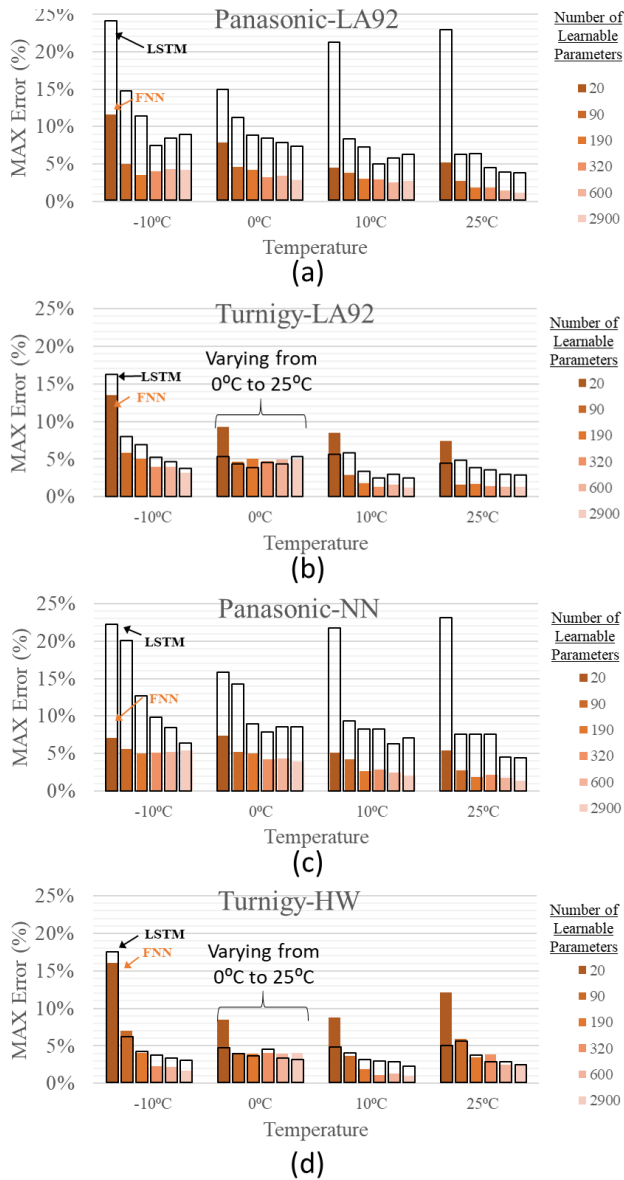
Figure 7.9 LSTM versus FNN Results based on the average Max error SOC estimation results, varying from 20 to 2900 total parameters (a) Panasonic, LA92, (b) Turnigy LA92, (c) Panasonic NN, and (d) Turnigy HW. At 0ºC from all Turnigy results, (b) and(d), the temperature varied from 0ºC to 25ºC
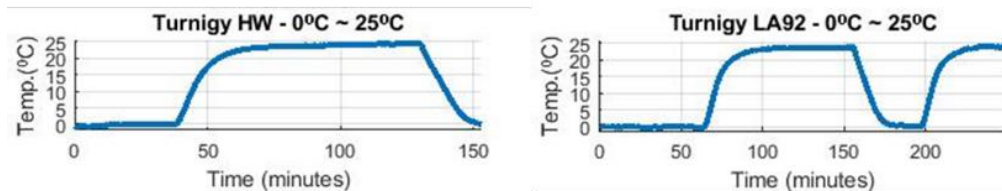
Figure 7.10 Turnigy LA92 and HW battery temperature varying from 0ºC to 25ºC over time.

Another particular situation where the LSTM has performed better than the FNN is shown in **Figure 7.11** where both models had to deal with a dataset that contains no contextual or previous information. This case has the intended to simulate a hypothetical situation where the models have to estimate the xEV SOC estimation despite eventual data flow interruptions. The situation is presented using the Turnigy UDDS dataset at -10ºC and tested on both FNN and LSTM-RNN with 2900 parameters. The hidden states of the LSTM-RNN, including the memory states, were set to zero before testing with the UDDS dataset. The LSTM-RNN only took 12 seconds to fit the observed SOC curve, while the FNN took approximately 12 minutes to reach an estimation value equivalent to the LSTM_RNN. The initialization without previous information damage the accuracy of both models, but considerably more in the case of the FNN.
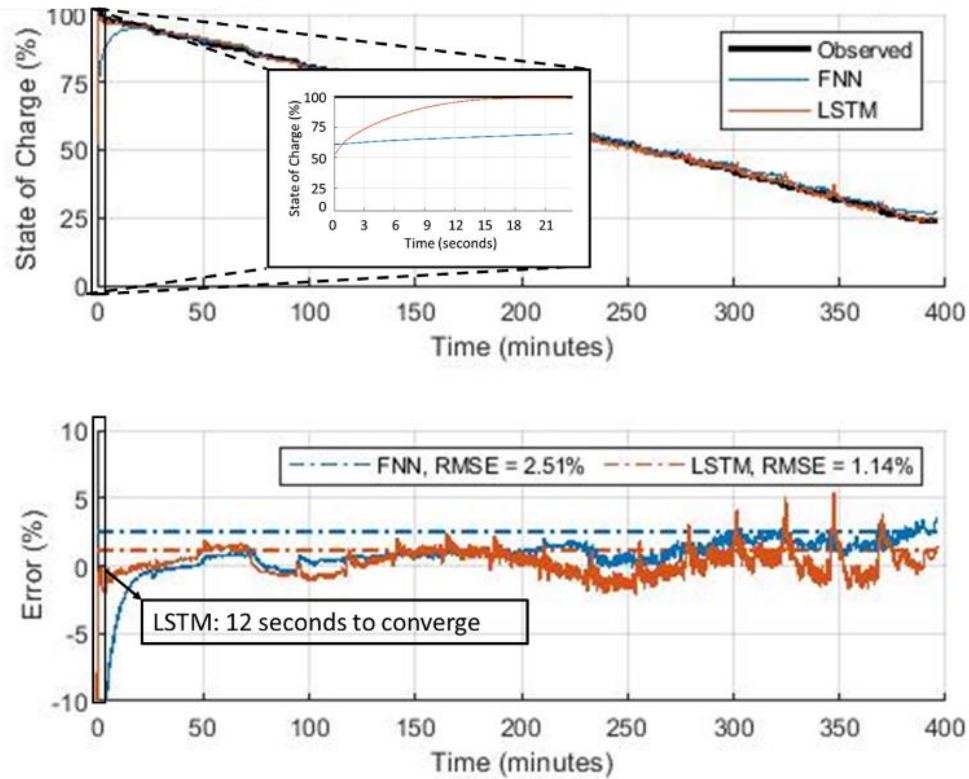
Figure 7.11 SOC estimation on Turnigy UDDS at -10ºC without previous data or updating LSTM hidden states. LSTM takes about 12 seconds to fit the observed SOC curve, while FNN takes several minutes

Figure 7.12 shows selected cases picked from the results of the LA92 at 25ºC and

-10ºC with 2900 parameters from both Panasonic and Turnigy datasets. Although

the RMSEs presented from both models are not significantly different from each

other, it is noticeable a higher error variation presented by the LSTM-RNN in all

cases. We assume that the FNN models can better cope with relatively slow changes

within the input and thus present a smoother and better SOC estimation than the

LSTM-RNN.
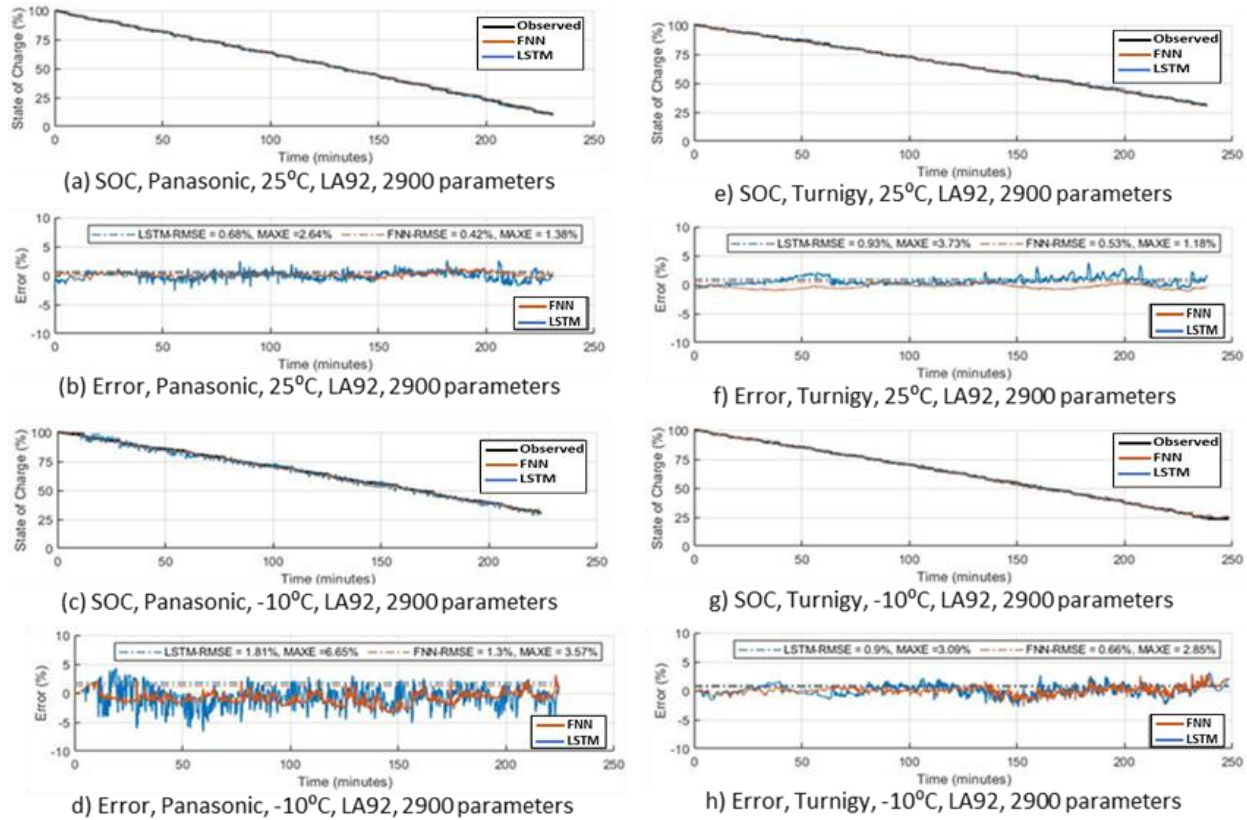
Figure 7.12 The time-domain plot of both FNN and LSTM-RNN from the LA92 drive cycle, including RMS and Max errors. In this case, all the models have 2900 parameters where (a) shows the SOC estimation and (b) the error plot for the Panasonic at 25⁰C while (c) and (d) at -10⁰C, (e) shows the SOC estimation and (f) the error plot for the Turnigy at 25⁰C, while (g), and (h) at -10⁰C. The dashed lines in (b), (d), (f), and (h) help visualize graphically the RMS error difference between the FNN and LSTM-RNN as well in relation to zero error.

Table 7.4 presents a comparison based on the best results obtained by the LSTM-RNN and FNN models with 600 parameters. The results are shown based on the concatenated drive cycles composed by UDDS, LA92, NN, and CC for all temperatures and by each temperature case.

As presented in section 7.2.1, the low frequencies used for the Butterworth filters have provided for the FNN the capability to better cope with long-term passed information as the LSTM-RNN model. The use filters before the model input to create "memory" capability to the FNN creates more flexibility and opens the possibility to add more filters with other frequencies to improve the FNN response to transient and short-term situations or to better adapt to different problems besides SOC estimation, e.g. SOH estimation.
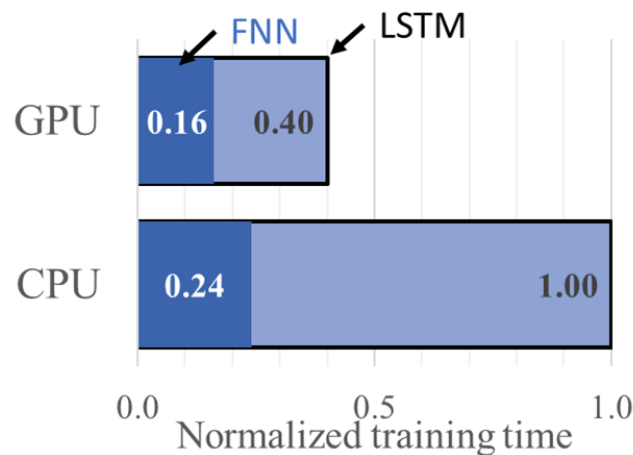
Figure 7.13 Normalized training time based on FNN and LSTM trained for 50000 Epochs, using CPU* and GPU*

*CPU: Intel Core i7-3960@3.30GHz; GPU: NVIDIA GeForceGTX 1080 TI

Table 7.4 Comparison of the SOC estimation methods

Li-ion Battery	Model[+]	Inputs(ψ) / Output ($\hat{o}$)	Test dataset	Best model Result[++++]	Model result by temperature
Panasonic NCR18650PF	**FNN**[++]	$\psi = [T_{(k)}, V_{0.5mHz(k)}, I_{0.5mHz(k)}, V_{5.0mHz(k)}, I_{5.0Hz(k)}]$; $\hat{o} = [SOC_{(k)}]$	UDDS, LA92, HW, CC	RMSE: 1.14%@-10^{0}C to 25^{0}C MAE: 0.73%@-10^{0}C to 25^{0}C MAX: 3.21%@-10^{0}C to 25^{0}C	0.98%@-10°C 1.17%@0°C 1.10%@10°C 1.30%@25°C
	LSTM	$\psi = [V_{(k)}, I_{(k)}, T_{(k)}]$; $\hat{o} = [SOC_{(k)}]$	UDDS, LA92, NN, CC	RMSE: 1.15%@-10^{0}C to 25^{0}C MAE: 0.80%@-10^{0}C to 25^{0}C MAX: 6.58%@-10^{0}C to 25^{0}C	1.27%@-10°C 1.18%@0°C 1.04%@10°C 1.11%@25°C
Turnigy Graphene 65C	**FNN**[++]	$\psi = [T_{(k)}, V_{0.5mHz(k)}, I_{0.5mHz(k)}, V_{5.0mHz(k)}, I_{5.0mHz(k)}]$; $\hat{o} = [SOC_{(k)}]$	UDDS, LA92, HW, CC	RMSE: 1.11%@-10^{0}C to 25^{0}C MAE: 0.79%@-10^{0}C to 25^{0}C MAX: 3.57%@-10^{0}C to 25^{0}C	1.16%@-10°C 1.47%@0°C[+++] 0.83%@10°C 0.82%@25°C
	LSTM	$\psi = [V_{(k)}, I_{(k)}, T_{(k)}]$; $\hat{o} = [SOC_{(k)}]$	UDDS, LA92, NN, CC	RMSE: 1.20%@-10^{0}C to 25^{0}C MAE: 0.74%@-10^{0}C to 25^{0}C MAX: 3.03%@-10^{0}C to 25^{0}C	1.01%@-10°C 1.01%@0°C[+++] 1.06%@10°C 1.33%@25°C

[+] **Models with 600 parameters.**
[++] **FNN with 2 hidden layers.**
[+++] **Temperature vary from 0ºC to 25ºC.**
[++++] **RMSE**

7.6. Concluding remarks

Based on the results presented in the previous sections, both models, FNN and LSTM-RNN, have shown excellent accuracy to estimate xEV SOC on both Panasonic and Turnigy even at negative temperatures, where the conditions are more complicated than at 25ºC [9]. However, the FNN model has performed considerably better than the LSTM-RNN, except when sudden variations on the temperature or the data flow interruption, the LSTM-RNN has performed better, being able to adapt quickly to the changes.

For future work, the inclusion of different filter frequencies, e.g. 125m Hz, may improve the response of the FNN for transient or short-term variations. The use of external filters creates more flexibility to improve the FNN models and adjustable to solve problems outside the SOC estimation, e.g. SOH estimation. The same idea could be added to LSTM models. The investigation of the effects of ageing on the battery SOC estimation. Consider the robustness comparison between both models, using similar procedures used in section 4.7.1 as well as computational complexity and real-time performance in a Hardware-in-the-loop or BMS.

8. CONCLUSION, FUTURE RESEARCH AND PUBLICATIONS

8.1. Concluding remarks

The transportation industry faces many challenges to improve efficiency, expand performance, advance connectivity, increase autonomy, and reduce emissions. Although, due to the uncertainties generated by the COVID-19 pandemic, any predictions at this point could be primarily affected, despite that, market signals have been indicating a favourable trend toward investments on renewable energy and electrified transportation sectors [4]. The increase of electrified vehicles in the transportation market share may also increase the amount of data generated from the streets

In 2019 the daily amount of data generated by each connected vehicle was four terabytes, which in turn, as the market increases, forecasts to generate 750 billion dollars by 2030 [17], this is only a small fraction when compared to the 15 trillion dollars that AI can add to the world economy by 2030[18]. Within this scenario, general-purpose technologies, such as AI, trained and greatly improved by data, can be applied to solve many engineering problems. As battery technology grows and matures, a significant amount of data is being collected and analyzed in a partially or fully automated fashion [19] to improve battery design and usage. This plethora of data has made it possible to improve BMS performance [20] via big data, IoT, cloud computing, and the AI methods developed and investigated in this thesis.

The SOC estimation determines how much energy it is available in the vehicle battery and has a significant impact on the vehicle EMS, including range

estimation, overall efficiency. It is crucial to estimate the vehicle battery SOC correctly, and still a challenge that the industry has to overcome [9], [10]. As extensively discussed in section 2.4, this is especially challenging at low-temperature conditions, therefore relevant for vehicles utilized in countries like Canada, that traditionally have freezing winters, and can have over 100 days per year with temperatures below 0℃ [11], [12]; but can reach temperatures as low as -41℃ [12] as shown on data collected from colder cities, such as Trois Rivieres in the province of Quebec in Canada.

In the case of SOC and SOH estimation based on AI methods, the main computational load demanded by these approaches happens during its off-line training phase as demonstrated throughout the thesis chapters, which also opens the possibility to be trained in the Cloud and downloaded to the vehicle using supporting communication infrastructure, e.g. 5G. The concept of Transfer Learning applied to SOC estimation, presented and discussed in chapter 6, can be particularly useful for this scenario of continuous updatable model based on the accumulation of real-world driving data as it may reduce the computational effort necessary to do the update.

For SOC estimation, several models configurations and approaches were developed and tested as results of this work, including different non-recurrent neural Networks, such as FNN and RNN based on LSTM. The approaches have considerably improved the accuracy presented in the previous state-of-the-art. This work has expanded the application throughout five different Li-ion at a wide

temperature range, achieving accuracies as low as 0.66% Root Mean Square Error at -10⁰C using an FNN approach and 0.90% using LSTM-RNN as shown **in Figure 7.12**. Through chapter 7, a detailed design process aimed to improve the FNN approach to match or surpass the LSTM-RNN is presented. The process includes the selection of the number of parameters, hidden layers and type of external filter used to compose the final structure of the FNN model, **Figure 7.12**, which by the end has outperformed the LSTM-RNN approach accuracy in several situations as summarized in **Table 7.4** and shown from **Figure 7.5** through **Figure 7.9**. The FNN approach has also shown an advantage regarding the necessary time to train the model, as shown in **Figure 7.13**. Although the LSTM-RNN approach has shown better adaptability when submitted to sudden dataflow interruptions or temperature variations, as shown in **Figure 7.8(b)**, **Figure 7.8(d)**, and **Figure 7.11**.

Finally, a novel Li-ion modelling approach using an LSTMECM was developed and compared with GRU-VM and a Third-order ECM. The models were extensively compared for different Li-ion at a wide range of temperature conditions. The LSTM-VM has shown to be more accurate than the two other benchmarks, where could achieve 43 (mV) Root Mean Square Error at -20⁰C, a third when compared to the same situation using ECM as shown in **Figure 5.4**. Although the difference between LSTM-VM and GRU-VM is not that steep, as shown in **Figure 5.7.**

8.2. Future Research

The current macroeconomic scenario shows signals of an increasing complexity generated by more diversified energy, communication, and transportation matrix [193], which in consequence is pulling the demand for more accurate and deployable Li-ion SOC estimation models to help xEV to become more accessible and reach a more substantial portion of the market. As mentioned before, AI is a general-purpose technology; therefore, the engineering effort applied to one area of application can help reduce the effort when applied to a different application, problem or industry. This characteristic can help the fast development of more sophisticated algorithms and models fueled by the plethora of data that are generated by a large net of ubiquitous technologies, e.g. IoT devices, autonomous vehicles.

Finding synergy among these new technologies can leverage public interests, and investments, which in turn can accelerate development and deployment. The methods developed through the course of this thesis can be transferred to other fields and industries, such as the ones related to smart-grid and renewables. They are not entirely restrained to Li-ion batteries, thus possibly applicable to other types of energy storage systems using different chemistries or even not from electrochemical nature, e.g., flywheels. Although, the more immediate application within the current field of application can be expanded to include SOH and SOP estimation. In the case of SOH estimation, a different dataset, including the data from fresh and aged batteries, are necessary, but as presented in

section 3.3, it is possible and would be the next step to develop and combine the method with SOC estimation. As the battery ages, the model trained with only fresh data can have its accuracy reduced, therefore extremely relevant and complementary. By leveraging the data from different vehicles from different parts of the globe would be possible to improve the machine learning models used in the vehicle already deployed and provide several updates through its useful life. New ways to create and develop a machine-learning-based model have emerged, recently autopilots provide a promising way to search several combinations of model structures and features automatically and should be explored in future works. To further improve the models, looking at the gradient-based class, activation maps can help visualize what neurons are activated during a particular prediction. The approach should help build better understanding or at least some intuition of how the model is making its prediction and visualize with parts that have been used.

8.3. Publications

The following publications have resulted from this Ph.D. study:

Published journal papers

1. C. Vidal, O. Gross, R. Gu, P. Kollmeyer, and A. Emadi, "XEV Li-Ion Battery Low-Temperature Effects-Review," IEEE Trans. Veh. Technol., vol. 68, no. 5, pp. 4560–4572, 2019.

2. C. Vidal, P. Malysz, P. Kollmeyer, and A. Emadi, "Machine Learning Applied to Electrified Vehicle Battery State of Charge and State of Health Estimation: State-of-the-Art," IEEE Access, vol. 8, pp. 52796–52814, 2020

3. C. Vidal, P. Kollmeyer, M. Naguib, P. Malysz, O. Gross, and A. Emadi, "Robust xEV Battery State-of-Charge Estimator Design using Deep Neural Networks," SAE International Journal of Advances and Current Practices in Mobility, 2020

Journal papers under review

1. C. Vidal, P. Malysz, P. Kollmeyer, and A. Emadi, "Deep Neural Networks Applied to Electrified Vehicle Battery State of Charge Estimation: Comprehensive Comparison of LSTM and FNN," IEEE Access (submitted 2020).

International refereed conference papers

1. M. Naguib, C. Vidal, P. Kollmeyer, P. Malysz, and A. Emadi, "Comparative Study between Thevenin and Recurrent neural Network Equivalent Circuit Type Li-ion Battery Models" in Proc *2020 IEEE Transportation Electrification Conference and Expo (ITEC)*, Chicago, IL, USA 2020 (accepted for publication)

2. C. Vidal, P. Kollmeyer, E. Chemali, and A. Emadi, "Li-ion Battery State of Charge Estimation Using long short-term memory recurrent neural network with Transfer Learning," in Proc *2019 IEEE Transportation Electrification Conference and Expo (ITEC)*, Novi, MI, USA 2019, pp. 1-6.

3. M. Haubmann, D. Barroso, C. Vidal, L. Bruck, and A. Emadi, "A Novel Multi-Mode Adaptive Energy Consumption Minimization Strategy for P1-

P2 Hybrid Electric Vehicle Architectures," in Proc *2019 IEEE Transportation Electrification Conference and Expo (ITEC),* Novi, MI, USA 2019*, pp. 1–6.*

4. C. Vidal, M. Haussman, D. Barroso, P. Mahvelatishamsabadi, A. Biswas, E. Chemali, R. Ahmed, and A. Emadi, "Hybrid energy storage system State-Of-Charge estimation using artificial neural network for micro-hybrid application," in Proc. *2018 IEEE Transportation Electrification Conference and Expo (ITEC)*, Long Beach, CA, USA, pp. 1075–1081.

REFERENCE

[1]   Z. Yang, "Improving the conversions between the various passenger vehicle fuel economy/CO2 emission standards around the world," International Council on Clean Transportation (ICCT), 2017. https://www.theicct.org/blogs/staff/improving-conversions-between-passenger-vehicle-efficiency-standards (accessed Jan. 01, 2017).

[2]   É. Latulippe, K. Mo, É. Latulippe, and K. Mo, "Outlook for Electric Vehicles and Implications for the Oil Market," Ottawa, Ontario, Canada, 2019. [Online]. Available: https://www.bankofcanada.ca/wp-content/uploads/2019/06/san2019-19.pdf.

[3]   IEA, "Global EV Outlook 2019 – Analysis - IEA," Paris, 2019. Accessed: Mar. 09, 2020. [Online]. Available: https://www.iea.org/reports/global-ev-outlook-2019.

[4]   "Can covid help flatten the climate curve?," The Economist, New York, New York, USA, May 2020.

[5]   B. Bilgin et al., "Making the case for electrified transportation," IEEE Trans. Transp. Electrif., vol. 1, no. 1, pp. 4–17, Jun. 2015

[6]   A. Mahmoudzadeh Andwari, A. Pesiridis, S. Rajoo, R. Martinez-Botas, and V. Esfahanian, "A review of Battery Electric Vehicle technology and readiness levels," Renew. Sustain. Energy Rev., vol. 78, no. March, pp. 414–430, 2017

[7]   S. Zuboff, The Age of Surveillance Capitalism: The Fight for a Human Future at the New Frontier of Power, 1st ed. New York, USA: PublicAffairs, 2019.

[8]   M.A. Hannan, M.S.H. Lipu, A. Hussain, and A. Mohamed, "A review of lithium-ion battery state of charge estimation and management system in electric vehicle applications: Challenges and recommendations," Renew. Sustain. Energy Rev., vol. 78, pp. 834–854, Oct. 2017

[9]   © 2020 IEEE. Reprinted, with permission, from C. Vidal, O. Gross, R. Gu, P. Kollmeyer, and A. Emadi, "XEV Li-Ion Battery Low-Temperature Effects-Review," IEEE Trans. Veh. Technol., vol. 68, no. 5, pp. 4560–4572, 2019

[10]   E. Chemali, M. Preindl, P. Malysz, and A. Emadi, "Electrochemical and electrostatic energy storage and management systems for electric drive vehicles: state-of-the-art review and future trends," IEEE J. Emerg. Sel. Top. Power Electron., vol. 4, no. 3, pp. 1117–1134, Sep. 2016

[11]   C. Government, "Temperature and Precipitation Graph for 1981 to 2010 Canadian Climate Normals," 10/10/2017. https://www.tc.gc.ca/eng/programs/environment-etv-electric-passenger-vehicles-eng-2904.htm (accessed Dec. 31, 2017).

[12]   D. H. Vega, S. Kelouwani, and L. Boulon, "Efficient Internal Resistance and Specific Heat Identification of Li-Ion Battery at Low Temperature Conditions," in Proc. 2015 IEEE Vehicle Power and Propulsion Conference (VPPC), Oct. 2015, pp. 1–6.

[13]   © 2020 IEEE. Reprinted, with permission, from C. Vidal, P. Malysz, P. Kollmeyer, and A. Emadi, "Machine Learning Applied to Electrified Vehicle Battery State of Charge and State of Health Estimation: State-of-the-Art," IEEE Access, vol. 8, pp. 52796–52814, 2020

[14]   R. Zhang et al., "State of the art of lithium-ion battery SOC estimation for electrical vehicles," Energies, vol. 11, no. 7, 2018

[15]   M. Berecibar, I. Gandiaga, I. Villarreal, N. Omar, J. Van Mierlo, and P. Van Den Bossche, "Critical review of state of health estimation methods of Li-ion batteries for real applications," Renew. Sustain. Energy Rev., vol. 56, pp. 572–587, 2016

[16] J. Desjardins, "How much data is generated each day? | World Economic Forum," World Economic Forum. https://www.weforum.org/agenda/2019/04/how-much-data-is-generated-each-day-cf4bddf29f/ (accessed Mar. 11, 2020).

[17] B. Insider, "Car data could be huge business: McKinsey & Co report - Business Insider." https://www.businessinsider.com/car-data-business-mckinsey-and-co-report-2016-10?r=UK (accessed Mar. 11, 2020).

[18] "AI Will Add $15 Trillion To The World Economy By 2030," Forbes, 2019. https://www.forbes.com/sites/greatspeculations/2019/02/25/ai-will-add-15-trillion-to-the-world-economy-by-2030/#1b67646a1852 (accessed Mar. 12, 2020).

[19] © 2020 IEEE. Reprinted, with permission, from C. Vidal, M. Haussman, D. Barroso, P. Mahvelatishamsabadi, A. Biswas, E. Chemali, R. Ahmed, and A. Emadi, "Hybrid energy storage system State-Of-Charge estimation using artificial neural network for micro- hybrid application," in Proc. 2018 IEEE Transportation Electrification Conference and Expo (ITEC), Long Beach, CA, USA, pp. 1075–1081.

[20] H. Liu, A. Gegov, and M. Cocea, Rule Based Systems for Big Data, vol. 13. AG Switzerland: Springer International Publishing, 2016.

[21] E. Chemali, P. J. Kollmeyer, M. Preindl, and A. Emadi, "State-of-charge estimation of Li-ion batteries using deep neural networks: A machine learning approach," J. Power Sources, vol. 400, no. June, pp. 242–255, Oct. 2018

[22] C. Vidal, P. Kollmeyer, M. Naguib, P. Malysz, O. Gross, and A. Emadi, "Robust xEV Battery State-of-Charge Estimator Design using Deep Neural Networks," in Proc WCX SAE World Congress Experience, 2020, [Online]. Available: https://www.sae.org/publications/technical-papers/content/2020-01-1181/.

[23] © 2020 IEEE. Reprinted, with permission, from C. Vidal, P. Kollmeyer, E. Chemali, and A. Emadi, "Li-ion Battery State of Charge Estimation Using Long

Short-Term Memory Recurrent Neural Network with Transfer Learning," in Proc. 2019 IEEE Transp. Electrif. Conf. Expo, ITEC, Novi, MI, USA, Jun, 2019

[24]   N. Nitta, F. Wu, J. T. Lee, and G. Yushin, "Li-ion battery materials: Present and future," Mater. Today, vol. 18, no. 5, pp. 252–264, 2015

[25]   S. LeVine, The powerhouse : inside the invention of a battery to save the world. .

[26]   R. Gu, P. Malysz, D. Wang, W. Wang, H. Yang, and A. Emadi, "On the Design of a Direct Cell Coupled Hybrid Energy Storage System for Plug-in Hybrid Electric Vehicles," 2016.

[27]   P. Malysz, J. Ye, R. Gu, H. Yang, and A. Emadi, "Battery state-of-power peak current calculation and verification using an asymmetric parameter equivalent circuit model," IEEE Trans. Veh. Technol., vol. 65, no. 6, pp. 4512–4522, Jun. 2016

[28]   A. Emadi, Advanced Electric Drive Vehicles. New York: CRC Press, 2015.

[29]   S. Liu, J. Jiang, W. Shi, Z. Ma, L. Y. Wang, and H. Guo, "Butler-Volmer-Equation-Based Electrical Model for High-Power Lithium Titanate Batteries Used in Electric Vehicles," IEEE Trans. Ind. Electron., vol. 62, no. 12, pp. 7557–7568, 2015

[30]   Woodbank Communications Ltd, "Battery Performance Characteristics," Electropaedia. http://www.mpoweruk.com/performance.htm (accessed Nov. 12, 2017).

[31]   J. Jaguemont, L. Boulon, and Y. Dub??, "A comprehensive review of lithium-ion batteries used in hybrid and electric vehicles at cold temperatures," Appl. Energy, vol. 164, pp. 99–114, 2016

[32]   G. Wu et al., "State of Charge Estimation for Li-Ion Battery Based on an Improved Peukert's Equation with Temperature Correction Factor," in Proc. 2016 IEEE Vehicle Power and Propulsion Conference (VPPC), Oct. 2016, pp. 1–4.

[33]   P. Kollmeyer, A. Hackl, and A. Emadi, "Li-ion battery model performance for automotive drive cycles with current pulse and EIS parameterization," in IEEE Transportation Electrification Conference and Expo (ITEC), Jun. 2017, pp. 486–492

[34]   H. Liu, Z. Wei, W. He, and J. Zhao, "Thermal issues about Li-ion batteries and recent progress in battery thermal management systems: A review," Energy Convers. Manag., vol. 150, no. May, pp. 304–330, 2017

[35]   D. Strickland, L. Chittock, D. A. Stone, M. P. Foster, and B. Price, "Estimation of transportation battery second life for use in electricity grid systems," IEEE Trans. Sustain. Energy, vol. 5, no. 3, pp. 795–803, 2014

[36]   M. Petzl, M. Kasper, and M. A. Danzer, "Lithium plating in a commercial lithium-ion battery – A low-temperature aging study," J. Power Sources, vol. 275, pp. 799–807, Feb. 2015

[37]   J. P. Singer and K. P. Birke, "Kinetic study of low temperature capacity fading in Li-ion cells," J. Energy Storage, vol. 13, pp. 129–136, 2017

[38]   T. Waldmann, M. Wilka, M. Kasper, M. Fleischhammer, and M. Wohlfahrt-Mehrens, "Temperature dependent ageing mechanisms in Lithium-ion batteries - A Post-Mortem study," J. Power Sources, vol. 262, pp. 129–135, 2014

[39]   R. Ahmed, M. El Sayed, I. Arasaratnam, J. Tjong, and S. Habibi, "Reduced-Order Electrochemical Model Parameters Identification and State of Charge Estimation for Healthy and Aged Li-Ion Batteries—Part II: Aged Battery Model and State of Charge Estimation," IEEE J. Emerg. Sel. Top. Power Electron., vol. 2, no. 3, pp. 678–690, Jun. 2014

[40]   R. Ahmed, M. El Sayed, I. Arasaratnam, Jimi Tjong, and S. Habibi, "Reduced-Order Electrochemical Model Parameters Identification and SOC Estimation for Healthy and Aged Li-Ion Batteries Part I: Parameterization Model

Development for Healthy Batteries," IEEE J. Emerg. Sel. Top. Power Electron., vol. 2, no. 3, pp. 659–677, Sep. 2014

[41]   R. Gu, P. Malysz, and A. Emadi, "A novel battery/ ultracapacitor hybrid energy storage system analysis based on physics-based lithium-ion battery modeling," 2015 {IEEE} {Transportation} {Electrification} {Conference} {Expo}, pp. 1–6, 2015

[42]   V. Sangwan, A. Sharma, R. Kumar, and A. K. Rathore, "Equivalent circuit model parameters estimation of Li-ion battery: C-rate, SOC and temperature effects," in Proc 2016 IEEE International Conference on Power Electronics, Drives and Energy Systems (PEDES), Dec. 2016, pp. 1–6.

[43]   W. Wang et al., "Comparison of Kalman Filter-based state of charge estimation strategies for Li-Ion batteries," in Proc. 2016 IEEE Transp. Electrif. Conf. Expo, ITEC, Dearborn, MI, USA, June 2016

[44]   L. ion battery productionAntti Väyrynen and J. Salminen, "Lithium ion battery production," J. Chem. Thermodyn., vol. 46, pp. 80–85, 2012

[45]   A. Baumgardt, F. Bachheibl, A. Patzak, D. Gerling, and A. E. Machine, "48V Traction: Innovative Drive Topology and Battery," pp. 0–5, 2016.

[46]   G. Ozcan, M. Pajovic, Z. Sahinoglu, Y. Wang, P. V Orlik, and T. Wada, "Online State of Charge Estimation for Lithium-Ion Batteries Using Gaussian Process Regression," pp. 0–5, 2016.

[47]   J. Ye, A. Emadi, R. Gu, P. Malysz, and H. Yang, "State-of-charge and state-of-health estimation with state constraints and current sensor bias correction for electrified powertrain vehicle batteries," IET Electr. Syst. Transp., vol. 6, no. 2, pp. 136–144, Jun. 2016

[48]   M. Ismail, R. Dlyma, A. Elrakaybi, R. Ahmed, and S. Habibi, "Battery state of charge estimation using an Artificial Neural Network," in Proc 2017 IEEE

Transportation Electrification Conference and Expo (ITEC), Chicago, IL, USA, Jun. 2017, pp. 342–349.

[49]   M. Shafique et al., "Adaptive and Energy-Efficient Architectures for Machine Learning: Challenges, Opportunities, and Research Roadmap," in Proc 2017 IEEE Computer Society Annual Symposium on VLSI (ISVLSI), Jul. 2017, pp. 627–632.

[50]   J. Meng et al., "An overview of online implementable SOC estimation methods for Lithium-ion batteries," in Proc. 2017 International Conference on Optimization of Electrical and Electronic Equipment (OPTIM) & 2017 Intl Aegean Conference on Electrical Machines and Power Electronics (ACEMP), May 2017, pp. 573–580.

[51]   Hongchuan Wei, W. Ross, S. Varisco, P. Krief, and S. Ferrari, "Modeling of human driver behavior via receding horizon and artificial neural network controllers," in Proc. 52nd IEEE Conference on Decision and Control, Dec. 2013, pp. 6778–6785.

[52]   J. Wu, C. Zhang, and Z. Chen, "An online method for lithium-ion battery remaining useful life estimation using importance sampling and neural networks," Appl. Energy, vol. 173, pp. 134–140, 2016

[53]   A. Nuhic, T. Terzimehic, T. Soczka-guth, M. Buchholz, and K. Dietmayer, "Health diagnosis and remaining useful life prognostics of lithium-ion batteries using data-driven methods q," J. Power Sources, vol. 239, pp. 680–688, 2013

[54]   N. Meyer, I. Whittal, M. Christenson, and A. Loiselle-Lapointe, "The Impact of Driving Cycle and Climate on Electrical Consumption & Range of Fully Electric Passenger Vehicles," 2012. Accessed: Dec. 22, 2016. [Online]. Available: https://www.tc.gc.ca/eng/programs/environment-etv-electric-passenger-vehicles-eng-2904.htm.

[55]   J. R. M. Delos Reyes, R. V. Parsons, and R. Hoemsen, "Winter Happens: The Effect of Ambient Temperature on the Travel Range of Electric Vehicles," IEEE Trans. Veh. Technol., vol. 65, no. 6, pp. 4016–4022, 2016

[56]   S. S. Zhang, K. Xu, and T. R. Jow, "Low temperature performance of graphite electrode in Li-ion cells," Electrochim. Acta, vol. 48, no. 3, pp. 241–246, Dec. 2002

[57]   C.-Y. Wang et al., "Lithium-ion battery structure that self-heats at low temperatures," Nature, vol. 529, no. 7587, 2016

[58]   Hyun-Sik Song et al., "Experimental study on the effects of pre-heating a battery in a low-temperature environment," in Proc. 2012 IEEE Vehicle Power and Propulsion Conference, Oct. 2012, pp. 1198–1201.

[59]   J. Jiang et al., "A reduced low-temperature electro-thermal coupled model for lithium-ion batteries," Appl. Energy, vol. 177, pp. 804–816, 2016

[60]   H. Ruan, J. Jiang, Q. Ju, B. Sun, and G. Cheng, "A Reduced Wide-temperature-range Electro-thermal Model and Thermal Parameters Determination for Lithium-ion Batteries," Energy Procedia, vol. 105, pp. 805–810, 2017

[61]   J. Lindgren and P. D. Lund, "Effect of extreme temperatures on battery charging and performance of electric vehicles," J. Power Sources, vol. 328, pp. 37–45, 2016

[62]   F. Zheng, J. Jiang, B. Sun, W. Zhang, and M. Pecht, "Temperature dependent power capability estimation of lithium-ion batteries for hybrid electric vehicles," Energy, vol. 113, 2016

[63]   J. Cao, A. Emadi, and S. Member, "A New Battery / UltraCapacitor Hybrid Energy Storage System for Electric , Hybrid , and Plug-In Hybrid Electric Vehicles," IEEE Trans. POWER Electron., vol. 27, no. 1, pp. 122–132, 2012

[64] J. Yang and G. Zhu, "Stochastic Predictive Boundary Management for a Hybrid Powertrain," IEEE Trans. Veh. Technol., vol. 65, no. 6, pp. 4700–4713, Jun. 2016

[65] M. Ecker, P. Shafiei Sabet, and D. U. Sauer, "Influence of operational condition on lithium plating for commercial lithium-ion batteries – Electrochemical experiments and post-mortem-analysis," Appl. Energy, vol. 206, no. July, pp. 934–946, 2017

[66] Dong Zhang, S. Dey, H. E. Perez, and S. J. Moura, "Remaining useful life estimation of Lithium-ion batteries based on thermal dynamics," 2017 Am. Control Conf., no. Icc, pp. 4042–4047, 2017

[67] Q. Wang, P. Ping, X. Zhao, G. Chu, J. Sun, and C. Chen, "Thermal runaway caused fire and explosion of lithium ion battery," J. Power Sources, vol. 208, pp. 210–224, 2012

[68] P. Zhang, J. Zhu, M. Wang, N. Imanishi, and O. Yamamoto, "Lithium dendrite suppression and cycling efficiency of lithium anode," Electrochem. commun., vol. 87, no. November 2017, pp. 27–30, 2018

[69] C. von Lüders et al., "Lithium plating in lithium-ion batteries investigated by voltage relaxation and in situ neutron diffraction," J. Power Sources, vol. 342, pp. 17–23, 2017

[70] J. Jaguemont, L. Boulon, P. Venet, Y. Dubé, and A. Sari, "Low Temperature Aging Tests for Lithium-ion Batteries," Accessed: Jul. 04, 2017. [Online]. Available: https://journals-scholarsportal-info.libaccess.lib.mcmaster.ca/pdf/21635145/v2015inone/1284_ltatflb.xml.

[71] L. Lu, X. Han, J. Li, J. Hua, and M. Ouyang, "A review on the key issues for lithium-ion battery management in electric vehicles," J. Power Sources, vol. 226, pp. 272–288, 2013

[72]   "A review of international abuse testing standards and regulations for lithium ion batteries in electric and hybrid electric vehicles," Renew. Sustain. Energy Rev., Jul. 2017

[73]   S. Abada, G. Marlair, A. Lecocq, M. Petit, V. Sauvant-Moynot, and F. Huet, "Safety focused modeling of lithium-ion batteries: A review," J. Power Sources, vol. 306, pp. 178–192, 2016

[74]   A. Hofmann, N. Uhlmann, C. Ziebert, O. Wiegand, A. Schmidt, and T. Hanemann, "Preventing Li-ion cell explosion during thermal runaway with reduced pressure," Appl. Therm. Eng., vol. 124, pp. 539–544, 2017

[75]   F. Leng, Z. Wei, C. M. Tan, and R. Yazami, "Hierarchical degradation processes in lithium-ion batteries during ageing," Electrochim. Acta, vol. 256, pp. 52–62, 2017

[76]   X. Feng, M. Ouyang, X. Liu, L. Lu, Y. Xia, and X. He, "Thermal runaway mechanism of lithium ion battery for electric vehicles: A review," Energy Storage Mater., no. May, pp. 1–22, 2017

[77]   Y. Gurkaynak, A. Khaligh, and A. Emadi, "Neural adaptive control strategy for hybrid electric vehicles with parallel powertrain," in Proc. IEEE Vehicle Power and Propulsion Conference, Sep. 2010, pp. 1–6.

[78]   R. Gu, P. Malysz, H. Yang, and A. Emadi, "On the Suitability of Electrochemical-Based Modeling for Lithium-ion Batteries," IEEE Trans. Transp. Electrif., vol. PP, no. 99, p. 1, 2016

[79]   L. Zhou, Y. Zheng, M. Ouyang, and L. Lu, "A study on parameter variation effects on battery packs for electric vehicles," J. Power Sources, vol. 364, pp. 242–252, 2017

[80]   B. Agrawal et al., "Non-dissipative battery cell balancing using half-bridge switching circuit," in Proc. 2016 IEEE Transp. Electrif. Conf. Expo, ITEC, Dearborn, MI, USA, Jun, 2016

[81]   N. Yang, X. Zhang, B. Shang, and G. Li, "Unbalanced discharging and aging due to temperature differences among the cells in a lithium-ion battery pack with parallel combination," J. Power Sources, vol. 306, pp. 733–741, 2016

[82]   Y. Zheng, M. Ouyang, L. Lu, and J. Li, "Understanding aging mechanisms in lithium-ion battery packs: From cell capacity loss to pack capacity evolution," J. Power Sources, vol. 278, pp. 287–295, 2015

[83]   L. McCurlie, M. Preindl, and A. Emadi, "Fast Model Predictive Control for Redistributive Lithium Ion Battery Balancing," IEEE Trans. Ind. Electron., vol. 0046, no. c, pp. 1–1, 2016

[84]   C. Zhang, J. Jiang, Y. Gao, W. Zhang, Q. Liu, and X. Hu, "Charging optimization in lithium-ion batteries based on temperature rise and charge time," Appl. Energy, vol. 194, pp. 569–577, May 2017, doi: 10.1016/j.apenergy.2016.10.059.

[85]   S. GUSTAFSON, "Tesla developing battery preheating feature to lessen cold-weather drain," Autoblog, 2017. https://www.autoblog.com/2017/12/19/tesla-battery-preheating-cold-weather/ (accessed Dec. 28, 2017).

[86]   H. Ruan et al., "A rapid low-temperature internal heating strategy with optimal frequency based on constant polarization voltage for lithium-ion batteries," Appl. Energy, vol. 177, pp. 771–782, Sep. 2016

[87]   A. S. Mussa, M. Klett, M. Behm, G. Lindbergh, and R. W. Lindström, "Fast-charging to a partial state of charge in lithium-ion batteries: A comparative ageing study," J. Energy Storage, vol. 13, pp. 325–333, 2017

[88]   USABC, "USABC Goals for Advanced Batteries for EVs - CY 2020 Commercialization." www.uscar.org/commands/files_download.php?files_id=364 (accessed Dec. 30, 2017).

[89]   Xudong Liu, Yanping Wu, and Jianmin Duan, "Power split control strategy for a series Hybrid Electric Vehicle using fuzzy logic," in Proc 2008 IEEE International Conference on Automation and Logistics, Sep. 2008, pp. 481–486

[90]   Y. Ji and C. Y. Wang, "Heating strategies for Li-ion batteries operated from subzero temperatures," Electrochim. Acta, vol. 107, pp. 664–674, Sep. 2013

[91]   G. Zhang, S. Ge, T. Xu, X.-G. Yang, H. Tian, and C.-Y. Wang, "Rapid self-heating and internal temperature sensing of lithium-ion batteries at low temperatures," Electrochim. Acta, vol. 218, pp. 149–155, 2016

[92]   A. Lajunen, T. Hadden, R. Hirmiz, J. Cotton, and A. Emadi, "Thermal energy storage for increasing heating performance and efficiency in electric vehicles," in Proc. 2017 IEEE Transp. Electrif. Conf. Expo, ITEC, Chicago, IL, USA, Jun, 2017, pp. 95–100, 2017.

[93]   G. Bower, "Tesla or GM: Who Has The Best Battery Thermal Management?," Inside EVs, 2015. https://insideevs.com/tesla-or-gm-who-has-the-best-battery-thermal-management-bower/ (accessed Dec. 28, 2017).

[94]   T. Moloughney, "Understanding Battery Capacity Loss From A Four Year BMW Electric Trial Veteran," Inside EVs, 2013. https://insideevs.com/understanding-battery-capacity-loss-from-a-four-year-bmw-electric-trial-veteran/ (accessed Dec. 28, 2017).

[95]   Y. Ji, Y. Zhang, and C.-Y. Wang, "Li-Ion Cell Operation at Low Temperatures," J. Electrochem. Soc., vol. 160, no. 4, pp. A636–A649, Feb. 2013

[96]   Q. Wang, B. Jiang, B. Li, and Y. Yan, "A critical review of thermal management models and solutions of lithium-ion batteries for the development of

pure electric vehicles," Renew. Sustain. Energy Rev., vol. 64, pp. 106–128, Oct. 2016

[97]   J. Taggart, "Ambient temperature impacts on real-world electric vehicle efficiency & range," in Proc. 2017 IEEE Transportation Electrification Conference and Expo (ITEC), Chicago, IL, USA, Jun. 2017, pp. 186–190.

[98]   J. Smith, M. Hinterberger, C. Schneider, and J. Koehler, "Energy savings and increased electric vehicle range through improved battery thermal management," Appl. Therm. Eng., vol. 101, 2016

[99]   K. R. Konecky, "xEV industry trends of charging & battery systems battery packs of modern xEVs," in AABC Europe, 2018, pp. 1–29.

[100]   G. Piłatowicz, A. Marongiu, J. Drillkens, P. Sinhuber, and D. U. Sauer, "A critical overview of definitions and determination techniques of the internal resistance using lithium-ion, lead-acid, nickel-metal-hydride batteries and electrochemical double-layer capacitors as examples," J. Power Sources, vol. 296, pp. 365–376, 2015

[101]   K. Palmer, J. E. Tate, Z. Wadud, and J. Nellthorp, "Total cost of ownership and market share for hybrid and electric vehicles in the UK, US and Japan," Appl. Energy, vol. 209, no. July 2017, pp. 108–119, 2018

[102]   Qnovo Incorporated, "THE COST COMPONENTS OF A LITHIUM ION BATTERY," Qnovo, 2016. https://qnovo.com/82-the-cost-components-of-a-battery/.

[103]   G. Berckmans, M. Messagie, J. Smekens, N. Omar, L. Vanhaverbeke, and J. Van Mierlo, "Cost projection of state of the art lithium-ion batteries for electric vehicles up to 2030," Energies, vol. 10, no. 9, 2017

[104] J. Cole, "At $100/kWh It Is 'All Over' For The Internal Combustion Engine – Energy Expert," Inside Evs, 2013. https://insideevs.com/at-100kwh-it-is-all-over-for-the-internal-combustion-engine-energy-expert/ (accessed Dec. 30, 2017).

[105] E. L. Olson, "Lead market learning in the development and diffusion of electric vehicles," J. Clean. Prod., vol. 172, pp. 3279–3288, Jan. 2018

[106] R. Gu, "Physics-Based Modeling of Direct Coupled Hybrid Energy Storage Modules in Electrified Vehicles," 2016.

[107] P. Keil and A. Jossen, "Charging protocols for lithium-ion batteries and their impact on cycle life—An experimental study with different 18650 high-power cells," J. Energy Storage, vol. 6, pp. 125–141, 2016

[108] E. Chemali et al., "Minimizing Battery Wear in a Battery-Ultracapacitor Hybrid Energy Storage System using a Linear Quadratic Regulator," pp. 3265–3270, 2015.

[109] A. Menahem, "Vehicle electrification : is the path to mass market open ?," in AABC Europe, 2018, pp. 1–38.

[110] I. Goodfellow, Y. Bengio, and A. Courville, Deep Learning. MIT Press, 2016.

[111] A. Shrestha and A. Mahmood, "Review of Deep Learning Algorithms and Architectures," IEEE Access, vol. 7, pp. 53040–53065, 2019

[112] X. Dang, L. Yan, H. Jiang, X. Wu, and H. Sun, "Open-circuit voltage-based state of charge estimation of lithium-ion power battery by combining controlled auto-regressive and moving average modeling with feedforward-feedback compensation method," Int. J. Electr. Power Energy Syst., vol. 90, pp. 27–36, 2017

[113] W. He, N. Williard, C. Chen, and M. Pecht, "State of charge estimation for Li-ion batteries using neural network modeling and unscented Kalman filter-based error cancellation," Int. J. Electr. Power Energy Syst., vol. 62, pp. 783–791, 2014

[114] C. Chen, R. Xiong, R. Yang, W. Shen, and F. Sun, "State-of-charge estimation of lithium-ion battery using an improved neural network model and extended Kalman filter," J. Clean. Prod., vol. 234, no. 5, pp. 1153–1164, 2019

[115] J. Yang et al., "Rapid prediction of the open-circuit-voltage of lithium ion batteries based on an effective voltage relaxation model," Energies, vol. 11, no. 12, 2018

[116] Y. Hu and Z. Wang, "Study on soc estimation of lithium battery based on improved bp neural network," 2019 8th Int. Symp. Next Gener. Electron. ISNE 2019, pp. 1–3, 2019

[117] J. Remmlinger, M. Buchholz, M. Meiler, P. Bernreuter, and K. Dietmayer, "State-of-health monitoring of lithium-ion batteries in electric vehicles by on-board internal resistance estimation," J. Power Sources, vol. 196, no. 12, pp. 5357–5363, 2011

[118] M. A. Hannan, M. S. H. H. Lipu, A. Hussain, M. H. Saad, and A. Ayob, "Neural network approach for estimating state of charge of lithium-ion battery using backtracking search algorithm," IEEE Access, vol. 6, no. c, pp. 10069–10079, 2018

[119] S. Tong, J. H. Lacap, and J. W. Park, "Battery state of charge estimation using a load-classifying neural network," J. Energy Storage, vol. 7, pp. 236–243, 2016

[120] M. Charkhgard and M. Farrokhi, "State-of-charge estimation for lithium-ion batteries using neural networks and EKF," IEEE Trans. Ind. Electron., vol. 57, no. 12, pp. 4178–4187, 2010.

[121] M. Shahriari and M. Farrokhi, "On-line State of Health Estimation of VRLA Batteries Using State of Charge," IEEE Trans. Ind. Electron., vol. 60, no. 1, pp. 191-202., 2012

[122] M. Haddad Zarif, M. Charkhgard, and A. Alfi, "Hybrid state of charge estimation for lithium-ion batteries: design and implementation," IET Power Electron., vol. 7, no. 11, pp. 2758–2764, 2014

[123] M. Charkhgard and H. Gholizade-Narm, "Lithium-ion battery state of charge estimation based on square-root unscented Kalman filter," IET Power Electron., vol. 6, no. 9, pp. 1833–1841, 2013

[124] X. Chen, W. Shen, M. Dai, Z. Cao, J. Jin, and A. Kapoor, "Robust Adaptive Sliding-Mode Observer Using RBF Neural Network for Lithium-Ion Battery State of Charge Estimation in Electric Vehicles," IEEE Trans. Veh. Technol., vol. 65, no. 4, pp. 1936–1947, Apr. 2016

[125] X. Chen, W. Shen, Z. Cao, and A. Kapoor, "Adaptive gain sliding mode observer for state of charge estimation based on combined battery equivalent circuit model," Comput. Chem. Eng., vol. 64, pp. 114–123, 2014

[126] F. Sun, R. Xiong, and H. He, "A systematic state-of-charge estimation framework for multi-cell battery pack in electric vehicles using bias correction technique," Appl. Energy, vol. 162, pp. 1399–1409, 2016

[127] G.-B. Huang, Q.-Y. Zhu, and C.-K. Siew, "Extreme learning machine: Theory and applications," Neurocomputing, vol. 70, no. 1–3, pp. 489–501, Dec. 2006

[128] J. Du, Z. Liu, and Y. Wang, "State of charge estimation for Li-ion battery based on model from extreme learning machine," Control Eng. Pract., vol. 26, no. 1, pp. 11–19, 2014

[129] M. S. Hossain Lipu, M. A. Hannan, A. Hussain, M. H. Saad, A. Ayob, and M. N. Uddin, "Extreme learning machine model for state-of-charge estimation of lithium-ion battery using gravitational search algorithm," IEEE Trans. Ind. Appl., vol. 55, no. 4, pp. 4225–4234, 2019

[130] J. C. Alvarez, "Support Vector Machines Used to Estimate the Battery State of Charge," IEEE Trans. Power Electron., vol. 28, no. 12, pp. 5919–5926, 2013.

[131] J. C. Álvarez Antón, P. J. García Nieto, F. J. de Cos Juez, F. Sánchez Lasheras, M. González Vega, and M. N. Roqueñí Gutiérrez, "Battery state-of-charge estimator using the SVM technique," Appl. Math. Model., vol. 37, no. 9, pp. 6244–6253, May 2013

[132] K. A. Althelaya, E. S. M. El-Alfy, and S. Mohammed, "Evaluation of Bidirectional LSTM for Short and Long-Term Stock Market Prediction," 2018 9th Int. Conf. Inf. Commun. Syst. ICICS 2018, vol. 2018-Janua, pp. 151–156, 2018

[133] M. Haubmann, D. Barroso, C. Vidal, L. Bruck, and A. Emadi, "A Novel Multi-Mode Adaptive Energy Consumption Minimization Strategy for P1-P2 Hybrid Electric Vehicle Architectures," in Proc. 2019 IEEE Transportation Electrification Conference and Expo (ITEC), Novi, MI, USA, Jun. 2019, pp. 1–6.

[134] R. Pascanu, T. Mikolov, and Y. Bengio, "On the difficulty of training Recurrent Neural Networks," no. 2, 2012, [Online]. Available: http://arxiv.org/abs/1211.5063.

[135] S. Hochreiter and J. Schmidhuber, "Long Short-Term Memory," Neural Comput., vol. 9, no. 8, pp. 1735–1780, Nov. 1997

[136] C. Olah, "Understanding LSTM Networks [Blog]," Web Page, 2015. https://colah.github.io/posts/2015-08-Understanding-LSTMs/ (accessed Jan. 27, 2020).

[137] E. Chemali, P. Kollmeyer, M. Preindl, R. Ahmed, and A. Emadi, "Long short-term memory-networks for accurate state of charge estimation of Li-ion batteries," IEEE Trans. Ind. Electron., vol. 65, no. 8, 2018

[138] J. Chung, C. Gulcehre, K. Cho, and Y. Bengio, "Empirical Evaluation of Gated Recurrent Neural Networks on Sequence Modeling," in Proc. 2015 IEEE Int. Conf. Rehabil. Robot., vol. 2013, pp. 119–124, Dec. 2014.

[139] "Panasonic 18650PF Li-ion Battery Data." doi: http://dx.doi.org/10.17632/wykht8y7tg.1#folder-96f196a8-a04d-4e6a-827d-0dc4d61ca97b.

[140] C. Bian, H. He, and S. Yang, "Stacked bidirectional long short-term memory networks for state-of-charge estimation of lithium-ion batteries," Energy, vol. 191, no. xxxx, p. 116538, Jan. 2020

[141] C. Li, F. Xiao, and Y. Fan, "An approach to state of charge estimation of lithium-ion batteries based on recurrent neural networks with gated recurrent unit," Energies, vol. 12, no. 9, p. 1592, 2019

[142] F. Yang, X. Song, F. Xu, and K.-L. Tsui, "State-of-Charge Estimation of Lithium-Ion Batteries via Long Short-Term Memory Network," IEEE Access, vol. 7, pp. 53792–53799, 2019

[143] A. Bonfitto, S. Feraco, A. Tonoli, N. Amati, and F. Monti, "Estimation Accuracy and Computational Cost Analysis of Artificial Neural Networks for State of Charge Estimation in Lithium Batteries," Batteries, vol. 5, no. 2, p. 47, Jun. 2019

[144] M. S. H. Lipu, M. A. Hannan, A. Hussain, M. H. M. Saad, A. Ayob, and F. Blaabjerg, "State of Charge Estimation for Lithium-Ion Battery Using Recurrent NARX Neural Network Model Based Lighting Search Algorithm," IEEE Access, vol. 6, pp. 28150–28161, 2018

[145] F. Yang, W. Li, C. Li, and Q. Miao, "State-of-charge estimation of lithium-ion batteries based on gated recurrent neural network," Energy, vol. 175, pp. 66–75, 2019

[146]   A. C. Caliwag and W. Lim, "Hybrid VARMA and LSTM Method for Lithium-ion Battery State-of-Charge and Output Voltage Forecasting in Electric Motorcycle Applications," IEEE Access, vol. 7, pp. 59680–59689, 2019

[147]   A. Khalid, A. Sundararajan, I. Acharya, and A. I. Sarwat, "Prediction of Li-Ion Battery State of Charge Using Multilayer Perceptron and Long Short-Term Memory Models," ITEC 2019 - 2019 IEEE Transp. Electrif. Conf. Expo, 2019

[148]   H. Chaoui, C. C. Ibe-ekeocha, S. Member, and C. C. Ibe-ekeocha, "State of charge and state of health estimation for lithium batteries using recurrent neural networks," IEEE Trans. Veh. Technol., vol. 66, no. 10, pp. 8773–8783, Oct. 2017

[149]   G. You, S. Park, and D. Oh, "Real-time state-of-health estimation for electric vehicle batteries: A data-driven approach," Appl. Energy, vol. 176, pp. 92–103, Aug. 2016

[150]   D. Andre, A. Nuhic, T. Soczka-Guth, and D. U. Sauer, "Comparative study of a structured neural network and an extended Kalman filter for state of health determination of lithium-ion batteries in hybrid electric vehicles," Eng. Appl. Artif. Intell., vol. 26, no. 3, pp. 951–961, 2013

[151]   H. Chaoui, C. C. Ibe-Ekeocha, and H. Gualous, "Aging prediction and state of charge estimation of a LiFePO4 battery using input time-delayed neural networks," Electr. Power Syst. Res., vol. 146, pp. 189–197, 2017

[152]   A. A. Hussein, "Capacity Fade Estimation in Electric Vehicle Li-Ion Batteries Using Artificial Neural Networks," IEEE Trans. Ind. Appl., vol. 51, no. 3, pp. 2321–2330, May 2015

[153]   J. Wu, Y. Wang, X. Zhang, and Z. Chen, "A novel state of health estimation method of Li-ion battery using group method of data handling," J. Power Sources, vol. 327, pp. 457–464, Sep. 2016

[154] G.-W. You, S. Park, and D. Oh, "Diagnosis of Electric Vehicle Batteries Using Recurrent Neural Networks," IEEE Trans. Ind. Electron., vol. 64, no. 6, pp. 4885–4893, Jun. 2017

[155] S. Hochreiter and J. Urgen Schmidhuber, "Long Short-Term Memory," Neural Comput., vol. 9, no. 8, pp. 1735–1780, 1997

[156] A. Veeraraghavan, V. Adithya, A. Bhave, and S. Akella, "Battery aging estimation with deep learning," in Proc 2017 IEEE Transportation Electrification Conference (ITEC-India), Dec. 2017, pp. 1–4.

[157] B. Saha and K. Goebel, "Battery Data Set." NASA Ames Prognostics Data Repository   (http://ti.arc.nasa.gov/project/prognostic-data-repository),   NASA Ames Research Cente, Moffett Field, CA, 2007, [Online]. Available: http://ti.arc.nasa.gov/project/prognostic-data-repository.

[158] Y. Choi, S. Ryu, K. Park, and H. Kim, "Machine Learning-Based Lithium-Ion Battery Capacity Estimation Exploiting Multi-Channel Charging Profiles," IEEE Access, vol. 7, pp. 75143–75152, 2019

[159] C. Zhang, Y. Zhu, G. Dong, and J. Wei, "Data-driven lithium-ion battery states estimation using neural networks and particle filtering," Int. J. Energy Res., vol. 43, no. 14, p. er.4820, Aug. 2019

[160] A. Eddahech, O. Briat, N. Bertrand, J.-Y. Delétage, and J.-M. Vinassa, "Behavior and state-of-health monitoring of Li-ion batteries using impedance spectroscopy and recurrent neural networks," Int. J. Electr. Power Energy Syst., vol. 42, no. 1, pp. 487–494, Nov. 2012

[161] X. Hu, J. Jiang, D. Cao, and B. Egardt, "Battery Health Prognosis for Electric Vehicles Using Sample Entropy and Sparse Bayesian Predictive Modeling," IEEE Trans. Ind. Electron., vol. 63, no. 4, pp. 2645–2656, 2015

[162]   J. S. Richman, D. E. Lake, and J. R. Moorman, "Sample Entropy," Methods Enzymol., vol. 384, pp. 172–184, Jan. 2004

[163]   J. Kim, S. Member, S. Lee, and B. H. Cho, "Complementary Cooperation Algorithm Based on DEKF Combined With Pattern Recognition for SOC / Capacity Estimation and SOH Prediction," Power, vol. 27, no. 1, pp. 436–451, 2012.

[164]   V. Klass, M. Behm, and G. Lindbergh, "A support vector machine-based state-of-health estimation method for lithium-ion batteries under electric vehicle operation," J. Power Sources, vol. 270, pp. 262–272, Dec. 2014

[165]   B. Saha, S. Poll, K. Goebel, and J. Christophersen, "An integrated approach to battery health monitoring using bayesian regression and state estimation," in 2007 IEEE Autotestcon, Sep. 2007, pp. 646–653

[166]   P.-H. Michel and V. Heiries, "An Adaptive Sigma Point Kalman Filter Hybridized by Support Vector Machine Algorithm for Battery SoC and SoH Estimation," in Proc. 2015 IEEE 81st Vehicular Technology Conference (VTC Spring), May 2015, vol. 2015, pp. 1–7.

[167]   X. Feng et al., "Online State-of-Health Estimation for Li-Ion Battery Using Partial Charging Segment Based on Support Vector Machine," IEEE Trans. Veh. Technol., vol. 68, no. 9, pp. 8583–8592, 2019

[168]   Z. He, M. Gao, G. Ma, Y. Liu, and S. Chen, "Online state-of-health estimation of lithium-ion batteries using Dynamic Bayesian Networks," J. Power Sources, vol. 267, pp. 576–583, Dec. 2014

[169]   H.-T. Lin, T.-J. Liang, and S.-M. Chen, "Estimation of Battery State of Health Using Probabilistic Neural Network," IEEE Trans. Ind. Informatics, vol. 9, no. 2, pp. 679–685, May 2013

[170]   K. A. Severson et al., "Data-driven prediction of battery cycle life before capacity degradation," Nat. Energy, vol. 4, no. 5, pp. 383–391, 2019

[171]   P. Kollmeyer, C. Vidal, M. Naguib, and M. Skells, "LG 18650HG2 Li-ion Battery Data and Example Deep Neural Network xEV SOC Estimator Script." Mendeley Data, 2020

[172]   H. Chaoui and C. C. Ibe-Ekeocha, "State of charge and state of health estimation for lithium batteries using recurrent neural networks," IEEE Trans. Veh. Technol., vol. 66, no. 10, pp. 8773–8783, Oct. 2017

[173]   D. Renner, F. Achhammer, P. Jansen, D. Vergossen, W. John, and S. Frei, "Optimization of a 12V dual-battery system for micro-hybrid vehicles," pp. 1–6

[174]   A123, "A123 12V starter battery." http://www.a123systems.com/wp-content/uploads/12V-Starter-Battery-Flier_2016_Gen-3.pdf (accessed Mar. 09, 2018).

[175]   K. Ng, Y. Huang, C. Moo, and Y. Hsieh, "An enhanced coulomb counting method for estimating state-of-charge and state-of-health of lead-acid batteries," in Proc. International Telecommunications Energy Conference (INTELEC), Incheon, SKR, Oct 2009, Oct., pp. 1–5.

[176]   K. S. Ng, C. S. Moo, Y. P. Chen, and Y. C. Hsieh, "Enhanced coulomb counting method for estimating state-of-charge and state-of-health of lithium-ion batteries," Appl. Energy, vol. 86, no. 9, pp. 1506–1511, 2009

[177]   J. Wang, B. Cao, Q. Chen, and F. Wang, "Combined state of charge estimator for electric vehicle battery pack," Control Eng. Pract., vol. 15, no. 12, pp. 1569–1576, 2007

[178]   A. Rahmoun, H. Biechl, and A. Rosin, "SOC estimation for Li-Ion batteries based on equivalent circuit diagrams and the application of a Kalman filter," in 2012 Electric Power Quality and Supply Reliability, Jun. 2012, pp. 1–4

[179]   A. A. Hussein, "A neural network based method for instantaneous power estimation in electric vehicles' Li-ion batteries," in Proc. IEEE Applied Power Electronics Conference and Exposition (APEC), San Antonio, TX, March, Mar. 2017, pp. 3122–3126.

[180]   Cheng-Hui Cai, Dong-Du, Zhi-Yu Liu, and Hua Zhang, "Artificial neural network in estimation of battery state of-charge (SOC) with nonconventional input variables selected by correlation analysis," in Proc. International Conference on Machine Learning and Cybernetics, vol. 3, Beijing, China, China, Nov 2002, pp. 1619–1625

A. Rahmoun, H. Biechl, and A. Rosin, "SOC estimation for Li-Ion batteries based on equivalent circuit diagrams and the application of a Kalman filter," in Proc. 2012 Electric Power Quality and Supply Reliability, Jun. 2012, pp. 1–4.

[181]   Y. Guo, Z. Zhao, and L. Huang, "SoC Estimation of Lithium Battery Based on Improved BP Neural Network," in Energy Procedia, May 2017, vol. 105, pp. 4153–4158

[182]   P. Malysz, J. Ye, R. Gu, H. Yang, and A. Emadi, "Battery state - of - power peak purrent calculation and verification using an asymmetric parameter equivalent circuit model," IEEE Trans. Veh. Technol., vol. 65, no. 6, pp. 4512–4522, Jun. 2016

[183]   M. Tutuianu et al., "Development of a World-wide Worldwide harmonized Light duty driving Test Cycle (WLTC)," Tech. Rep., vol. 03, no. January, pp. 7–10, 2014

[184]   Q. Jiang, F. Ossart, and C. Marchand, "Comparative study of real-time HEV energy management strategies," IEEE Trans. Veh. Technol., vol. 66, no. 12, pp. 10875–10888, 2017

[185]   M. Gelbke and C. Mondoloni, "Flooded starting-lighting-ignition (SLI) and enhanced flooded batteries (EFBs)," in Lead-Acid Batteries for Future Automobiles, Elsevier, 2017, pp. 149–184.

[186] P. Malysz, R. Gu, J. Ye, H. Yang, and A. Emadi, "State-of-charge and state-of-health estimation with state constraints and current sensor bias correction for electrified powertrain vehicle batteries," IET Electr. Syst. Transp., vol. 6, no. 2, pp. 136–144, Jun. 2016

[187] L. W. Juang, P. J. Kollmeyer, T. M. Jahns, and R. D. Lorenz, "Improved nonlinear model for electrode voltage-current relationship for more consistent online battery system identification," IEEE Trans. Ind. Appl., vol. 49, no. 3, pp. 1480–1488, 2013

[188] R. Zhao, P. J. Kollmeyer, R. D. Lorenz, T. M. Jahns, and 재호김, "A Compact Methodology Via a Recurrent Neural Network for Accurate Equivalent Circuit Type Modeling of Lithium-Ion Batteries," IEEE Trans. Ind. Appl., vol. 55, no. 2, pp. 1922–1931, Mar. 2019

[189] P. Kollmeyer, "Panasonic 18650PF Li-ion Battery Data," Mendeley, Jun. 2018. doi: 10.17632/WYKHT8Y7TG.1.

[190] J. Yosinski, J. Clune, Y. Bengio, and H. Lipson, "5347-How-Transferable-Are-Features-in-Deep-Neural-Networks," pp. 1–9

[191] O. Christopher, "Understanding LSTM networks," Github, 2015. .

[192] S. J. Pan and Q. Yang, "{A} {S}urvey on {T}ransfer {L}earning," {IEEE} {T}ransactions on {K}nowledge and {D}ata {E}ngineering (TKDE), vol. 22, no. 10, pp. 1345–1359, 2010.

[193] J. Rifkin, The Zero Marginal Cost Society: The Internet of Things, the Collaborative Commons, and the Eclipse of Capitalism. Macmillan, 2014.

[194] I. J. Goodfellow, O. Vinyals, and A. M. Saxe, "Qualitatively characterizing neural network optimization problems," 3rd Int. Conf. Learn. Represent. ICLR 2015 - Conf. Track Proc., 2015.

[195]   D. Erhan, P. A. Manzagol, Y. Bengio, S. Bengio, and P. Vincent, "The difficulty of training deep architectures and the effect of unsupervised pre-training," J. Mach. Learn. Res., vol. 5, pp. 153–160, 2009.

[196] X. Glorot and Y. Bengio, "Understanding the difficulty of training deep feedforward neural networks," J. Mach. Learn. Res., vol. 9, pp. 249–